Development of Volatile Inorganic Compounds and Their Application for Chemical Vapour Deposition of Metal and Metal Oxide Thin Films

by

Agnieszka Kurek

A thesis submitted to the Faculty of Graduate Studies and Postdoctoral Affairs in partial fulfillment of the requirements for the degree of

Doctor of Philosophy

in

Ph.D. Chemistry

Carleton University

Ottawa, Ontario

Abstract

Chemical vapour deposition is a necessary and important technology for the manufacture of nano-thin metal films. The reactivity and thermal stability of the metal complexes used in this process are key to the deposition process. Through logical design, guanidinate ligands have evolved into iminopyrrolidinates to prevent decomposition pathways. These ligands were first tested on aluminum metal centres. Iminopyrrolidinates have been further stabilized with additional methyl moieties and have led to promising new copper precursors. Copper metal is desirable for interconnecting material in electronics due to its high conductivity. The reactivity of 1,3-diisopropyl-imidazolin-2-ylidene copper hexamethyl disilazide has been explored and yielded three new copper metal compounds. Sputtered thin films of gold have been used in metal assisted chemical etching to produce high aspect ratio structures on the surface of silicon substrates.

Preface

Here are the full bibliographical details for all reproduced publications included in this thesis. The supervisor, Seán T. Barry, and the student, Agnieszka Kurek, confirm that the student was fully involved in setting up and conducting the research, obtaining data and analyzing results, as well as preparing and writing the material presented in the co-authored articles integrated in this thesis. Additionally, the supervisor confirms the information provided by the student in this preface.

To cite material from this thesis, please cite both this thesis and the relevant article from the chapter, if the chapter is based on a published work.

Kurek, A.; Gordon, P.G.; Karle, S.; Devi, A.; Barry, S.T. Recent Advances Using Guanidinate Ligands for Chemical Vapour Deposition (CVD) and Atomic Layer Deposition (ALD) Applications, Aust. J. Chem. 2014, 67, 989-996. DOI: 10.1071/CH14172

This article was reproduced partially in sections 1.4 – 1.6 and Chapter 2. Minor edits were made to enhance clarity. Reprinted with permission from CSIRO and CSIRO PUBLISHING. http://www.publish.csiro.au/nid/51/paper/CH14172.htm

Wasslen, Y.A.; Kurek, A.; Johnson, P.A.; Pigeon, T.C.; Monillas, W.H.; Yap, G.P.A.; Barry, S.T. Heteroleptic Iminopyrrolidinates of Aluminium, Dalton Trans., 2010, 39, 9046. DOI: 10.1039/C0DT00267D

This article is reproduced wholly in Chapter 3 and edited for clarity of presentation. The word "tautomersed" was replaced with "resonance structure." Reproduced by permission of The Royal Society of Chemistry. http://pubs.rsc.org/en/Content/ArticleLanding/2010/DT/c0dt00267d#!divAbstract

Gordon, P.G.; Kurek, A.; Barry, S.T. Trends in Copper Precursor Development for CVD and ALD Applications, J. Sol. State Sci. Technol., 2015, 4 (1) N3188-N3197. DOI: 10.1149/2.0261501jss

This article is reproduced wholly in Chapter 4 and edited for clarity of presentation. Reprinted with permission under the Creative Commons License. http://creativecommons.org/licenses/by/4.0/legalcode

Coyle, J.P.; Kurek, A.; Pallister, P.J.; Sirianni, E.R.; Yap, G.P.A.; Barry, S. T. Preventing Thermolysis: Precursor Design for Volatile Copper Compounds, Chem. Commun. 2012, 48, 10440. DOI: 10.1039/C2CC35415B

This article is reproduced wholly in Chapter 6 and edited for clarity of presentation. Reproduced by permission of The Royal Society of Chemistry. http://pubs.rsc.org/en/content/articlelanding/2012/cc/c2cc35415b#!divAbstract

Coyle, J.P.; Pallister, P.J.; Kurek, A.; Sirianni, E.R.; Yap, G.P.A.; Barry, S.T. Copper Iminopyrrolidinates: A Study of Thermal and Surface Chemistry, Inorg. Chem. 2013, 52, 910. DOI: 10.1021/ic3021035

This article is reproduced wholly in Chapter 7 and edited for clarity of presentation. Reprinted with permission from {Coyle, J.P.; Pallister, P.J.; ***Kurek, A.****; Sirianni, E.R.; Yap, G.P.A.; Barry, S.T. Copper Iminopyrrolidinates: A Study of Thermal and Surface Chemistry, Inorg. Chem.* ***2013****, 52, 910} Copyright {2013} American Chemical Society.*

Kurek, A.; Barry, S.T. Metal-Assisted Chemical Etching Using Sputtered Gold: A Simple Route to Black Silicon, Sci. Technol. Adv. Mater., 2011, 045001. DOI: 10.1088/1468-6996/12/4/045001

This article is reproduced wholly in Chapter 8 and edited for clarity of presentation. Reprinted with permission under the Creative Commons License. http://creativecommons.org/licenses/by-nc-sa/3.0/legalcode

Acknowledgements

This thesis is dedicated to my dad, Ryszard Kurek, who unfortunately did not make it to witness my academic achievements but gave me all the advantages he could throughout my childhood and always let me know how proud he was of me.

There are many people to thank for their unwavering support throughout my graduate studies. First and foremost – Prof. Seán T. Barry. His knowledge, passion and drive have motivated me to become my best. I have gained confidence, carefullness and experience that I would not have found elsewhere. I am forever grateful for his investment in my education. The past and present members of the Barry Lab are also to thank for their help and support over the years. Especially, Yamile Gaudette, Julie Pallister, Peter Gordon, Jason Coyle, and Peter Pallister for their patience and teaching in the lab.

My mom, Margaret and her partner Jurek have always been supportive of me. My loving fiancée Darren Park has been my rock these past few years. I hope this body of work inspires my daughter, Karolina, to achieve something great in her life.

Table of Contents

Abstract 2

Preface 3

Acknowledgements 5

List of Tables 9

List of Figures 11

Chapter 1 – General Introduction 14

1.1 Thermogravimetric Analysis 16
1.2 Chemical Vapour Deposition (CVD) 18
1.3 Atomic Layer Deposition (ALD) 21
1.4 Ligand and Metal Compound Design 24
1.5 Metal-Assisted Chemical Etching (MACE) 27

Chapter 2 – Recent Advances Using Guanidinate Ligands for CVD and ALD Applications 29

2.1 Abstract 30
2.2 Introduction 31
2.3 Results and Discussion 32
Metal Guanidinate Complex Synthesis and Mechanism 32
Contribution of Guanidinates to Precursor Development 35
Copper Metal Deposition by CVD 37
Versatility of Metal Guanidinate Precursors 39
Future Directions and Perspective 43
2.4 Conclusions 47

Chapter 3 – Heteroleptic Iminiopyrrolidinates of Aluminium 48

3.1 Abstract 48
3.2 Introduction 50
3.3 Results and Discussion 53
3.4 Experimental 69
3.5 Conclusions 80

Chapter 4 – Trends in Copper Precursor Development for CVD and ALD Applications 81

4.1 Abstract 82
4.2 Introduction 84
Chemical Vapor Deposition (CVD) vs. Atomic Layer Deposition (ALD) 84
Copper Reduction 87
4.3 Results and Discussion 91
Diethyl Zinc 91
Iodine Catalyzed Copper Deposition 94
Solution Testing of Second Precursors 94
Comparison of CVD and ALD of Copper 97
Copper Chloride 99
Aminoalkoxides 102
Amidinates 108
Betadiketonates and Betaketoiminates 112
4.4 Conclusions 117

Chapter 5 – Novel Copper Compounds: Characterization and Thermolysis 119

5.1 Abstract 119
5.2 Introduction 120
5.3 Results and Discussion 121
Thermogravimetric Analysis of Ligands 121
Synthetic Procedure 123
Single Crystal X-ray Diffraction 126
Thermogravimetric Analysis of Copper Compounds 131
5.4 Experimental 133
5.5 Conclusions 136

Chapter 6 – Preventing Thermolysis: Precursor Design for Volatile Copper Compounds 137

6.1 Abstract 138
6.2 Introduction 138
6.3 Results and Discussion 140
6.4 Conclusions 146

Chapter 7 – Copper Iminopyrrolidinates: A Study of Thermal and Surface Chemistry 147

7.1 Abstract 148
7.2 Introduction 148
7.3 Results and Discussion 153
7.4 Experimental 175
7.5 Conclusions 180

Chapter 8 – Metal Assisted Chemical Etching Using Sputtered Gold: A Simple Route to Black Silicon 182

8.1 Abstract 183
8.2 Introduction 183
8.3 Results and Discussion 185
8.4 Experimental 194
8.5 Conclusions 195

Chapter 9 – Conclusions 196

References 202

List of Tables

2.3.1: *Summary of Chemical Vapour Deposition (CVD) with Guanidinate Precursors* **37**

2.3.2: *Summary of Atomic Layer Deposition (ALD) with Guanidinate Precursors* **40**

2.3.3: *Thermolysis Studies of New Guanidinate CVD and ALD Precursors* **44**

3.3.1: *Yields and Melting Points of Iminopyrrolidine Ligands* **54**

3.3.2: *Yields and Melting Points of Aluminum Dimethyl Iminopyrrolidinate Complexes* **57**

3.3.3: *Metrical Data for ipipAlMe$_2$ (7)* **59**

3.3.4: *Metrical Data for tbipAlMe$_2$ (12)* **59**

3.3.5: *Yields and Melting Points of Aluminum Diethyl Iminopyrrolidinate Complexes* **61**

3.3.6: *Metrical Data for sbipAlEt$_2$ (14)* **62**

3.3.7: *X-ray Data for 7, 12, and 14* **63**

3.3.8: *Rate Constant and Half-life for the First-order Decomposition of Compounds 7 – 12 at 78 °C* **66**

4.2.1: *Summary of Copper Metal Deposition Processes by Chemical Vapor Deposition or Atomic Layer Deposition* **90**

5.3.1: *Metrical Data for 1* **127**

5.3.2: *Metrical Data for 3* **128**

5.3.3: *X-ray Data for 1, and 3* **129**

6.3.1: *Selected Bond Lengths and Angles for 1* **144**

7.3.1: *Selected Bond Lengths and Angles for 1 and 2* **158**

7.3.2: *Kinetic Data for the Thermal Decomposition of 1 – 4 at 165°C. The "Correlation Coefficient" Refers to the Linear Fit in Figure 8.3.5* **167**

7.3.3: *Elemental Analysis of Samples a – c. Data for Sample a was Below the Limit of Detection* **174**

9.0.1: *Summary of Ligand Improvements to [Cu(iPr-guan)]$_2$* **202**

9.0.2: *Summary of Ligand Improvements to (NHC)Cu(HMDS)* **203**

List of Figures

1.1.1: *Thermogravimetric analysis curve of a volatile compound.* **17**

1.1.2: *Thermogravimetric analysis curve of a compound undergoing thermolysis.* **18**

1.2.1: *Illustration of typical coverage for sputter deposition, CVD and ALD on a substrate with a deep surface feature.* **20**

1.3.1: *Schematic representation of one ALD cycle of Al_2O_3 growth using trimethylaluminum (TMA) and water. Steps 1 – 4 are repeated to achieve desired film thickness.* **23**

1.5.1: *The general mechanism of metal-assisted chemical etching.* **27**

***2.3.1**: Reaction scheme of 1) rapid tris(guanidinato)Al(III) complex formation by CDI insertion, followed by 2) slow ligand exchange to form bis- and mono-substituted Al (III) species.* **34**

2.3.2: *Resonance structures of a general guanidinate ligand.* **35**

2.3.3: *DFT-calculated fragmentation pattern of Cu(I) guanidinate compound.* **39**

2.3.4: *Selection of proposed fragmentation pattern of $Gd(DPDMG)_3$, under MS conditions (EI-MS, 70 eV) highlighting imido species products.* **42**

2.3.5: *a) Substituted mono(guanidinato) Ge compound; b) bis(guanidinato) Ge monomer where R= Me or Et.* **45**

3.2.1: *Deinsertion of carbodiimide (CDI) at elevated temperatures.* **52**

3.2.2: *The similarity in chelating geometry of an amidinate and an iminopyrrolidinate.* **52**

3.3.1: *Synthetic procedure for iminopyrrolidine ligands.* **53**

3.3.2: *Thermogravimetric anaylsis of iminopyrrolidine ligands 1 – 6.* **56**

3.3.3: *Synthesis of $AlMe_2$iminopyrrolidinate complexes.* **57**

3.3.4: *Molecular structures of 7 and 12, respectively. Thermal ellipsoids are drawn at 50% probability, and the H atoms have been omitted for clarity.* **58**

3.3.5: *Molecular structure of 14. Thermal ellipsoids are drawn at 50% probability, and the H atoms have been omitted for clarity.* **62**

3.3.6: *Thermogravimetric analysis of heteroleptic aluminum complexes 7 – 12.* **65**

3.3.7: *First order decomposition of compounds 7 – 12 at 78°C.* **67**

3.3.8: *Isomerization followed by dimerisation of the ligand.* **68**

4.2.1: *CVD (a) is a continual deposition where all reactants are introduced simultaneously, and reaction ideally occurs at the surface by chemisorbed species. ALD (b) occurs in several steps, ideally by 1) chemisorption of the precursor, 2) purge of the byproducts, 3) reaction with a second precursor or "secondary reactant gas," and 4) another purge of byproducts.* **87**

4.3.1: *The reduction of copper "dmap" by dielthyl zinc through ligand exchange and subsequent reductive elimination.* **93**

4.3.2: *Diethylzinc likely undergoes ligand exchange with copper surface species in a two-step reaction, generating an intermediate mixed ligand zinc compound before fully eliminating* $ZnCl_2$. **94**

4.3.3: *Chemical structures for the variety of copper precursors discussed in this review.* **97**

4.3.4: *Insertion of dihydrogen gas into the existing copper-chloride bond of a copper chloride surface species, with subsequent elimination of hydrogen chloride gas.* **101**

4.3.5: *Reaction of chemisorbed copper dimethylaminoethoxide undergoing (a) beta-hydrogen elimination and subsequently (b) reductive elimination to produce copper metal from copper(II) dimethylaminoethoxide.* **105**

4.3.6: *Exchange of a surface bound "dmap" ligand with formic acid to form a surface formate.* **107**

4.3.7: *The surface reaction of hydrazine and subsequent reaction to produce copper metal from surface bound copper formate.* **108**

4.3.8: *Dimethylaminoborane forming dihydrogen in the gas phase, and the subsequent reaction of dihydrogen to reduce surface-bound copper "dmap" to metallic copper.* **109**

4.3.9: *Thermal fragmentation of copper(I) amidinate at a nickel surface with increasing temperatures.* **111**

4.3.10: *Thermal fragmentation of copper(I) guanidinate at a nickel surface with increasing temperatures.* **112**

4.3.11: *The decomposition of copper(I) "dtip" at elevated temperature.* **113**

4.3.12: *Stabilization of copper by pyridine, and activation of the copper-oxygen bond through interaction with the hexafluoroacetylacetonate ligand.* **118**

5.2.1: *Structure of 1,3-diisopropyl-imidazolin-2-ylidene copper hexamethyl disilazide.* **121**

5.3.1*: Thermogravimetric analysis curves of protonated ligands: N-acetylbenzamide and diacetamide.* **123**

5.3.2: *Synthetic scheme of **1** (top), and **2** (bottom).* **124**

5.3.3: *Synthetic scheme of **3**.* **125**

5.3.4: *Molecular structure of **1**. Thermal ellipsoids are drawn at 50 % probability, and the H atoms have been omitted for clarity.* **127**

5.3.5: *Molecular structure of **3**. Thermal ellipsoids are drawn at 50 % probability, and the H atoms have been omitted for clarity.* **128**

5.3.6: *Crystal structure unit cell for **1**.* **131**

5.3.7: *Thermogravimetric analysis curves of **1**, **2** and **3**.* **133**

6.2.1: *Thermal decomposition pathways for copper(I) amidinates, where R can be an alkyl or an amine.* **140**

6.3.1: *The synthetic procedure for producing the tert-butyl-imino-2,2-dimethylpyrrolidine ligand.* **141**

6.3.2: *The structure of **1,** with hydrogens removed for clarity, and the thermal ellipsoids shown at 30 %.* **143**

6.3.3: *Thermal stress test of compounds a) 1 and b) 2, showing effect on residual mass as starting mass was increased.* **145**

6.3.4: *Reactivity of **1** with silica: a) shows the SS-^{13}C NMR of silica after deposition of **1** at 275°C (top trace) compared to the HR-^{13}C NMR of **1** in deuterated benzene (bottom trace). b) shows the HR-^{1}H NMR of the surface species etched from the silica with D_2O (in D_2O; top trace) compared to the HR-^{1}H NMR of **1** in $CDCl_3$ (bottom trace). c) shows the proposed nucleation and chemisorption of **1** at a silanol group on a silica surface.* **147**

7.2.1: *Two thermal decomposition pathways for a Cu(I) guanidinate species.* **152**

7.2.2: *A series of amidinate-type ligands with differing numbers of ß-hydrogens, shown as their corresponding copper(I) compounds*. **154**

7.3.1: *The structure of a) 1 and b) 2, shown with the hydrogens removed for clarity. The thermal ellipsoids are at 30%.* **155**

7.3.2: *Thermal stress test of compounds 3 showing no change in residual mass with increasing sample mass (left), and 1 showing increasing residual mass with increasing initial sample mass (right).* **161**

7.3.3: *Thermal stress test trends for compounds 1 – 4.* **162**

7.3.4: *Evaporation kinetics of 1 – 4 by TG analysis.* **164**

7.3.5: *Thermal decomposition of 1 – 4 at 165°C over 21 days.* **167**

7.3.6: *Solid-state ^{29}Si {^{1}H} CP/MAS NMR of samples a - c.* **171**

7.3.7: *Solid-State ^{13}C {^{1}H} CP/MAS NMR of high surface area silica samples a – c.* **172**

7.3.8: *High-res ^{1}H NMR of D_2O after it was washed over samples b and c.* **174**

7.3.9: *Possible thermolysis of the surface species formed by **3** on high-surface area silica.* **176**

8.3.1: *SEM images demonstrating a 6 min etch of silicon by peroxide/HF with an 8 nm sputtered gold film. Panels a) and c) show different magnifications of a sample etched without ultrasonication. Panels b) and d) show the effect of ultrasonication. Both samples are shown with gold remnants on the surface.* **189**

8.3.2: *The aspect ratio of surface features as a function of etch time. Panels a) – d) show a 45°-inclined view and panels e) – h) show a cross-sectional view.* **191**

8.3.3: *The aspect ratio of surface features as a function of etch time. The etch rate fits a logarithmic trend (shown as a dashed line) with a coefficient of determination (R^2) of 0.9909.* **192**

8.3.4: *The radiance factor over the visible spectrum of the samples etched for 0 – 24 min with sonication.* **192**

8.3.5: *SEM images showing the top layer that is formed and liberated from the substrate during a peroxide/HF etch for various etch times. Panels a), c) and e) show plane view and panels b), d) and f) show a side view. Panels a) and b) show a typical top layer after 12 min etching. Panels c) and d) show an isolated "plateau" feature after 18 min etching. Panels e) and f) show the pores etched through the top layer "plateau" features and into the underlying layer after 24 min etching. All samples are shown with gold remnants present on the surface.* **195**

8.3.6: *SEM images of the same pore on two complementary edges of a cleaved substrate. The sample shown was etched for 24 min and gold catalyst has been removed by aqua regia.* **196**

Chapter 1 – General Introduction

Copper metal films are important components in microelectronics as interconnect material. The challenge facing the industry is the demand for

increasingly smaller devices. Copper metal is commonly deposited electrochemically however; this method cannot deposit the required nanoscale thin films. Vapour deposition of thin films is an effective alternative method, but due to surface chemistry or other factors, a smooth, continuous film is often not produced. Rather, it deposits as small pebble-like islands that introduce undesirable grain boundaries. Different vapour deposition precursors produce different film qualities and there is no ideal copper metal precursor yet. Chapter 4 describes the chemistries of copper film deposition. For this reason, this work set out to synthesize new metal compounds, suitable for the vapour phase deposition of copper and potentially other metal thin films. Ligands were improved and tested on aluminum and copper metal centres for volatility and precursor suitability. To demonstrate an application of thin films, sputtered gold was used in a metal-assisted chemical etch application to produce black silicon. The following chapter describes some key concepts and themes that reoccur throughout the thesis.

Aluminum oxide coatings are used as electrical insulators in microelectronic circuits and are grown by atomic layer deposition, using the following chemistry. The oxygen source can either be water or ozone and trimethylaluminum (TMA) is the aluminum metal source.

$$2\ Al(CH_3)_{3\ (g)} + 3\ H_2O_{\ (g)} \rightarrow Al_2O_{3\ (s)} + 6\ CH_{4\ (g)}$$

$$2\ Al(CH_3)_{3\ (g)} + O_{3\ (g)} \rightarrow Al_2O_{3\ (s)} + 3\ C_2H_{6\ (g)}$$

TMA is most commonly used in industry but is pyrophoric and requires special handling and storage. Therefore, there is motivation for developing aluminum-containing precursors as desirable alternatives to TMA.

1.1 Thermogravimetric Analysis

Thermogravimetric analysis is a bench-top analytical technique that assesses the volatility of a compound. A < 50mg sample is loaded onto a tared platinum pan and suspended on a balance. A tube furnace encloses the pan and inert, N_2 gas, is flowed through the tube. As the temperature of the furnace increases at a pre-programmed rate, typically 10ºC/min, the mass of the pan is recorded. Depending on the compound, the final temperature is programmed to about 500ºC or less. Experiment time and temperatures are also recorded.

The curve of percentage weight loss against temperature provides a lot of information about the thermal behaviour of the compound in question. The temperature at which 5% mass loss occurred is herein referred to as the “onset of volatilization.” This arbitrary temperature point is where one can safely say that there will be detectable vapour phase molecules. After this point, the curve of a volatile compound takes a rapid descent until it reaches 0% mass remaining. Figure 1.1.1 depicts a typical curve for a volatile compound.

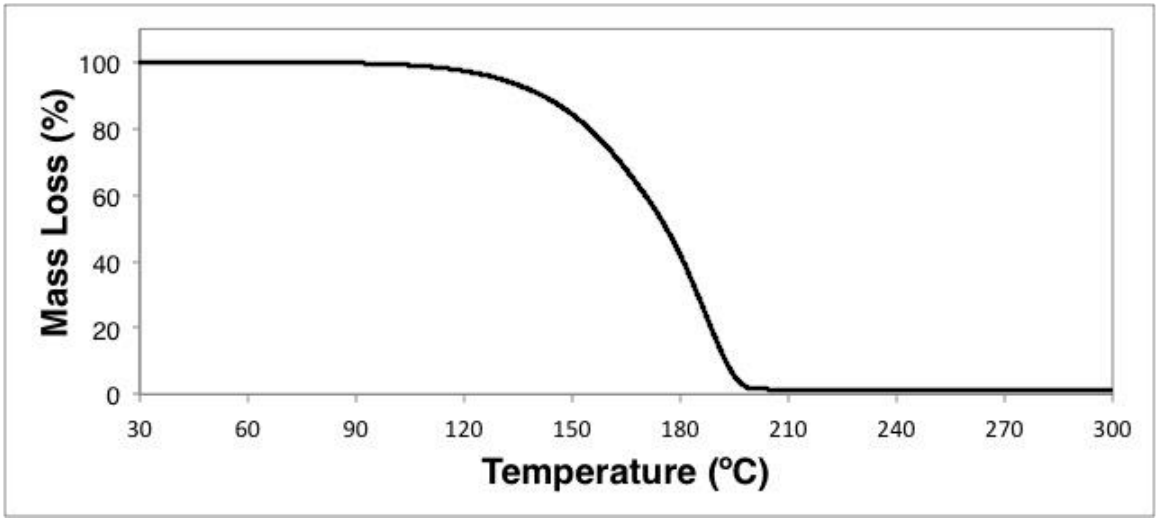

Figure 1.1.1: Thermogravimetric analysis curve of a volatile compound.

If the curve levels off at a percentage other than 0%, i.e. some mass remains in the pan, this indicates that the compound underwent some thermal decomposition after, or during the volatilization event. Alternatively, the compound may have contained a non-volatile impurity. However, samples are typically screened for quality before being subjected to this analysis. If the mass remaining is less than the atomic percentage of metal in the compound, it may be useful as a CVD precursor (see section 1.2) but further testing would be required. If the curve contains several features and/or has high residual mass in the pan, it is eliminated as a potential precursor. Figure 1.1.2 depicts a TGA curve of a compound that decomposes in several steps and has a non-zero residual mass. A compound with this thermolysis pattern would not be considered a volatile precursor candidate.

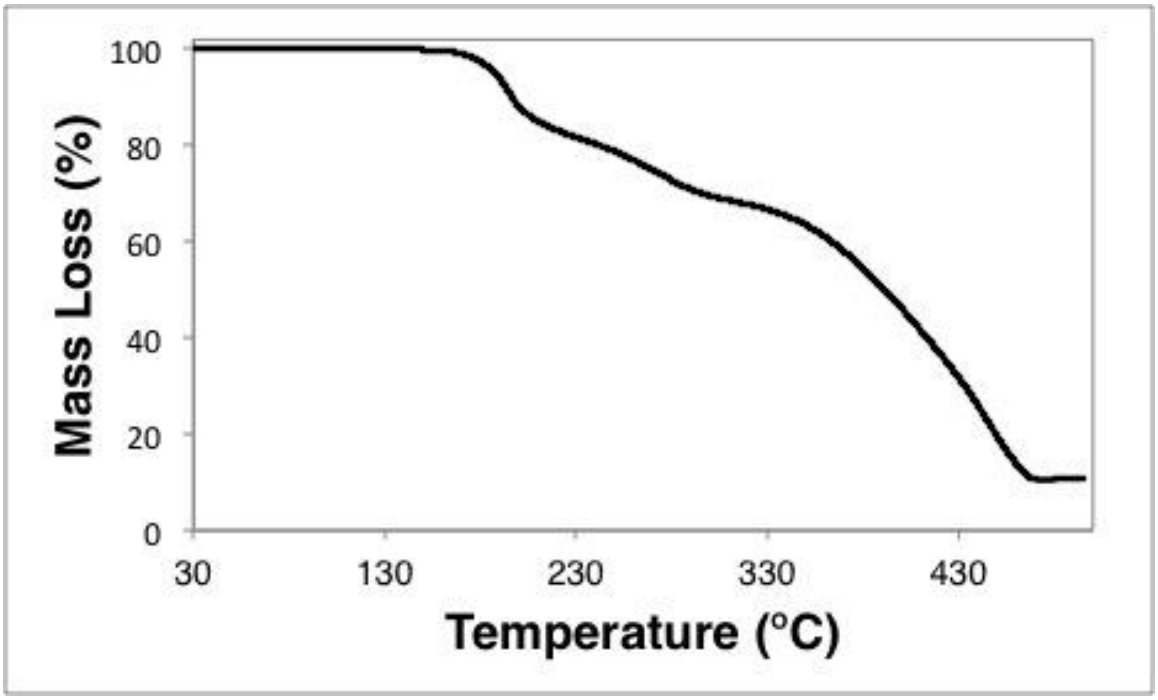

Figure 1.1.2: Thermogravimetric analysis curve of a compound undergoing thermolysis.

One can also maintain the sample at a constant temperature for a period of time before quickly ramping to another and repeating this process until the end of the experiment. The slope of the line segments provides the evaporation rate at a given temperature in mg/min. This information is useful in ALD processes (see section 1.2 and 1.3) because one can estimate the amount of compound needed for the deposition of a certain thickness of film and the temperature at which to maintain the precursor source.

Since the compounds discussed in this thesis are air and moisture sensitive, the thermogravimetric analyzer is located inside a drybox under an inert atmosphere of nitrogen gas.

1.2 Chemical Vapour Deposition (CVD)

Chemical vapour deposition employs volatile compounds, which are typically heated and continuously entrained into a deposition chamber. These precursors chemically react on a heated substrate and build up a film of a target material while unwanted volatile components are removed by reduced pressure or an inert gas purge or a combination thereof. Single source precursors (SSPs) incorporate multiple components to the growing film from a single precursor molecule. However, this may introduce a variety of impurities from organic ligand combustion products. Another way to promote the desired chemistry of the film is to employ co-reagents, i.e. separate reactive gases, which are simultaneously introduced into the reaction chamber. Oxygen, water or ozone are commonly used for oxides, and ammonia for nitrides. CVD rapidly covers the substrate in a thin film of the target material, tunable to nanometers in thickness. This bottom-up nanoscale approach is applied in the microelectronics industry for fabrication of interconnects and semiconductor materials.

One disadvantage of CVD is encountered when the complexity of the substrate is increased. High aspect ratio features can be overgrown as deposition proceeds because the precursors are typically thermally unstable and are more likely to react immediately, closer to the top of the feature (Figure 1.2.1). The bottom of a feature is thus commonly under-coated by the desired material due to this bottlenecking effect. CVD is therefore not an ideal choice for applications such as photovoltaics, memory storage or hydrophobic materials where continuous, conformal coatings are needed over complicated morphologies. Despite this drawback, CVD can be used for many applications

that require simpler substrates. In fact, it is often preferred over line-of-sight techniques such as sputtering which tend not to cover the sides of nanostructures and build up a concentration gradient on the plane normal to the source (Figure 1.2.1).

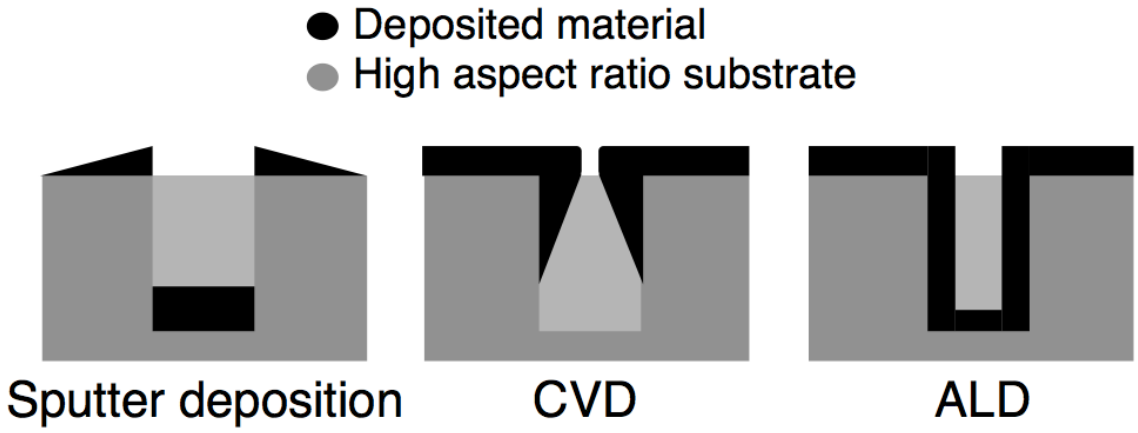

Figure 1.2.1: Illustration of typical coverage for sputter deposition, CVD and ALD on a substrate with a deep surface feature.

This leads to non-conformal, non-uniform coverage. CVD boasts much better control over roughness and conformality of thin films compared to sputtering. Both benefits are extremely important on the nanoscale and vital for good quality films.

1.3 Atomic Layer Deposition (ALD)

ALD is similar to CVD but is particularly useful in coating more complex surfaces. The notable distinction between ALD and CVD is that the volatile precursors in ALD are designed to deliver film components by self-limiting reactions at the surface. ALD precursor molecules are designed to only react at nucleation sites on the surface of the substrate while remaining unreactive towards other molecules in the gas phase and towards other surface species. In the ideal case, this method leaves a single, molecule-thick monolayer over the entire substrate that contains an element of the target film in the deposition process. Depending on the specific process, exposure of the substrate to the precursor can range from fractions of a second to several seconds. Typically, a vacuum purge is then used to evacuate volatile byproducts and excess, unreacted precursor from the reactor chamber. A second precursor is subsequently introduced to add the second component of the target film or reduce the chemisorbed species to leave behind the target film. This second exposure is followed by another evacuation step, again removing byproducts and unreacted precursor. This four-part process constitutes one “ALD cycle” (Figure 1.3.1). Once the film growth per cycle has been determined for a process, controlling the number of ALD cycles can reproducibly grow a desired thickness

of material. Relative to CVD, ALD is a slower but more careful process that offers the advantage of conformal coverage even on very high surface area or aspect ratio substrates due to its self-limiting nature (Figure 1.3.1). The deposition of the film is governed by step-wise reactions. In this particular example, trimethylaluminum (TMA) reacts with the silicon surface at available hydroxyl sites. When all of the sites are occupied, TMA will not react with itself, thus suspending film growth. The unreacted TMA and by-products are removed from the reactor by vacuum purges and the second precursor, in this case, water, is introduced and reacts with the surface chemisorbed TMA to knit together one "monolayer" of desired film. The cycle is repeated until desired thickness is achieved. The "self-limited nature" of this process refers to the fact that the *surface chemistry* of the precursors governs film growth rather than *quantity* of gaseous precursor, as in a typical CVD process. I.e. The concentration of TMA in the presence of a substrate is irrelevant once all surface sites have been saturated with chemisorbed species.

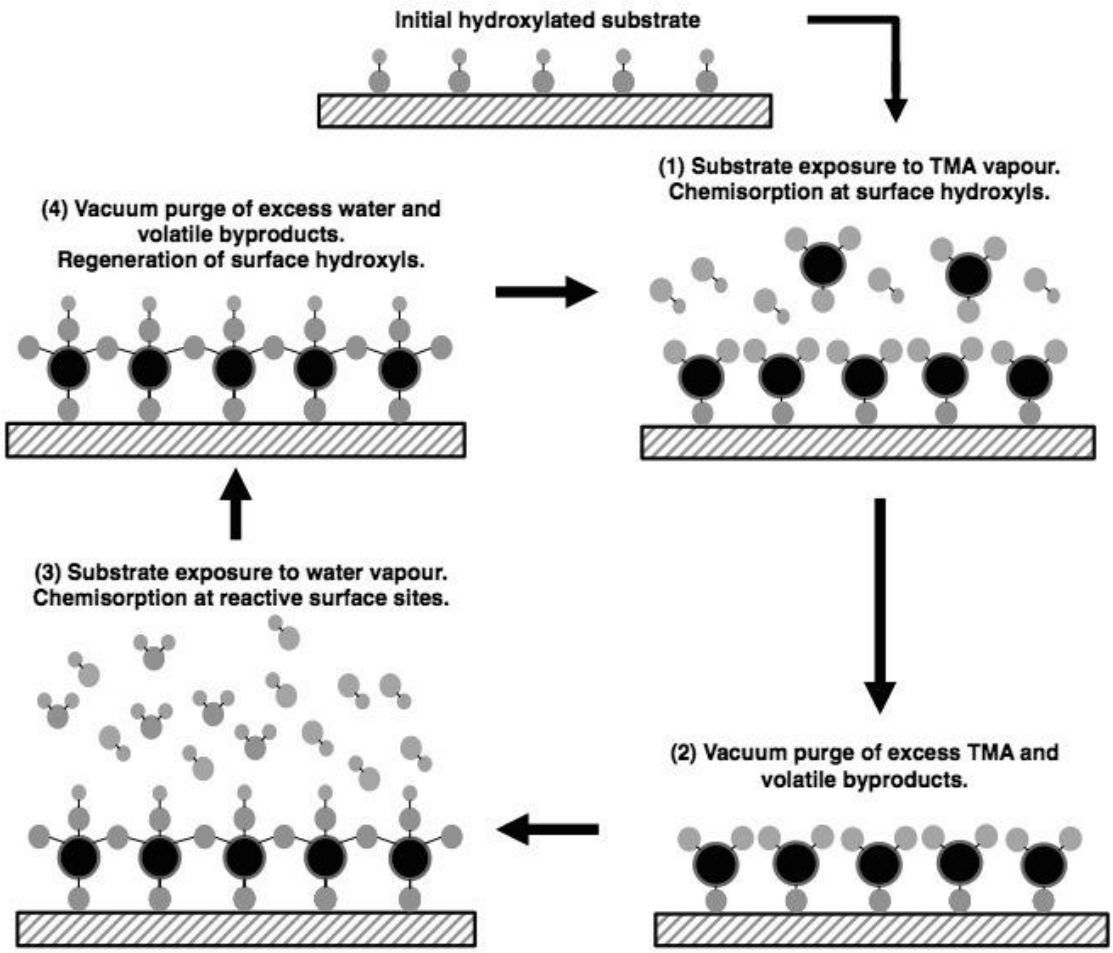

Figure 1.3.1: Schematic representation of one ALD cycle of Al_2O_3 growth using trimethylaluminum (TMA) and water. Steps 1 – 4 are repeated to achieve desired film thickness.

1.4 Ligand and Metal Compound Design

There are several key criteria that must be balanced in order to design an excellent precursor. Volatility is of utmost importance. Overall low molecular weight, branching, cleavage points (e.g. alkoxy groups), and asymmetry of the ligands can help produce a highly volatile compound. Ideal precursors exhibit high vapour pressure at low temperatures. Liquid precursors provide constant vapour pressure as the compound is depleted; therefore low melting points are advantageous. Unwanted thermal decomposition from over-heating can lead to film impurities that compromise function. In many cases, the precursor is heated inside a holding canister or "bubbler" and transported through a network of heated vacuum lines and valves before reaching the substrate. Therefore it must be thermally robust enough to withstand this journey without condensing or decomposing along the route or inside the bubbler. Warm, inert carrier gases such as Ar or N_2 can help minimize this effect. The compound must be reactive enough to chemisorb quickly to a target surface, but avoid polymerization, self-propagated decomposition or other reactivity in the gas phase. Coordinative saturation and heteroleptic structures are often used in metal-containing precursors to promote such chemical stability and selective reactivity, respectively. For ALD, the surface chemistry must be designed to ensure regeneration of reactive surface sites across the substrate after every purge step (Figure 1.3.1). During either CVD or ALD, the ligand system should cleave cleanly from the metal and be volatile enough to be removed without leaving behind unwanted impurities.

Ligand design is not always as straightforward as changing an R group as in the iminopyrrolidine work presented in Chapter 3. For example, to prevent β-hydrogen abstraction, two methyl groups were added to the pyrrole ring; which effectively removed hydrogens that were two bonds away from the copper metal. However, the synthesis needed to be reinvented for two reasons: 1) the yield for tert-butyl iminopyrrolidine could not be optimized using the procedure presented in section 3.4; 2) the pyrrole had to be synthesized first. It took modification of a new literature method to succeed with the optimization of the dimethyl tertbutyl iminopyrrolidine ligand as described in Chapter 6.

Thorough understanding and improvement of a given ligand such as this would not have been possible without an accumulation of thermolysis studies in conjunction with thermogravimetric analysis. Sealed Nuclear Magnetic Resonance (NMR) tube boil-ups, as discussed Chapters 3, 6 and 7 are simple in concept but can be used to identify structural weaknesses in compounds, such as carbodiimide (CDI) deinsertion in guanidinates. Adding CDI reagent to the NMR tube and checking whether the integration value for that peak increased in the ^{1}H NMR spectrum can easily verify whether CDI is truly a thermolysis by product. Time-of-flight mass spectroscopy studies can also be of value to determine the gas-phase fragments that may form during thermolysis. Computer simulations with Density Functional Theory (DFT) calculations can be used to determine the thermodynamically favoured decomposition products and help elucidate a decomposition mechanism. In a custom-built reactor, if a precursor is exposed over a high-surface area silica a monolayer may form. Solid-state NMR

can then be used to determine surface species, as demonstrated in Chapter 6 and 7. Careful ligand design is vital and governs volatility, reactivity and purity of the resulting material.

1.5 Metal-Assisted Chemical Etching (MACE)

The chemistry of Metal-Assisted Chemical Etching (MACE) has recently been exploited for the fabrication of black silicon – high aspect ratio topography on the surface of silicon. This highly textured substrate appears velvet-like black to the naked eye. The nanostructured pillars that the surface is comprised of capture light in a unique way and reflect very little of the incident beam. This property has led to the development of more efficient solar cell devices.

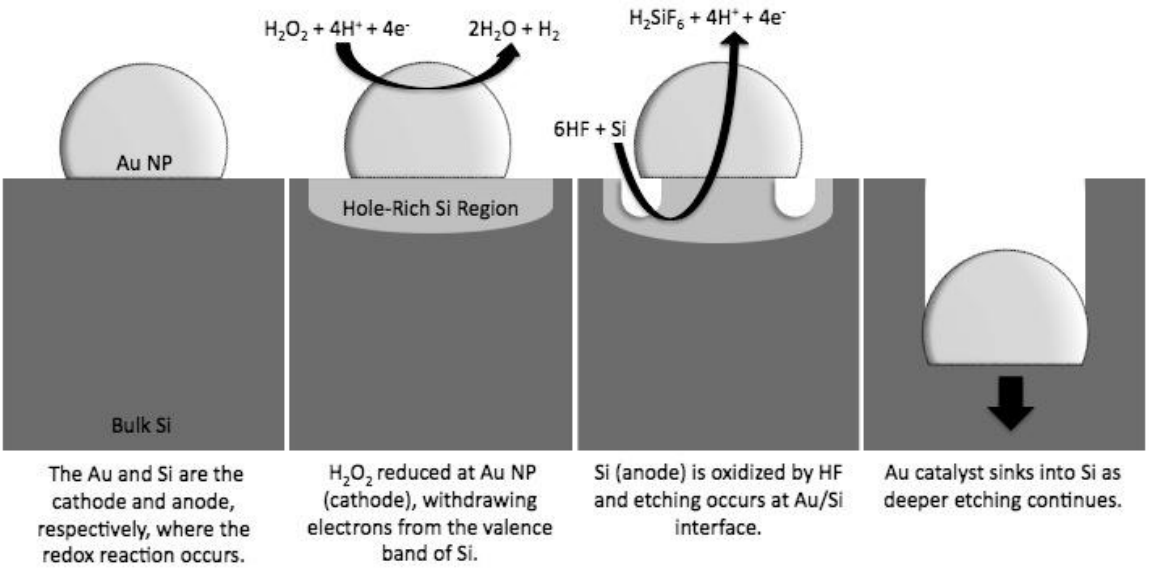

Figure 1.5.1: The general mechanism of metal-assisted chemical etching.

The silicon etching mechanism is described in Figure 1.5.1. Metal nanoparticles (in this case, gold) are first deposited on the silicon substrate. This can be done by many means, including sputtering and CVD. Noble metals work best as they will not react and be removed from the surface in the acidic etching environment. The redox chemistry depicted above occurs. The metal nanoparticle catalyzes the reduction of hydrogen peroxide to water at the surface

by channeling electrons from the silicon surface it is in contact with. This depletes electrons from the underlying silicon and makes it vulnerable to dissolution by hydrogen fluoride. The silicon is oxidized and is physically removed from the surface. The metal catalyst sinks into the cavity and the etching process continues until the substrate is removed from the etching solution and rinsed with distilled water to halt the reaction. This process is rapid and dependent on time, concentration, quantity of catalyst, temperature, and agitation among other factors. This process is explored in detail in Chapter 9.

Chapter 2 discusses the usefulness of guanidine ligands in chemical vapour deposition (CVD) and atomic layer deposition (ALD). Iminopyrrolidine ligands evolved from guanidines and Chapter 3 presents a family of iminopyrrolidinate aluminum precursors and studies of their thermolyses. Chapter 4 reviews copper metal CVD and ALD and serves as an introduction to Chapters 4, 5 and 6. Several novel copper compounds were characterized and their thermal properties were investigated here. Lastly, Chapter 7 highlights an application of thin films – metal assisted chemical etching (MACE) of silicon to afford a highly nanostructured surface.

Chapter 2 – Recent Advances Using Guanidinate Ligands for CVD and ALD Applications

Reprinted with permission from CSIRO and CSIRO PUBLISHING.
http://www.publish.csiro.au/nid/51/paper/CH14172.htm

Please see preface, page 3, for more details and full article citation. Author contributions listed below are paraphrased from signed Letters of Permission to reprint this material.

Agnieszka Kurek is first author of this review paper. Her contributions to this published work included literature research, writing, editing and figure composition.

Peter Gordon contributed some writing and research.

Sarah Karl wrote about examples from the Devi group's work of homoleptic Dy and Gd tris(guanidinates) and tris(amidinates) and their application in MOCVD and ALD processes.

Anjana Devi contributed data and discussion on Dy and Gd tris(guanidinates) and tris(amidinates) for MOCVD and ALD processes.

Sean Barry contributed data interpretation, writing and editing.

2.1 Abstract

Volatile metal complexes are important precursors for Chemical Vapour Deposition (CVD) and Atomic Layer Deposition (ALD) to deliver metal components to growing thin films. Ligands are critical design elements of such complexes, as their charge distribution, molecular weight, and coordination greatly influence the fragmentation of the precursor under deposition conditions. Compounds that are thermally stable enough to volatilize but that can also react with a specific substrate are uncommon and remain unknown for many metal centres. Guanidinate ligands, as demonstrated in this review, have proven their utility for CVD and ALD precursors across a broad range of metal centres. By tuning process parameters like co-reagents or temperature, metal oxides, metal nitrides or pure metallic films can be deposited from guanidinato complexes. Our review highlights interesting literature trends from the past five years and provides an outlook for the future of guanidinate complexes in ALD and CVD. The unique electronic and steric tunability of guanidinate ligands will permit the growth of a large library of versatile metal precursors.

2.2 Introduction

In recent years, the nanoscale thin film deposition methods of chemical vapour deposition (CVD) and atomic layer deposition (ALD) have become common for growing nano-thin coatings to keep pace with industrial demand for smaller, more sophisticated microelectronic devices.[1–6] New precursor compounds for vapour deposition are uncommon, as they must delicately balance thermal stability and reactivity, amongst other criteria. Some of the earliest volatile precursors employed halide ligands, which can enable volatility of relatively heavy metals (e.g., lead, tungsten).[7] However, high levels of halide impurities have been reported in such films and these impurities can act as electron sinks and deteriorate the functional properties of the film. As precursor design evolved, alkyl, cyclopentadienyl, alkoxy, beta-diketonate ligands and combinations thereof were reported in the literature. For a broader scope of precursors and deposited materials, please consult the comprehensive review by Puurunen from 2013.[7]

To the best of our knowledge, the earliest report of using guanidinates in volatile complexes for thin film deposition was reported by Claire Carmalt in 2005.[8] Employing the previously known monoguanidinato complex $TiCl_2[(^iPrN)_2CNMe_2]$ and the newly synthesized $Ti(NMe_2)_2Cl[(^iPrN)_2CN(SiMe_3)_2]$, titanium carbonitride films were grown at 600ºC under low-pressure CVD conditions.[8] Guanidinate ligands quickly became a welcomed addition to library of ligands suitable for CVD and ALD precursors and a variety of metal-containing guanidinate compounds with intriguing thermal properties have been reported

since. Recent studies of guanidinate compounds and their applications in CVD and ALD over the past five years will be summarized and discussed as the topic of this overview.

2.3 Results and Discussion

Metal Guanidinate Complex Synthesis and Mechanism

Two of the most straightforward approaches to the synthesis of metal guanidinate complexes are salt metathesis and carbodiimide (CDI) insertion. Salt metathesis is a well understood and widely used synthetic technique whereby a metal halide is reacted with a metalated ligand anion. Preparation of metal guanidinate complexes by this method is straightforward; it must be done slowly, at low temperature and in dilute solution to mitigate the heat released by this highly exothermic reaction. Once the resulting salt is removed, the product can usually be isolated in good yields by distillation, sublimation, or recrystallization from an appropriate solvent.

The second method of metal guanidinate complex synthesis, CDI insertion, begins with a metal amide complex. Adding the desired molar equivalents of a CDI reagent (such as diisopropylcarbodiimide) will insert into the M-N bond such that the metal-based NR_2 moiety becomes the exocyclic group in a chelating guanidinate ligand. This approach is analogous to CDI insertion with a metal alkyl species to form amidinate complexes. It should be noted that the stabilities of the mono-guanidinate species as compared to the stabilities of the multi-guanidinate species could skew synthesis in favour of the most stable compound. In

particular, ligand exchange processes can make isolation of the desired stoichiometric product difficult if it is not the most stable species. For example, the synthesis of tris(guanidinato) species using CDI insertion with aluminum and gallium was rapid (taking minutes) and complete, while the synthesis of the mono-substituted species required much longer reaction times (several hours) to achieve good yields.[9] Early NMR spectra of the reaction mixtures showed the presence of mono-, bis-, and tris(guanidinato) compounds in the reaction vessel, supporting the notion that rapid formation of the tris-species was then followed by the slower process of ligand exchange to form the stoichiometric product (Figure 2.3.1). Further experiments suggested that an intact ligand transfer is favoured over the CDI deinsertion/reinsertion process.[10]

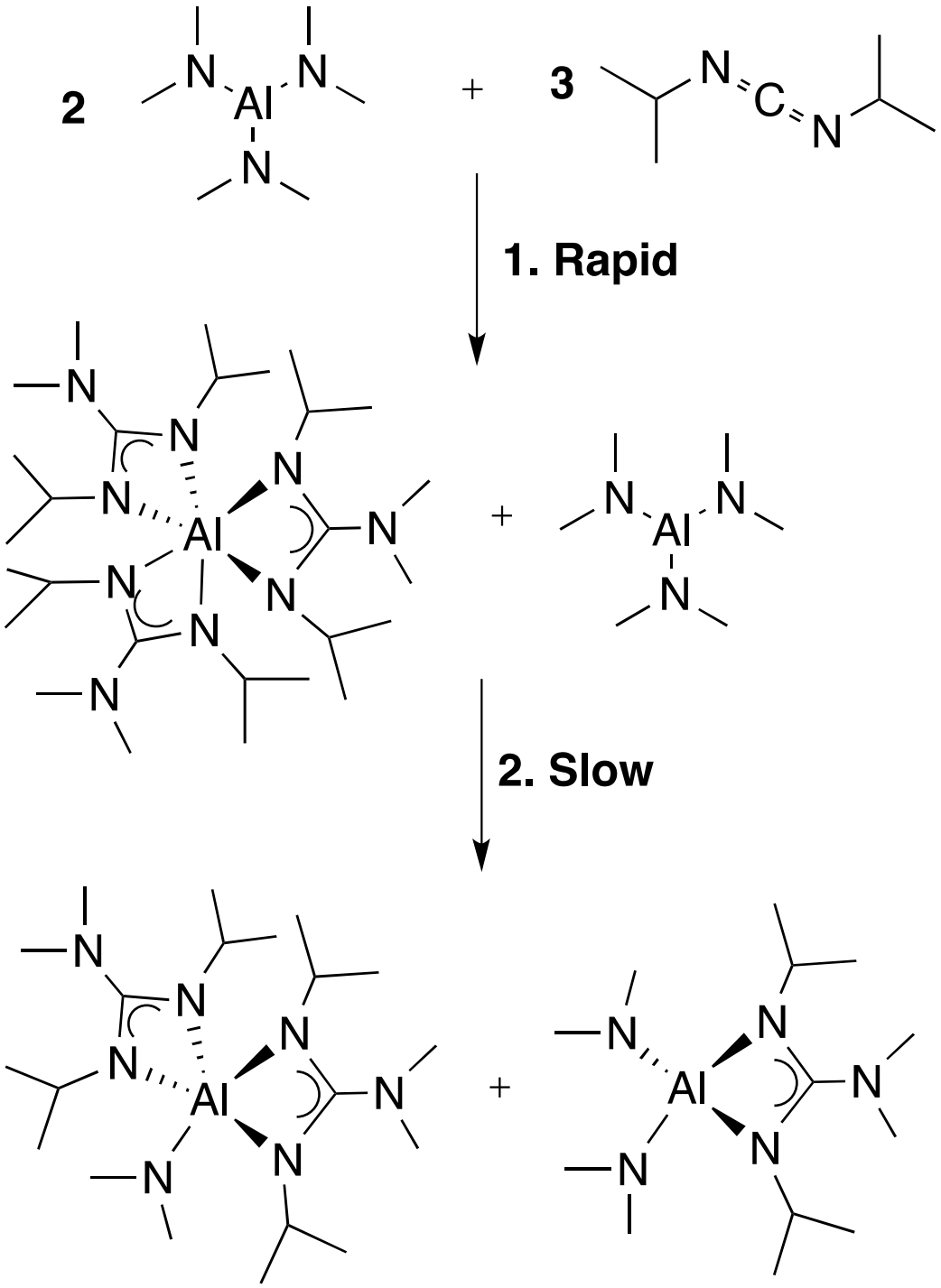

Figure 2.3.1: Reaction scheme of 1) rapid tris(guanidinato)Al(III) complex formation by CDI insertion, followed by 2) slow ligand exchange to form bis- and mono- substituted Al (III) species.

Contribution of Guanidinates to Precursor Development

Guanidinates used as anionic ligands became notable for their versatility and utility as ancillary ligands in precursor complexes due to their interesting electronic properties. The specific reactivity of guanidinates is fundamentally attributed to the three stabilizing resonance structures (Figure 2.3.2).

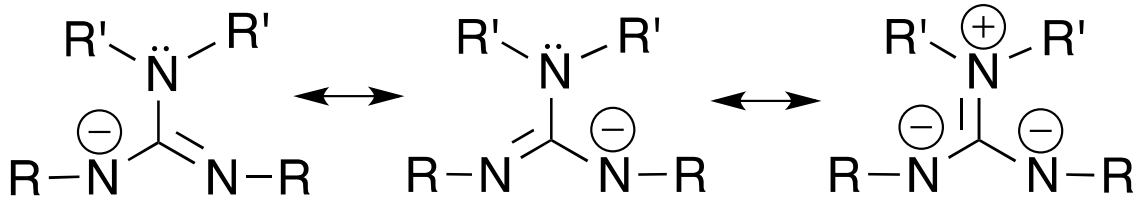

Figure 2.3.2: Resonance structures of a general guanidinate ligand.

Particularly, the electronic resonance structure of guanidinate ligands where the π electrons are shared with the secondary amino group renders these ligands highly tunable to suit the needs of a variety of metal centers and adds an extra degree of reactivity to the metal complex. Guanidinates are easily customizable in the R and R' position and easily synthesized as described above. Edelmann published an excellent review of guanidinate ligands and derivatives in 2012.[2] Guanidinate compounds are all-N-coordinating ligands and have thus become popular for the deposition of nitride films. Gadolium nitride and dysprosium nitride films were deposited by CVD using tris(N,N'-diisopropyl-2-dimethylamido-guanidinato)Ln(III) (Ln = Gd, Dy) as single source precursors and also with the aid of ammonia as a co-reagent .[11] Oxygen has also been used as a co-reagent to deposit ZrO_2,[12] TiO_2,[13] HfO_2,[14,15] oxides of some lanthanide metals,[11,16,17] as well as lanthanide-doped metal oxide films.[1] A dimeric copper (I) guanidinate,

[(N,N'-diisopropyl-2-dimethylamido-guanidinato)copper(I)]$_2$, has been used to deposit copper metal nanoparticles onto flat substrates[18] and optical fibers.[19] These examples demonstrate the versatility of guanidinate compounds to deposit metal oxide, nitride and metallic thin films. As tabulated in Table 2.3.1, many different growth rates, deposition conditions and type of substrates have been investigated. CVD growth of materials tends to be performed at high substrate temperatures, anywhere from 275-850ºC. Extreme conditions such as these lead to rapid film growth as exemplified by Kim et. al. for titania, where a growth rate of 180nm/min was reported.[13]

Impurities in CVD films can often be problematic but are process dependent and vary greatly from one case to another. Carbon impurities from the combustion of ligands are very common and difficult to remove once incorporated into the material. Post-deposition cleanup methods such as annealing at high temperatures under inert gases can be employed but this can add stress or strain to the material by altering the crystallinity. Over the past several years, more careful and well-designed processes have greatly improved on this problem. Ligand design is integral to this and depositions using guanidinate compounds in the literature consistently report low impurities, often < 3% (Tables 1 and 2).

Table 2.3.1: Summary of Chemical Vapour Deposition (CVD) with Guanidinate Precursors

Target material	Substrate	Precursor	Co-reagent	Deposition T (ºC)	Growth Rate (nm/min)	Impurities	Year Reported
TiO_2	Si (100); ITO-coated glass	$Ti(NMe_2)_3(guan)$	O_2	400 – 700	180 @ 600ºC	C: < 6%	2013[13]
Cu(0)	Optical fiber	$[Cu(guan)]_2$	None	200	1.52 nm/cycle*	NR	2011[19]
ZrO_2	Al-back contact c-Si	$Zr(NEtMe)_2(guan)_2$	O_2	500 – 600	8.74	NR	2009[12]
ZrO_2	Glass	$Zr(CpMe)(\eta^1\text{-guan})_2Cl$	Air	500 – 600	NR	5-18%	2009[32]
In_2O_3	Si (100) Glass	$In(guan)_3$	Air	275 – 350	43	In(0): < 2%	2011[4]
HfO_2	Si (100)	$Hf(\eta^2\text{-guan})_2Cl_2$[A], $Hf(\eta^2\text{-guan})_2Me_2$[B]	O_2	300 – 700	NR[A]; 7.3 @ 700ºC[B]	None	2010[28]
HfO_2	Si(100)/SiO_2	$Hf[(NR')(NR'')CNMe_2]_x(NR_2)_{4-x}$, $Hf[(NR')(NR'')CNEt_2]_x(NR_2)_{4-x}$, R = Me, Et; R' ≠ R"= Et, ^{i}Pr, ^{t}Bu; x = 1,2	O_2	350 – 580	NR	NR	2009[15]
Sc_2O_3[A] Er_2O_3[B] Y_2O_3[C]	Si (100)	$Ln(III)(guan)_3$	O_2	350 – 700	9.1[A]; NR[B]; 11.1[C]	C: ~3%; N: ~1%	2012[17]
$HfGdO_x$[A] $HfDyO_x$[B]	Si (100)	$Hf(NMe_2)_2(guan)_2$ $Ln(III)(guan)_3$	O_2	300 – 700	30 @ 700ºC[A,B]	negligible	2012[1]
Gd_2O_3[A] Dy_2O_3[B]	Si (100); Al_2O_3 (0001)	$Ln(III)(guan)_3$	O_2	300 – 700	Si: 15.3 @ 600ºC[A]; Si: 12.2 @ 600ºC[B]	C,N:< 3%	2009[22]
Gd_2O_3[A] GdN[B]	Si (100); Al_2O_3 (0001); glass	$Gd(guan)_3$	O_2; None	300 – 700[A]; 550 – 850[B]	Si: 3.7 @ 300ºC[A]; Al_2O_3: 16.6 @ 600ºC[A]	C: 3.29 %; N: 3.78 %	2009[23]
GdN	Al_2O_3	$Gd(guan)_3$	None	650 – 850	30	Low O	2009[16]
GdN[A] DyN[B]	Si (100)	$Ln(III)(guan)_3$	None; NH_3	650 – 850	8 @ 850ºC[A]; 16 @ 850ºC with NH_3[B]	complicated	2011[11]

Abbreviations: guan = $[(^iPrN)_2C(NMe_2)]$; not reported = NR; *pulsed CVD

Copper Metal Deposition by CVD

The Barry group reported a modification to typical CVD processes in 2011. This process deposited copper metal onto optical fibers for sensing applications.[19] A dimeric Cu(I) complex, [(N,N'-diisopropyl-2-dimethylamido-guanidinato)copper(I)]$_2$ was the precursor and performed well under the relatively mild, 200ºC reactor temperature. Pulsed-CVD was used whereby the precursor was released into the reactor through computer-controlled pneumatic valves in short bursts. This modification to a typical precursor delivery system aided in slowing down the growth rate and offered better thickness control. This is not to be confused with an ALD process because no self-limiting growth was achieved. Compared to most CVD processes, 200ºC is a relatively low deposition temperature and partly responsible for the slow growth rate of 1.52nm/cycle.

Another interesting feature of this work was that no secondary precursor was necessary to remove the ligand system and reduce Cu(I) to Cu(0). In this case, the Cu(I) guanidinate acts as a single source precursor where the guanidinate is the reducing agent. A gas-phase thermolysis study was undertaken using time of flight mass spectroscopy (TOF-MS), matrix-isolation FTIR, and DFT calculations to determine how the precursor managed to reduce the copper autonomously.[10] It was determined that at temperatures greater than 150ºC, the dimer can undergo a rearrangement to form a copper hydride that subsequently bridges the copper centers and releases a neutral oxidized guanidine-type ligand (Figure 2.3.3).

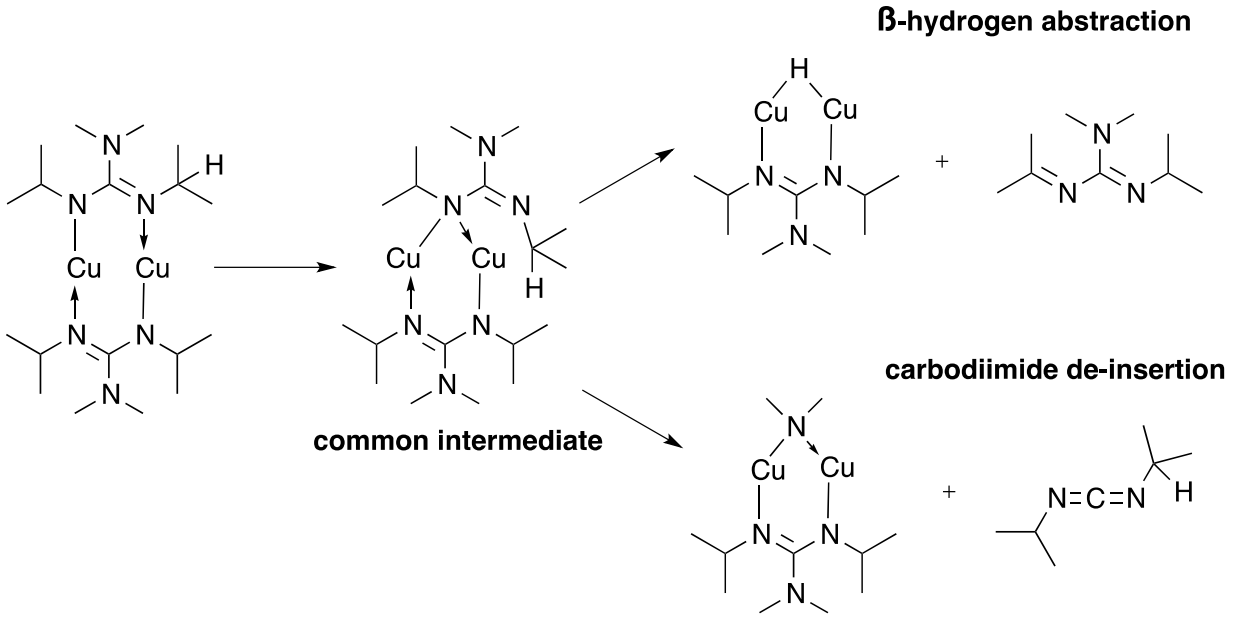

Figure 2.3.3: DFT-calculated fragmentation pattern of Cu(I) guanidinate compound.

Detection of CDI at elevated temperatures also supports a thermodynamically favourable CDI-deinsertion pathway – a reversal of the guanidinate ligand synthetic procedure. Reactivity at low temperature on a nickel (110) surface using X-ray photoelectron spectroscopy (XPS) and temperature-programmed desorption also corroborated the single source reactivity of the precursor.[20] These studies demonstrated the complexity of the thermal decomposition of this Cu(I) guanidinate precursor.

Versatility of Metal Guanidinate Precursors

Interestingly, there are many commonalities between CVD and ALD precursors and some compounds have shown to perform well in both processes. In these cases, the lower available thermal energy due to decreased reactor temperatures results in self-limiting growth that is characteristic of ALD.

Table 2.3.2: Summary of Atomic Layer Deposition (ALD) with Guanidinate Precursors

Target Material	Substrate	First Precursor	Second Precursor	Deposition T (ºC)	Growth Rate (Å/cycle)	Impurities	Year Reported
TiO_2	Si (100)/SiO_2	$Ti(NMe_2)_3(guan)$	H_2O	150 – 330	0.4-0.7	C: < 5%; N: < 4%	2013[33]
In_2O_3	Si (100); Al (0001); glass	$In(guan)_3$	H_2O	160 – 320	0.4-0.45	C: < 2%	2014[21]
HfO_2	Si (100)	$Hf(NMe_2)_2(guan)_2$	H_2O	100 – 300	1.0-1.2 @ 100-225ºC	C detected, % NR	2012[3]
Ta/TaN	NR	$Ta(NEt_2)_4[\eta^2$–^{i}PrNC(NEt_2)NEt]	NH_3	260	NR	NR	2011[5]
Gd_2O_3	Si (100)	$Gd(guan)_3$	H_2O	225	NR	NR	2010[24]
Gd_2O_3	Si (100)	$Gd(guan)_3$	H_2O	175 – 275	1.1	NR	2010[6]
Gd_2O_3 Dy_2O_3	Si (100)	$Gd(guan)_3$ $Dy(guan)_3$	H_2O	150 – 350	1.1 @ 175-275ºC[A] 1.0 @ 200-275ºC[B]	C, N: < 2 %	2012[25]
Er_2O_3	Si (100)	$Er(guan)_3$	H_2O	150 – 350	1.1	None	2013[34]

Abbreviations: guan = $[(^i PrN)_2C(NMe_2)]$;, not reported = NR

Table 2.3.2 shows that not only are the process temperatures lower, but also the film growth rates are much lower. The tris(N,N'-diisopropyl-2-dimethylamido-guanidinato) indium(III) complex is an excellent example of such a compound. CVD grown indium oxide films deposited at 275 – 350ºC with humid air as a co-reagent achieved a growth rate of 43 nm/min.[4] Very recently, the same precursor has demonstrated self-limited growth of indium oxide in a water-assisted process between 160 – 320ºC at a rate of 0.4 – 0.45Å/cycle.[21] No In(0) impurities were reported in either example, although low carbon impurities were noted. Thus this tris(guanidinato) indium complex shows slow, careful ALD growth at 160ºC and rapid CVD growth at 350ºC. The overlap of these temperatures ranges from 275 – 320ºC with a transition from pure layer-by-layer

ALD growth (lower temperatures) to a CVD-like growth, which becomes more dominant at higher temperatures.

Homoleptic tris(guanidinato) lanthanide compounds, analogous to the tris(guanidinato) Al complex shown in Figure 2.3.1, have been thoroughly studied by Devi and show distinct CVD and ALD growth under different process conditions. In 2009, this group reported tris(N,N'-diisopropyl-2-dimethylamido-guanidinato)gadolinium(III) ($Gd(DPDMG)_3$) as a SSP for CVD of GdN films, achieving a growth rate of 30nm/min at temperatures between 650 – 850ºC.[16] This was the first reported CVD approach to growing rare earth metal films and many other studies have stemmed from its success. In 2011, Devi reported further studies using this compound as well as the analogous dysprosium compound, tris(N,N'-diisopropyl-2-dimethylamido-guanidinato)dysprosium(III) ($Dy(DPDMG)_3$) and compared the resultant rare earth nitride films with films grown using very similar Ln(III)(N,N'-diisopropyl-acetamidinate)$_3$ complexes.[11] The SSP nature of these compounds was highlighted in this study, where it was directly compared to the analogous amidinates. In both the DyN and GdN cases, the amidinate complexes were not suitable as SSPs. Even at process temperatures up to 850ºC the resulting films were amorphous, showing high amounts of carbon impurities due to a preferred incorporation of C over N. However, both could be counteracted by the use of NH_3 as a co-reagent. Under SSP conditions, carbon impurities were much lower in the films grown with guanidinate precursors, indicating that the fragments released from these precursors during the deposition process advantageously removed more carbon

than did amidinate analogues. Electron ionization and high resolution mass spectroscopy (MS) were used to further examine possible decomposition routes.[11] The MS evidence suggested that the detected imido species (Figure 2.3.4) were likely the species that contributed to inclusion of nitrogen into growing films.

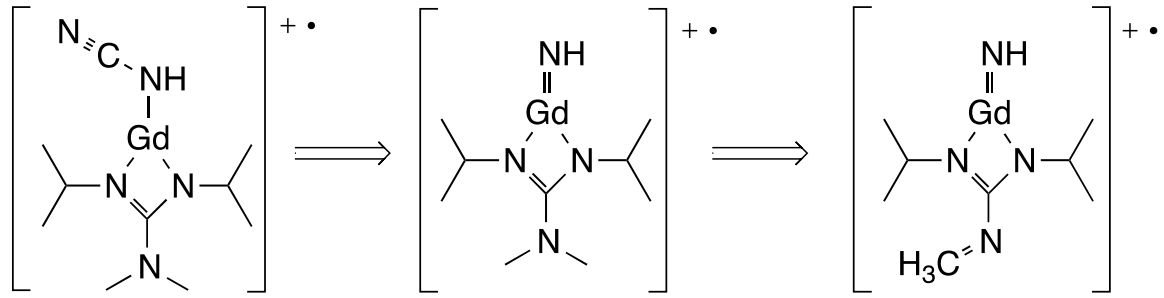

Figure 2.3.4: Selection of proposed fragmentation pattern of $Gd(DPDMG)_3$, under MS conditions (EI-MS, 70 eV) highlighting imido species products.

However, it is noteworthy that the conditions of EI-induced fragmentation in high vacuum and the thermally activated fragmentation under CVD conditions at reduced pressure cannot be directly compared. The guanidinate compounds were further shown to deposit both rare earth metal and nitrogen film components, as the NH_3 co-reagent did not have significant effect on the stoichiometry of the films. Gd_2O_3 films grown by CVD in the presence of oxygen, in the 300 – 700ºC temperature range were also reported using $Gd(DPDMG)_3$.[22,23]

Devi also explored the possibility of these compounds showing self-limited growth with ALD at lower temperatures. The first communication confirming this behavior was in 2010, with the growth of Gd_2O_3 films at a rate of ~1.1Å/cycle

over the temperature range of 175 – 275ºC using water as the second precursor.[6] The excellent growth and nucleating behavior was attributed to the high basicity of the guanidinate ligand, which allowed rapid reaction with surface hydroxyls as well as with the second precursor.[6] Further improvement on this process was reported, when forming gas annealing at 450ºC was employed after deposition to films grown at 225ºC.[24] Interface defect density was considerably lowered, which improved electrical properties and had positive implication for further downscaling of electrical devices.[24] Dy_2O_3 films were grown at a rate of 1.0Å/cycle between 200 – 275ºC using the previously discussed $Dy(DPDMG)_3$ precursor and the same beneficial effect of forming gas annealing was reported.[25] These compounds strongly demonstrate the versatility of guanidinate ligands for both CVD and ALD applications.

Future Directions and Perspective

The potential of many homoleptic and hetereoleptic guanidinate complexes with electropositive metals have been thoroughly explored with respect to their volatility and thermal properties. Many compounds have not demonstrated film growth yet, but have been tested for precursor candidacy. These are tabulated in Table 2.3.3 and give insight into the direction that guanidinate ligands are headed and the types of compounds that may be reported in future works.

Table 2.3.3: Thermolysis Studies of New Guanidinate CVD and ALD Precursors

Target Component	Precursor(s)	Summary of Data Collected	Year Reported [ref]

Ti	$TiCp_2[(N^iPr)_2CNRR']$ R, R' = H, Me, ^{i}Pr	mp: 147-165ºC; Onset of volatility: 147 - 168ºC; Residual mass: 8.5-0%; Reactivity on high surface area SiO_2	2010 [35]
Cu	$[Cu(guan)]_2$	Gas-phase fragmentation	2010 [10]
Cu	$[Cu(guan)]_2$	Reactivity with Ni (100) substrates	2013 [20]
Cu	$[Cu(^iPrN)_2CN^iPr_2]_2$[A] ; $[Cu(^iPrN)_2CNEt_2]_2$[B]	Sublimation: 130ºC at 80 mTorr[A], 130ºC at 85 mTorr[B]; Onset of volatility: 87.5ºC[A], 78.1ºC[B] Residual mass: 21.4%[A]; 19.1%[B]	2011 [36]
Ge	R*GeN($SiMe_2CH_2CH_2Me_2Si$)	Monomer; mp: 100ºC	2009 [26]
Ge	$(TMG)_2Ge(NMe_2)_2$[A]; $(TMG)_2Ge(NEt_2)_2$[B]	mp: 46.7ºC[A], liquid[B]; Onset of volatility: 190ºC[A], 203ºC[B]; Residual mass: 3%[A], 0%[B]	2010 [27]
MoN	$Mo(N^tBu)_2(guan)(X)$; $Mo(N^tBu)_2(guan)_2$ X = Cl[A], I[B], N_3[C]	B: TBD; mp: 120ºC[A], 79ºC[C]; Onset of volatility: 130ºC[A], 135 ºC[C] Residual mass: 43%[A]; 29%[C]; sublimable, potential CVD precursors	2009 [30]
Ag	$[Ag(^iPrN)_2CN^iPr_2]_3$[A]; $[Ag(^iPrN)_2CNEt_2]_3$[B]	Onset of volatility: 58.4ºC[A], 99.4ºC[B] Residual mass: 33.8%[A]; 36.0%[B]	2011 [36]
Hf	$HfCl_2(NSiMe_3)[(^iPrN)_2CN(SiMe_3)_2]$	Not volatile but reactive with isopropanol	2010 [28]
Ta	$Ta(NMe_2)_4[\eta^2$-^{t}BuNC$(NMe_2)(NEt)]$	mp: 66.7ºC; Onset of volatility: 170ºC; Residual mass: 1.6%	2010 [29]
Au	$[Au(guan)]_3$[A];$[Au(^iPrN)_2CN^iPr_2]_2$[B]; $[Au(^iPrN)_2CNEt_2]_2$[C]; $[Au(^iPrN)_2CNMe_2]_2$[D]; $[Au(^iPrN)_2CNMe]_2$[E]; $[Au(^iPrN)_2CN^nBu]_2$[F]	Sublimation: 85ºC at 20 mTorr[D]; Onset of volatility: 114.9ºC[A], 25.5ºC[B], 100.5ºC[C], 52.0ºC[D], 79.5ºC[E], 132.3ºC[F]; Residual mass: 41.0%[A]; 46.0%[B], 50.0%[C]; 4.0%[D], 14.2%[E]; 54.1%[F]	2011 [36]
WN_xC_y	$W(N^iPr)(guan)Cl_3$	DFT of gas-phase decomposition	2010 [31]

Abbreviations: guan =$[(^iPrN)_2C(NMe_2)]$; TMG =N,N,N',N'-tetraalkylguanidinate; R* = $[^iPrNCN(SiMe_2CH_2CH_2Me_2Si)N^iPr]$

An interesting germanium guanidinate compound (Figure 2.3.5a) with a cyclic bis(dimethylsilyl)ethane substituted nitrogen in the exocyclic position was reported in a short communication in 2009.[26] With a facile synthesis, melting point of 100ºC and an 88% yield, further study to determine volatility would be very interesting. The exocyclic position not only adds stability to the structure through resonance, but careful substitution there may also favorably change the

electronic and thermal properties of the compound. Another interesting family of Ge bis(guanidinate) compounds (Figure 2.3.5b), reported in 2010 had two (N,N,N',N'-tetramethyl) substituted guanidinates bound to the Ge (IV) centre through the unsubstituted nitrogens.[27]

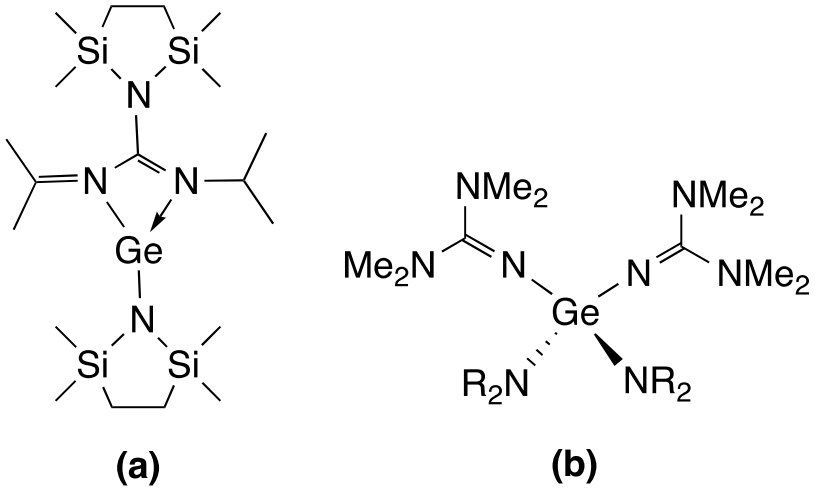

Figure 2.3.5: a) Substituted mono(guanidinato) Ge compound; b) bis(guanidinato) Ge monomer where R= Me or Et.

Volatility was tuned by altering the R groups on the other amido moieties. The compounds were reported to show onset of volatility, as determined through thermogravimetric analysis, below 200ºC and residual masses were <5%. From these data, these compounds would be excellent candidates for CVD or ALD applications and perhaps other chalcogenide analogues would exhibit similar thermal properties.

Trimethylsilyl substitution in guanidinates has also been tested on hafnium complexes but so far, without success. Although the candidate $HfCl_2(NSiMe_3)[(^iPrN)_2CN(SiMe_3)_2]$ was not volatile, this was the first report of such a hafnium complex.[28] Since reaction with isopropanol at the chloro moieties was demonstrated, perhaps alternative substitutions could be explored to render the compound volatile. Asymmetric substitutions to the chelating nitrogens have also demonstrated promising thermal properties in Ta complexes.[29] New metal centres are also under investigation with guanidinates, such as copper[10,19,20] , molybdenum[30], tungsten[31], silver[36] and gold.[36]

2.4 Conclusions

Recent literature is trending towards novel guanidinate modification that consequently changes electronic properties of the ligand and thus the metal complex. Guanidinates naturally lend themselves to substitutions on the nitrogen atoms, which is what makes this ligand so attractive. Volatility of ALD and CVD precursors is of utmost importance and the versatility of guanidinate structures is attractive for tuning this property. They are relatively new ligands in the CVD and ALD field and already oxide, nitride and pure metal films have been deposited. In the coming years, a rich selection of guanidinate metal complexes will likely emerge as their thermal properties become more understood and predictable and will be developed for CVD and ALD.

Chapter 3 – Heteroleptic Iminiopyrrolidinates of Aluminium

Please see preface, page 3, for more details and full article citation. Author contributions listed below are paraphrased from signed Letters of Permission to reprint this material.

Agnieszka Kurek is second author of this research paper. Her contributions to this published work included experimental work (compound synthesis and thermal analysis), writing, editing and figure composition. Please see preface, page 3, for more details and full article citation.

Yamile Wasslen contributed writing, experiments, collaborating with Kurek on ideas and data analysis.

Paul Johnson synthesized some iminopyrrolidine ligands.

Taylor Pigeon contributed supporting information and data.

Wesley Monillas and Glenn Yap contributed crystal structure collection and data interpretation.

Sean Barry contributed data interpretation, writing and editing.

3.1 Abstract

A series of iminopyrrolidine (ip) compounds were synthesized with excellent yields as potential ligands for novel organometallic precursors for atomic layer deposition. The idea behind these ligands was that CDI deinsertion would not occur as the quaternary carbon was tethered to one chelate nitrogen. To our advantage, a melting point trend was evident within the ip ligands and reflected in the family of heteroleptic aluminum species when the ip ligands were reacted with trimethyl aluminum (TMA) or triethylaluminum (TEA). The alkane elimination reaction occurred at room temperature yielding clean products with high yields. Crystal structure data were collected for compounds **7** [ipipAlMe_2], **12** [tbipAlMe_2], and **14** [sbipAlEt_2] demonstrating that the heteroleptic aluminum species were dimers. This was also evident in the mass spectra collected for each compound as the parent peak was that of the dimer minus a methyl. Thermolysis studies were carried out on all the ipAlMe_2 species to observe the decomposition at an isotherm over several days. The decay of the methyl peak was monitored as a ratio against tetramethylsilane (TMS) within the solution and was shown to be a first order decomposition. From these studies it was clear that nbip (**9**), iso-bip (**10**), and tbip (**12**) were the most stable complexes with half-lives of 24.8, 9.00, and 10.3 days, respectively.

3.2 Introduction

Amidinates and guanidinates have been widely used as alternatives to cyclopentadienyl ligands in organometallic chemistry.[37–39] These ligands have been used with metals across the periodic table to make organometallic complexes for catalysis[40,41] as well as potential precursors for processes in material science and nanotechnology such as metal organic chemical vapour deposition (MOCVD) and atomic layer deposition (ALD).[42–44]

As nanotechnology becomes increasingly prevalent, the desire to make smaller scale architectures and thinner films is a mounting challenge. MOCVD and ALD are close cousins for the fabrication of thin films. They differ in the way in which the precursor is handled, which greatly affects the surface chemistry of the process. MOCVD introduces both precursors into the reaction chamber simultaneously where they are allowed to form the thermodynamically determined film. ALD has more control on the uniformity and the thickness of the film by introducing the precursors in intervals to the reaction chamber separated by purge steps to remove any volatile by-products. This process requires a self-limiting monolayer of precursor to form at the substrate, which consequently allows greater thermodynamic control. Self-limiting monolayer formation occurs because the surface reactions are limited by the number of reactive surface sites and no further reactions occur on the surface once these sites are occupied. This complete monolayer saturation prevents continual growth of the film by inhibiting further reactions at the surface.

In order for an ALD precursor to be successful, it must meet several criteria. It must have high volatility; which can be achieved by keeping the molecular weight low and by having asymmetric[45] as well as branched ligands.[46] The metal center must be coordinatively saturated, or at least sterically congested to prevent oligomerization, which also promotes self-limiting behaviour. The compound must be chemically reactive towards a substrate but must be thermally stable such that it can resist decomposition at elevated temperatures. Control of the thermal reactivity is paramount. The ability to tune the thermal reactivity through the ligand design of the compound is a significant goal in precursor design.

Amidinato and guanidinato anions of the general formula $[RC(NR')_2]^-$ and $[R_2NC(NR')_2]^-$ (where R = H or alkyl and R' = alkyl) are commonly found as ligands on precursors for ALD due to their tunable properties which allow control over volatility and melting point.[47] The flexibility to change the steric and electronic properties of these ligands is highly attractive. However, mechanistic investigations of these ligands have revealed that deinsertion of CDI from the parent guanidinate or amidinate at elevated temperatures can occur (Figure 3.2.1).[48]

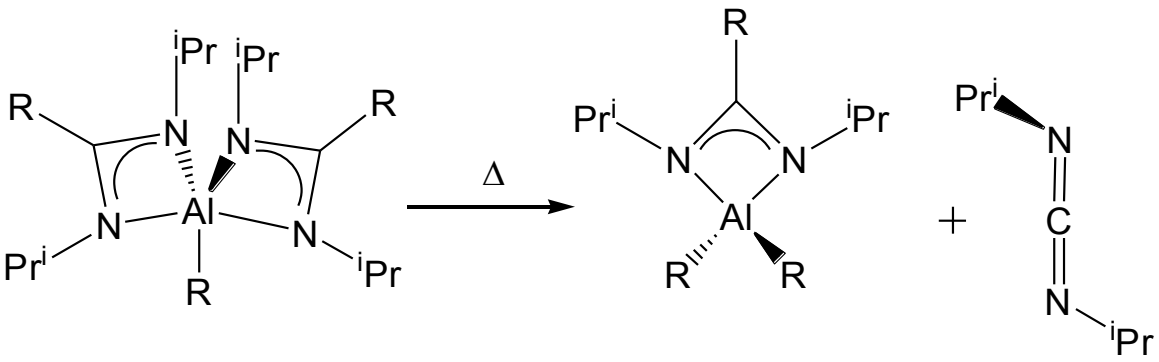

Figure 3.2.1: Deinsertion of carbodiimide (CDI) at elevated temperatures.

The search for a ligand that does not deinsert CDI but maintains the chelating geometry and (importantly) the flexibility of an amidinate or guanidinate was undertaken. The iminopyrrolidinate ligand is monoanionic like its amidinate counter part; however the sp^2 carbon is tethered to one of the chelating nitrogens (Figure 3.2.2). This type of structure prevents CDI deinsertion because rearrangement to produce CDI is highly unfavourable.

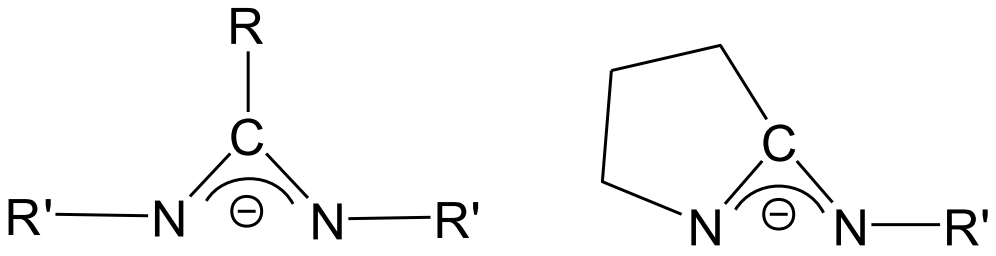

R = H or alkyl
R' = alkyl

Figure 3.2.2: The similarity in chelating geometry of an amidinate and an iminopyrrolidinate.

Iminopyrrolidine-based ligands, such as amidinates, can be easily tuned to decrease melting point by changing the length and controlling the branching of the alkyl chain bonded to the acyclic nitrogen. The asymmetry of the ligand is a desirable feature as it can increase volatility of organometallic complexes. Herein, the synthesis of the propyl and butyl iminopyrrolidines and their reactivity to make methyl aluminum derivatives, as well as the thermolysis of the compounds are reported.

3.3 Results and Discussion

A straightforward synthetic route (Figure 3.3.1) for iminopyrrolidines (**1 – 6**) was achieved after combination and modification of the experimental from two previously reported syntheses.[49,50] Indeed, careful and technical execution of the procedure is crucial to achieving a good yield for these ligands. Thus, the synthetic procedure will be discussed in detail.

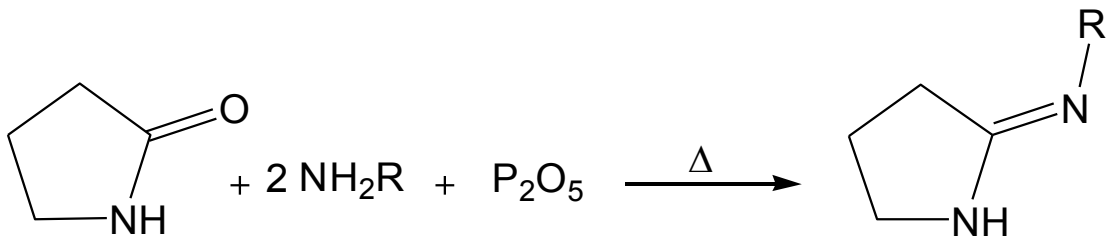

R = propyl, iso-propyl, butyl, iso-butyl, sec-butyl, tert-butyl

Figure 3.3.1: Synthetic procedure for iminopyrrolidine ligands.

Due to the high volatility of the amines, the molar ratio of the amines was increased compared to the literature preparation. The amine was mixed with the 2-pyrrolidone and added to the neat P_2O_5 through a reflux condenser; a longer

reflux condenser was used in an attempt to contain the amine during the reaction. Very importantly, the source of heat was changed from an oil bath to a sand bath. The sand bath proved to have less heat loss to the surroundings than an oil bath and so it was much easier to control and quicker to reach reflux temperatures.

The reaction reached completion after 2 hours of refluxing and was allowed to cool to a glassy solid. Instead of dissolving the solid in ice, 40 mL of distilled water was used with the aid of a heat gun and vigorous agitation. The strength of the base was increased to 6M NaOH to avoid the addition of excess water: iminopyrrolidines are soluble in water.

By simply implementing these changes, excellent yields of the purified ligands were achieved with the exception of the tert-butyl (tbip) derivative. Here, the steric bulk of the parent amine is cumbersome, and causes the discrepancy in yield. All six ligands were room temperature solids, and were sublimed under reduced pressure between 60 – 65°C (Table 3.3.1).

Table 3.3.1: Yields and Melting Points of Iminopyrrolidine Ligands

Compound	R	Crude yield (%)	Sublimed yield (%)	Melting Point (°C)
1	Iso-propyl (ipip)	81	78	99 – 100
2	N-propyl (npip)	85	72	72 – 74
3	N-butyl (nbip)	87	75	55 – 56
4	Iso-butyl (ibip)	79	73	102 – 103
5	Sec-butyl (sbip)	80	76	98 – 100
6	Tert-butyl (tbip)	40	30	108 – 110

The bench top melting point values of each ligand were compared with the exothermic peaks of the differential scanning calorimetric results. There was a definite melting point trend associated with the alkyl moiety on the ligand. N-propyl iminopyrrolidine (npip, **2**) has a lower melting point than ipip (**1**), as there is a larger degree of freedom for the n-propyl moiety than for the iso-propyl. This effect of lowering melting points was also evident when the n-propyl is considered with the n-butyl iminopyrrolidine (nbip, **3**), where the longer chain afforded a lowering of the melting point by roughly 18°C. As the branching increases from nbip (**3**) to tbip (**6**) the melting point also increases. Notably, there is a decrease in the melting point for sbip (**5**). This melting point depression is accredited to the fact that there is asymmetric branching around the amine as well as the fact that there are two stereoisomers due to the sec-butyl group.

Thermal gravimetric analysis of all six ligands was performed (Figure 3.3.2). Although nbip (**3**) had the lowest melting point, it is evident that it had the highest onset of volatility, followed by npip. This is attributed to steric factors, since a higher onset of volatility suggests stronger hydrogen bonding between the molecules. However, each ligand had a clean volatilization (only one feature in the TGA), demonstrating that they did not decompose under heat. The residual mass of each ligand was zero, also indicating a clean evaporation.

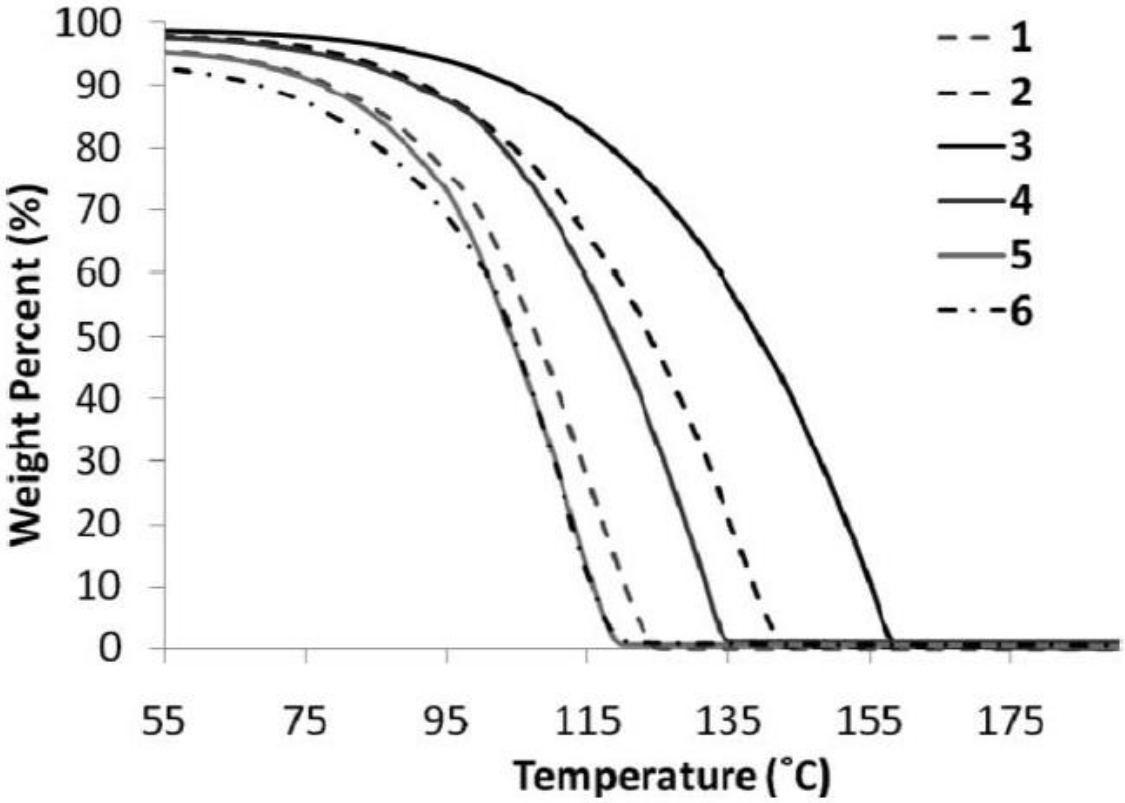

Figure 3.3.2: Thermogravimetric anaylsis of iminopyrrolidine ligands **1-6**.

TMA was used to make heteroleptic aluminum complexes containing these ligands with the general formula (ip)$AlMe_2$, where “ip” is the general iminopyrrolidine. A one-to-one ligand to TMA reaction in hexanes at room temperature was performed to synthesize all the dimethyl aluminum iminopyrrolidinate complexes (Figure 3.3.3). Methane elimination was the driving force of these reactions.

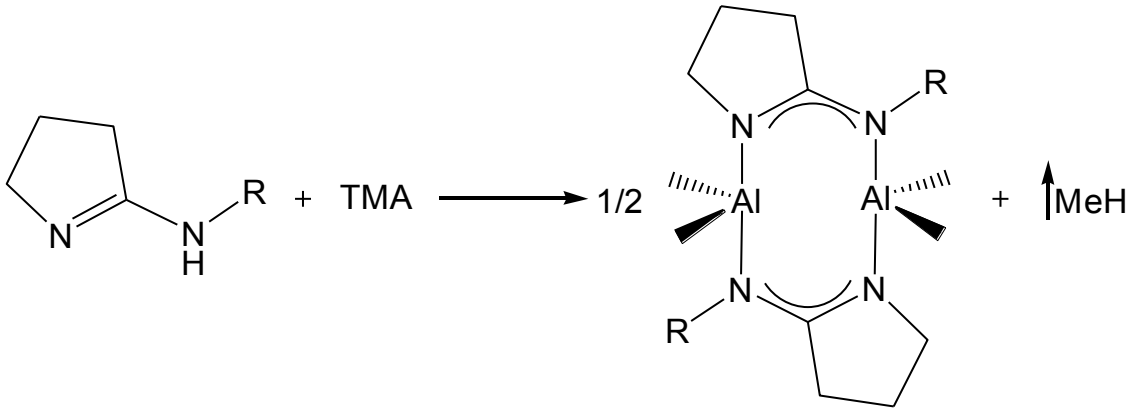

Figure 3.3.3: Synthesis of $AlMe_2$iminopyrrolidinate complexes.

Compounds **7** – **12** were colourless solids and all were purified by recrystallization (Table 3.3.2). Crystal structures for compounds **7** and **12** were collected, both of which were dimers (Figure 3.3.4). The ^1H NMR spectra for all six compounds were similar in their simplicity with no evidence of monomer-dimer equilibrium, and it is inferred from this data and mass spectrometry that compounds **7** – **12** were all dimers. This is likely due to the lesser steric demand of the ip ligands from the absence of a pendant "R" group on the cyclic nitrogen.

Table 3.3.2: Yields and Melting Points of Aluminum Dimethyl Iminopyrrolidinate Complexes

Compound	R	Yield (%)	Melting Point (°C)
7	Iso-propyl (ipip)	75	87 – 91
8	N-propyl (npip)	78	79 – 83
9	N-butyl (nbip)	84	68 – 70
10	Iso-butyl (ibip)	91	111 – 113
11	Sec-butyl (sbip)	90	62 – 65
12	Tert-butyl (tbip)	66	116 – 118

Compound **7** (ipipAlMe$_2$) was symmetrical, residing in a *P2$_1$/n* space group with an S_2 symmetry and a center of inversion residing at the molecular centre, and the aluminum in a distorted tetrahedral geometry (Tables 3.3.3 and 3.3.4). It was evident from the crystal structure that the π-system was localised within the chelate ring as the N1-C3 and N2-C3 bonds were shorter (1.329 Å and 1.331 Å respectively) than the N1-C6 and N2-C7 bonds (1.480 Å and 1.490 Å respectively). Also, C3 was planar with a sum of angles of 360.0°, indicating that it has an sp^2 hybridisation, allowing the remaining p orbital to participate in the π system. The nitrogen centres N1 and N2 were also very close to planar (sums of angles at 355.3° and 357.5° respectively). The N1-Al-N2 angle was 111.19°.

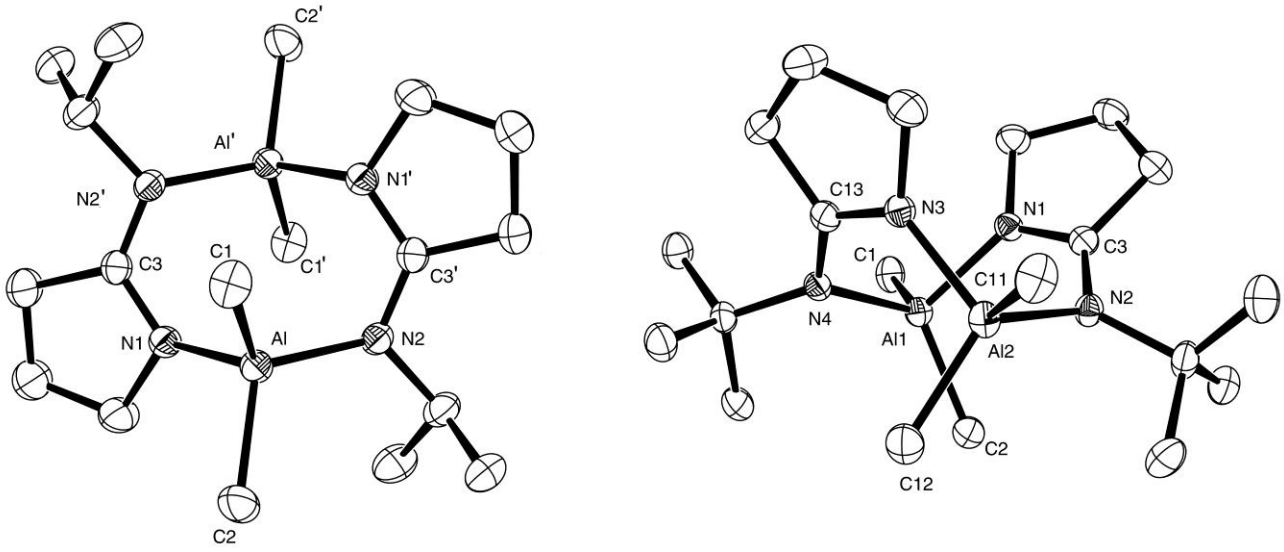

Figure 3.3.4: Molecular structures of **7** and **12**, respectively. Thermal ellipsoids are drawn at 50% probability, and the H atoms have been omitted for clarity.

Table 3.3.3: Metrical Data for ipipAlMe$_2$ (7)

Selected Bond Lengths (Å)			
Al – N(1)	1.926(2)	Al – C(2)	1.984(2)
Al – N(2)	1.931(2)	N(1) – C(3)	1.329(2)
Al – C(1)	1.969(2)	N(2)' – C(3)	1.331(2)
Selected Bond Angles (°)			
C(1)–Al–C(2)	109.34(10)	C(3)–N(1)–Al	125.01(11)
N(1)–Al–N(2)	111.19(6)	Al–N(2)–C(3)'	117.62(11)
N(1)–C(3)–N(2)'	122.57(14)		

Table 3.3.4: Metrical Data for tbipAlMe$_2$ (12)

Selected Bond Lengths (Å)			
Al(1) – C(1)	1.984(2)	Al(2) – N(2)	1.9376(18)
Al(1) – C(2)	1.970(2)	Al(2) – N(3)	1.9405(19)
Al(1) – N(1)	1.9242(18)	N(1) – C(3)	1.323(3)
Al(1) – N(4)	1.9353(18)	N(2) – C(3)	1.344(2)
Al(2) – C(11)	1.987(2)	N(3) – C(13)	1.318(3)
Al(2) – C(12)	1.966(2)	N(4) – C(13)	1.345(2)
Selected Bond Angles (°)			
C(1)–Al(1)–C(2)	109.87(9)	Al(1)–N(4)–C(13)	118.68(13)
N(1)–Al(1)–N(4)	102.22(7)	Al(2)–N(2)–C(3)	117.90(13)
C(11)–Al(2)–C(12)	111.20(10)	Al(2)–N(3)–C(13)	127.73(14)
N(2)–Al(2)–N(3)	103.33(7)	N(1)–C(3)–N(2)	121.61(17)
Al(1)–N(1)–C(3)	127.38(13)	N(3)–C(13)–N(4)	121.82(17)

The structure of **12** was also in a $P2_1/n$ space group, but without an inversion centre located in the molecule (Figure 3.3.4, Tables 3.3.3 and 3.3.4). Again, the aluminum had a distorted tetrahedral coordination. The additional bulk of the tert-butyl group caused the rings to "flip up" and bend the metallocycle into a boat conformation in **12** compared to the chair conformation in **7**. However, this steric effect does not change the ligand binding significantly. The sp^2 carbons, C3 and C13 were planar (sum of angles of 359.7° in both cases), with the N-C bond lengths to C3 and C13 being shorter then the bond lengths of the nitrogens bonded to the other C atoms due to their involvement in the π-system. The chelation angle of this dimer was similar in size to compound **7** at 121.6° and 121.8°, respectively (compared to 122.6° in **7**). The N1-Al1-N4 and N2-Al2-N3 (at 102.2° and 103.3°) were smaller compared to N1-Al1-N2 in compound **7** (at 122.6°). It should be noted that **12** showed C2 symmetry very close to this in the solid phase. It is interesting that the solid-state structure preserved this.

Due to the steric effect found using tbip in **12**, it was suspected that some additional bulk (from the aluminum alkyl) might break the typical dimer arrangement into monomers. Thus, we employed TEA rather than TMA to produce heteroleptic aluminum compounds of the type (ip)$AlEt_2$. Three ethyl derivatives were synthesized, with the other ethyl derivatives seeming to require much more stringent reaction conditions. The investigation of these ethyl compounds is ongoing. No crystals of sufficient quality for structural determination of the tbip derivative **15** were collected, but the sec-butyl (sbip) derivative **14** was determined to be a dimer by crystallographic analysis (Figure

3.3.4). The similarity of the melting points of **14** and **15** as well as NMR data strongly suggested that **13** and **15** are dimers as well.

Table 3.3.5: Yields and Melting Points of Aluminum Diethyl Iminopyrrolidinate Complexes

Compound	R	Yield (%)	Melting Point (°C)
13	Iso-propyl (ipip)	70	120 – 124
14	Sec-butyl (sbip)	71	60 – 63
15	Tert-butyl (tbip)	34	63 – 64

Compound **14** was also crystallised in a *$P2_1/n$* space group with the inversion centre at the molecular centre, and the aluminum centres in distorted tetrahedral bonding environments (Tables 3.3.6 and 3.3.7). The crystal structure was very similar to compound **7** in that it was highly symmetrical and the 8 membered ring was in a chair like conformation. The sp^2 carbon was very close to planar with the sum of angles at 359.9°. The bond lengths of the nitrogens to C8 (N1 and N2) were again short (1.325 Å and 1.331 Å, respectively), indicating that they were involved in the π-system. These nitrogen centres were also very close to planar with the sum of angles at 357.3° and 355.9°, respectively. The N1-Al-N2 angle was found to be 112.7°, and the ligand angle was very similar to complex **7** at 122.7°.

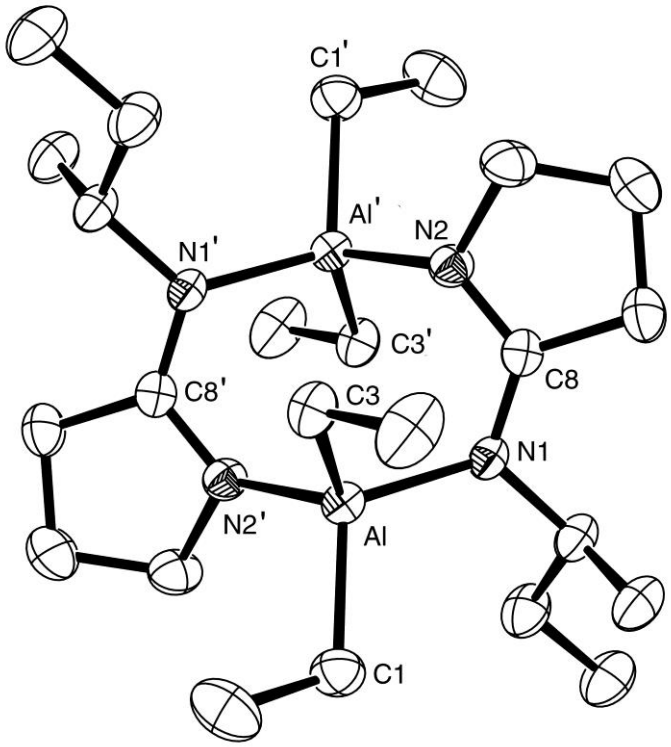

Figure 3.3.5: Molecular structure of **14**. Thermal ellipsoids are drawn at 50% probability, and the H atoms have been omitted for clarity.

Table 3.3.6: Metrical Data for sbipAlEt$_2$ (14)

Selected Bond Lengths (Å)			
Al – N(1)	1.9457(14)	Al – C(3)	1.9816(17)
Al – N(2')	1.9276(14)	N(1) – C(8)	1.325(2)
Al – C(1)	1.9920(18)	N(2) – C(8)	1.331(2)
Selected Bond Angles (°)			
C(1)–Al–C(3)	109.12(8)	C(8)–N(1)–Al	117.01(10)
N(1)–Al–N(2')	112.72(6)	Al'–N(2)–C(8)	126.05(11)
N(1)–C(8)–N(2)	122.73(14)		

Table 3.3.7: X-ray Data for 7, 12, and 14			
	7	**12**	**14**
empirical formula	$C_9H_{19}N_2Al$	$C_{20}H_{42}N_4Al_2$	$C_{24}H_{50}N_4Al_2$
Fw	182.24	392.54	448.64
cryst syst	monoclinic	monoclinic	monoclinic
space group	P2 (1)/n	P2 (1)/n	P2 (1)/n
a (Å)	8.101(8)	8.168(4)	8.1090(14)
b (Å)	8.521(9)	17.903(8)	19.526(4)
c (Å)	15.814(16)	16.396(7)	8.7766(16)
α (deg)	90	90	90
β (deg)	93.618(15)	104.42(2)	101.582(3)
γ (deg)	90	90	90
V ($Å^3$)	1089.4(19)	2322.1(18)	1361.4(4)
Z	4	4	2
D_c (kg/L)	1.111	1.123	1.094
μ (mm^{-1})	0.141	0.137	0.124
T(^oC)	120(2)	120(2)	170(2)

The trend in the melting point of the ligands **1** – **6** was reflected in the melting points of the heteroleptic aluminum complexes, as seen in Table 3.3.1. For instance, **8** (npipAlMe_2) had a lower melting point than **7** (ipipAlMe_2), reflecting the above-mentioned trend for the ligands. Again, as the length of the alkyl chain increases by one carbon, the melting point decreases. Increasing the branching from n-butyl to t-butyl increased the melting point with the exception of the stereocenter and asymmetry of the sec-butyl complex **11**.

The thermogravimetric analysis of the heteroleptic aluminum complexes (Figure 3.3.6), was conducted to evaluate the characteristics of these compounds as potential vapour-phase precursors for MOCVD or ALD. Although there is no real need for additional aluminum-containing precursors for the deposition of traditional aluminum target films (Al_2O_3 and AlN), this does lend credibility to these ligands, potentially in other applications where guanidinates and amidinates are employed.

Compounds **7** to **11** have similar features in the TG. Each complex has two main features: the first feature is a 5 – 8% weight loss, which can be attributed to a slow thermal degradation of the compound.

The second feature in the TGs signified the volatility of compounds **7** to **11**, all of which had residual masses of <12%. This is acceptable for a vapour deposition precursor, and likely represents non-volatile decomposition products formed through the slow thermal degradation that occurred during the collection of these data.

Compound **12** has a different TG, insomuch as the onset of volatility is significantly lower. This might be attributed to the steric bulk of the tert-butyl groups, which may prevent intermolecular N-Al interactions. It also has a higher temperature feature, starting at about 150°C. Here, the sublimation appeared to occur at a lower temperature than decomposition. Thus, ligand **6** holds significant promise for vapour deposition applications.

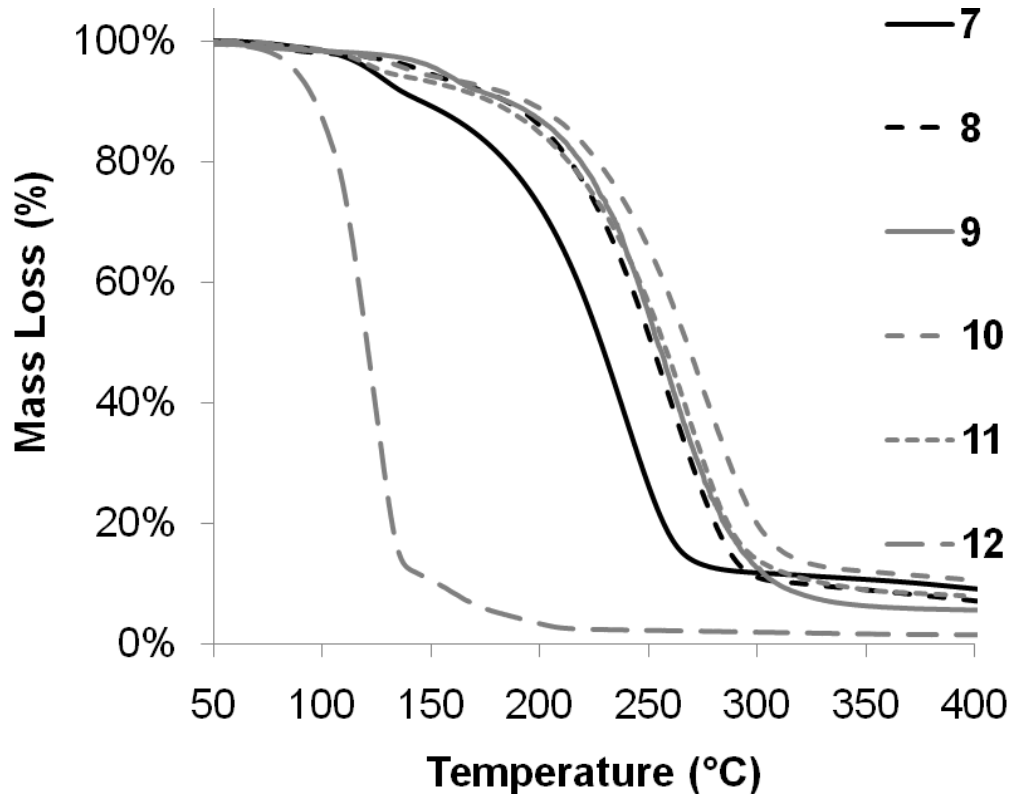

Figure 3.3.6: Thermogravimetric analysis of heteroleptic aluminum complexes **7** – **12**.

Sealed NMR tube thermolysis experiments were conducted for the methyl derivatives (**7** – **12**). These were dissolved in 0.35(± 6)mL 1% v/v TMS in C_6D_6 or 5% v/v TMS in C_6D_6 solution in thick-walled NMR tubes, under inert atmosphere. The tubes were frozen and sealed under vacuum. They were placed in a furnace at 78°C and the decomposition of the dimethyl peak was monitored relative to the peak from the TMS. This thermolysis experiment showed that the ring feature of the ligands designed to prevent CDI deinsertion was effective. No CDI peaks were seen in the ^{1}H NMR spectra and the ligands appear to have stayed intact.

Each compound had a first order decomposition with respect to the loss of the aluminum dimethyl signal in the ^{1}H NMR (Figure 3.3.7). This was significantly different from aluminum guanidinates, where the decomposition never followed simple kinetics because of competing thermolysis pathways. Now that CDI deinsertion has been eliminated through ligand design, the decomposition follows straightforward first-order decomposition.

From this study it was clear that the nbip (**9**) complex was the most stable, with the iso-butyl (**10**) and tert-butyl (**12**) complexes also showing significant half-lives (Table 3.3.8). Note that the error on k and half-lives was approximately +/- 0.02 $days^{-1}$ and +/-0.2 days, respectively.

Table 3.3.8: Rate Constant and Half-life for the First-order Decomposition of Compounds 7 – 12 at 78°C

Compound	R	k (day^{-1})	Half-life (day)
7	Iso-propyl (ipip)	0.38	1.8
8	N-propyl (npip)	0.12	5.6
9	N-butyl (nbip)	0.03	24.8
10	Iso-butyl (ibip)	0.08	9.0
11	Sec-butyl (sbip)	0.33	2.1
12	Tert-butyl (tbip)	0.07	10.3

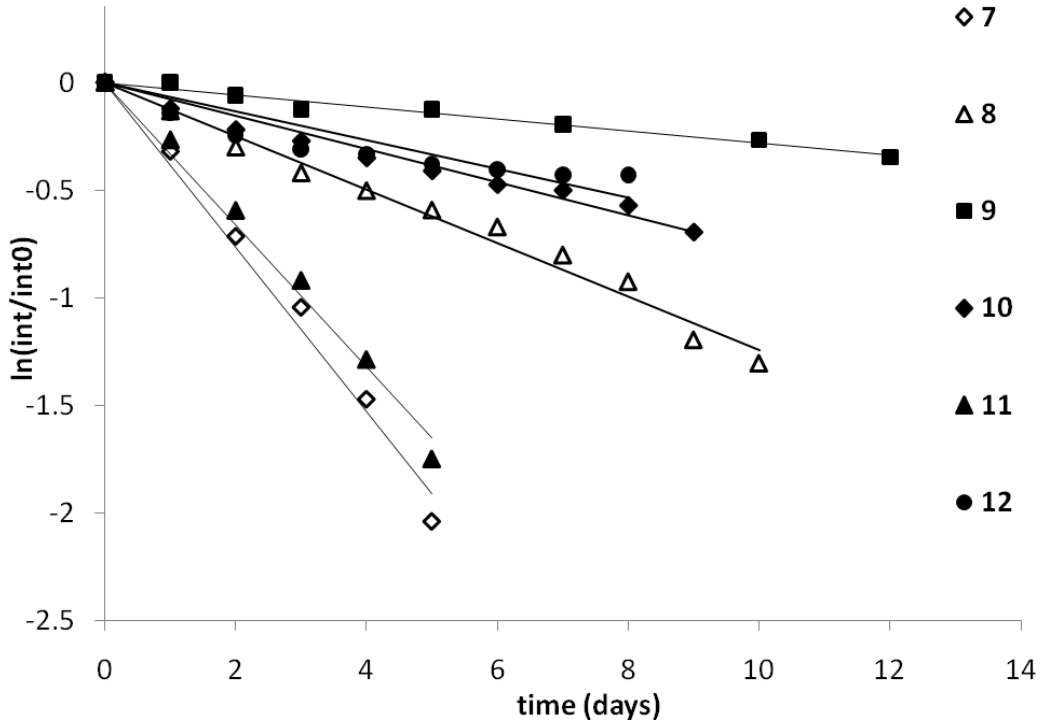

Figure 3.3.7: First order decomposition of compounds **7** – **12** at 78°C.

The loss of the methyl signal in the spectra of **7** – **12** was concomitant with the production of a new set of peaks associated with two iminopyrrolidinate ligand environments and no precipitation from solution was seen. This thermolysis is most obvious in the decomposition of **7**, which will be used as an example to explain the suspected thermal rearrangement.

After 12 days at 78°C, the ^{1}H NMR signals associated with compound **7** had completely disappeared, and a new ligand environment was seen in the ^{1}H NMR with signals at δ 3.39, 3.24 (m, 4H, N(C*H*$_2$CH$_2$CH$_2$C)), 3.00 (m, 4H, N(C*H*$_2$CH$_2$CH$_3$)), 1.96 (m, 4H, N(CH$_2$CH$_2$C*H*$_2$C)), 1.42 (m, 4H, N(CH$_2$C*H*$_2$CH$_2$C)), 1.29 (br. m, 4H, N(CH$_2$C*H*$_2$CH$_2$C)), 0.82 (double tr., 6H, N(CH$_2$CH$_2$C*H*$_3$)), 0.15, -0.16, -1.01 (s, 6H, Al(CH$_3$)$_2$). These peaks show a pattern that is most easily

described as the formation of a dimerised ligand, suggesting that the dimer molecule might have produced monomers during thermolysis, developing a new bonding mode to the aluminum species through two resonance structures. (Figure 3.3.8). This unusual reactivity is the subject of an ongoing mechanistic investigation.

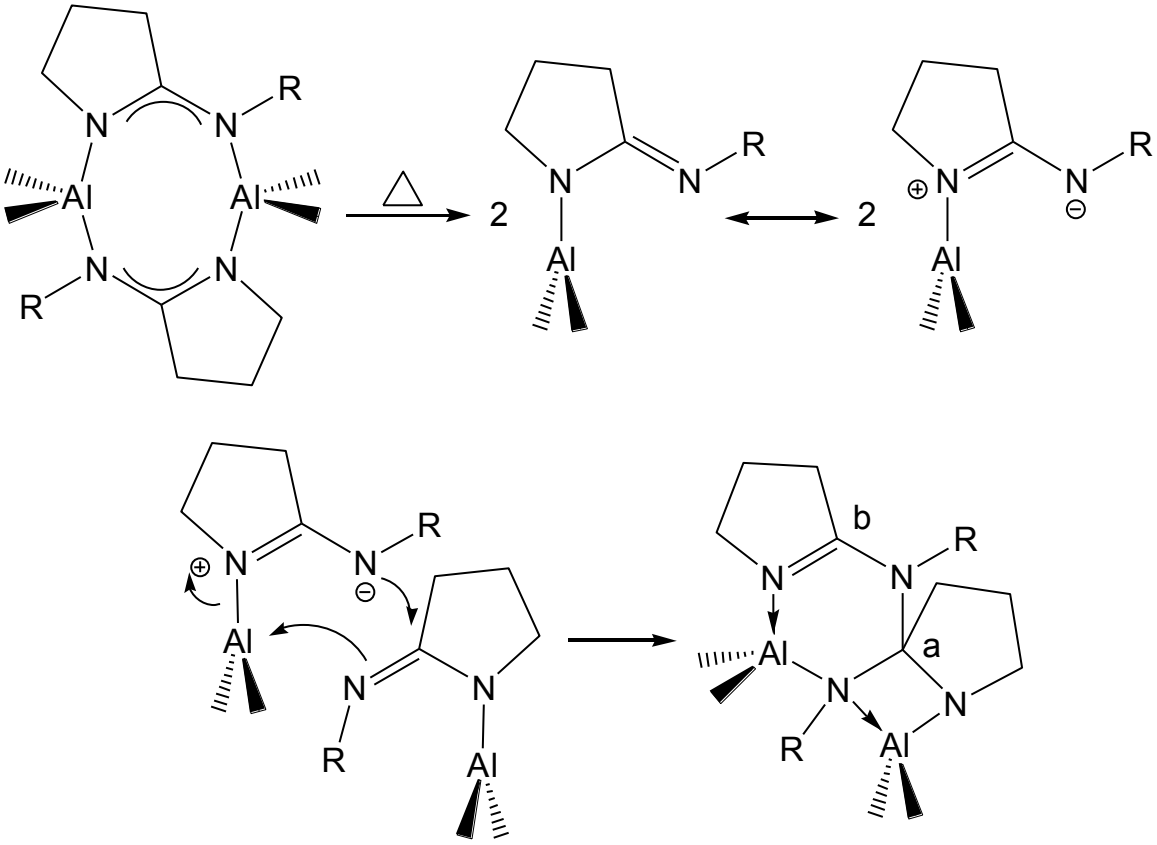

Figure 3.3.8: Isomerization followed by dimerisation of the ligand.

In the ^{1}H NMR of thermolised **8**, the sextet of the R-group protons showed a chemical shift of 1.42ppm from 1.39ppm in **8**. Also, the quintet of the ring protons at 1.29ppm, shifted from 1.32ppm in **8**. The resolution of these peaks also supports proposed new ligand environments.

As previously mentioned, in the thermolysis study, the methyl signal of **8** at -0.34ppm diminishes over time, and is replaced with a singlet at -0.16ppm, seen in the spectrum of thermolised **8**. DEPT-135 analysis confirmed the presence of a new methyl peak, as would be expected when the dimerization occurs.

Significantly, the ^{13}C NMR spectrum showed the development of quaternary carbons at 179.7 and 179.5ppm (labeled “a” and “b” in Figure 3.3.8). Neither peak represents the original quaternary carbon of **8**, which are very similar to one another. Chemical shift coupled with DEPT-135 analysis showed these carbon peaks to represent quaternary carbons.

3.4 Experimental

General Considerations: All manipulations were performed in a nitrogen-filled drybox unless otherwise specified. The chemicals: TMA, TEA, 2-pyrrolidinone, isopropyl amine, n-propyl amine, n-butyl amine, iso-butyl amine, sec-butyl amine, tert-butyl amine, and phosphorous pentoxide were purchased from Aldrich Chemical Company and used as received. All solvents used were reagent grade and purified from an MBraun Solvent Purifier System. Nuclear Magnetic Resonance experiments were performed on 300MHz Avance 3 and 400MHz Bruker AMX spectrometers. Mass spectra were obtained using the electron impact method on a VG ZAB-2HF triple-focusing spectrometer. Guelph Chemical Laboratories performed combustion analysis. Thermogravimetric analysis was performed on a TA Instruments Q50 apparatus located in an MBraun Labmaster

130 Dry box under a nitrogen atmosphere. Differential Scanning Calorimetry was performed on a TA Instruments Q10 apparatus.

Isopropyl-iminopyrrolidine (ipip, **1**): A mixture of 2-pyrrolidinone (3.0g, 35.2mmol) and isopropyl amine (4.4g, 70.5mmol) was prepared in the dry box, capped and brought out of the dry box. This mixture was added 1mL at a time through a reflux condenser to a 100mL round bottom flask that contained neat phosphorous pentoxide (5.0g, 35.2mmol). As the pyrrolidinone mixture reached the reaction flask, vapour began to rise up the reflux condenser. The reaction mixture was heated over 1 h to 220°C and then refluxed with stirring for 2 h at this temperature in a sand bath. The reaction was cooled to room temperature and it became a hard glassy substance. Distilled water (40mL) was added to the flask and the compound dissolved with the aid of a heat gun. Using a Pasteur pipette aqueous NaOH solution (6M, 50mL) was added until a pH of 11 was obtained. The aqueous phase was extracted with washes of diethyl ether (3 x 70mL). Volatiles were removed under reduced pressure to afford a brown solid (3.6g, 28.5mmol, 81%). The brown solid sublimed at 60°C under reduced pressure to afford needle-like white precipitate (3.3g, 26mmol, 78%). mp (99 – 100°C). ^{1}H NMR (300 MHz, C_6D_6): δ 4.09 (m, 1H, NC*H*$(CH_3)_2$), 3.79 (t, 2H, N(C*H*$_2$)), 1.90 (t, 2H, NC(C*H*$_2$)), 1.61 (quintet, 2H, N(CH_2)(C*H*$_2$)), 1.02 (d, 6H, NCH(C*H*$_3$)$_2$). ^{13}C NMR (300 MHz, C_6D_6): δ 57.56 (N(*C*H_2)), 43.75 (N*C*H$(CH_3)_2$), 33.03 (NC(*C*H_2)), 23.59 (N(CH_2)(*C*H_2)), 22.90 (NCH(*C*H_3)$_2$). Mass spectral data (EI, *m/z*) (rel. intensity, %): 126.1 (76.4, M^+). Combustion analysis; found (calculated), C: 66.43 (66.62), H: 10.92 (11.18), N: 22.44 (22.20).

N-propyl-iminopyrrolidine (npip**, 2**): The same reaction procedure as **(1)** was used substituting the previous amine with n-propyl amine (4.4g, 70.5mmol). Volatiles were removed under reduced pressure to afford an off-white solid (3.8g, 30.1mmol, 85%). The solid sublimed at 60°C under reduced pressure to afford needle-like white precipitate (3.2g, 25.4mmol, 72%). mp (72 – 74°C). ^{1}H NMR (300 MHz, C_6D_6): δ 3.78 (t, 2H, NC*H*$_2$CH$_2$CH$_2$C), 3.44 (s, 1H, NCN*H*), 3.22 (t, 2H, CH$_3$CH$_2$C*H*$_2$N), 1.92 (t, 2H, NCH$_2$CH$_2$C*H*$_2$C), 1.63 (quintet, 2H, NCH$_2$C*H*$_2$CH$_2$C), 1.41 (sextet, 2H, CH$_3$C*H*$_2$CH$_2$N), 0.77 (t, 3H, C*H*$_3$CH$_2$CH$_2$N). ^{13}C NMR (300 MHz, C_6D_6): δ 165.49 (N*C*N), 56.56 (N*C*H$_2$CH$_2$CH$_2$C), 44.88 (CH$_3$CH$_2$*C*H$_2$N), 32.51 (NCH$_2$CH$_2$*C*H$_2$C), 23.55 (CH$_3$*C*H$_2$CH$_2$N), 23.13 (NCH$_2$*C*H$_2$CH$_2$C), 11.44 (*C*H$_3$CH$_2$CH$_2$N). Mass spectral data (EI, *m/z*) (rel. intensity, %): 126.1 (92.0, M$^+$). Combustion analysis; found (calculated), C: 66.39 (66.62), H: 11.36 (11.18), N: 22.25 (22.20).

N-butyl-iminopyrrolidine (nbip**, 3**): The same reaction procedure as **(1)** was used substituting the previous amine with n-butyl amine (5.156g, 70.5mmol). Volatiles were removed under reduced pressure to afford an off white solid (4.3g, 30.6mmol, 87%). The solid sublimed at 60°C under reduced pressure to afford needle like white precipitate (3.71g, 26.4mmol, 75%). mp (55 – 56°C). ^{1}H NMR (300 MHz, C_6D_6): δ 3.78 (t, 2H, NC*H*$_2$CH$_2$CH$_2$C), 3.28 (t, 2H, C*H*$_2$CH$_2$CH$_2$CH$_3$), 1.95 (t, 2H, NCH$_2$CH$_2$C*H*$_2$C), 1.63 (quin, 2H, NCH$_2$C*H*$_2$CH$_2$C), 1.40 (quin, 2H, CH$_2$C*H*$_2$CH$_2$CH$_3$), 1.22 (sext, 2H, CH$_2$CH$_2$C*H*$_2$CH$_3$), 0.83 (t, 3H, C*H*$_3$). ^{13}C NMR (400 MHz, C_6D_6): δ 165.04 (N*C*N), 57.08 (N*C*H$_2$CH$_2$CH$_2$CH$_3$), 42.62 (N*C*H$_2$CH$_2$CH$_2$C), 32.55 (NCH$_2$CH$_2$*C*H$_2$C), 32.06 (NCH$_2$*C*H$_2$CH$_2$CH$_3$), 23.64

($NCH_2CH_2CH_2C$), 20.18 ($NCH_2CH_2CH_2CH_3$), 13.74 ($NCH_2CH_2CH_2CH_3$). Mass spectral data (EI, *m/z*) (rel. intensity, %): 140.1 (39.3, M^+). Combustion analysis; found (calculated), C: 68.52 (68.52), H: 11.45 (11.50), N: 20.22 (19.98).

Iso-butyl-iminopyrrolidine (ibip**, 4**): The same reaction procedure as **(1)** was used substituting the previous amine with iso-butyl amine (7.741g, 105.8mmol), phosphorous pentoxide (10.316g, 72.7mmol), and 2-pyrrolidone (6.081g, 71.5mmol). Volatiles were removed under reduced pressure to afford an off-white solid. The solid sublimed at 60°C under reduced pressure to afford needle-like white precipitate (6.0g, 42.8mmol, 60%). mp (102 – 103°C). ^{1}H NMR (300 MHz, C_6D_6): δ 3.78 (t, 2H, $NCH_2CH_2CH_2C$), 3.09 (d, 2H, $CH_2CH(CH_3)_2$), 1.91 (t, 2H, $NCH_2CH_2CH_2C$), 1.77 (m, 1H, $CH_2CH(CH_3)_2$), 1.62 (quin, 2H, $NCH_2CH_2CH_2C$), 0.80 (d, 6H, $CH_2CH(CH_3)_2$). ^{13}C NMR (400 MHz, C_6D_6): δ 164.95 (NCN), 57.21 ($NCH_2CH_2CH_2C$), 50.58 ($NCH_2CH(CH_3)_2$), 32.52 ($NCH_2CH_2CH_2C$), 28.33 ($NCH_2CH(CH_3)_2$), 23.63 ($NCH_2CH_2CH_2C$), 20.08 ($NCH_2CH(CH_3)_2$). Mass spectral data (EI, *m/z*) (rel. intensity, %): 140.1 (43.4, M^+). Combustion analysis; found (calculated), C: 68.90 (68.52), H: 11.21 (11.50), N: 19.77 (19.98).

Sec-butyl-iminopyrrolidine, (sbip**, 5**): The same reaction procedure as **(1)** was used substituting the previous amine with sec-butyl amine (7.743g, 105.9mmol), phosphorous pentoxide (10.345g, 72.8mmol), and 2-pyrrolidone (6.070g, 71.3mmol). Volatiles were removed under reduced pressure to afford an off-white solid. The solid sublimed at 65°C under reduced pressure to afford needle like white precipitate (6.767g, 48.2mmol, 68%). mp (100°C). ^{1}H NMR (300 MHz, C_6D_6): δ 3.94 (m, 1H, $CH(CH_3)(CH_2CH_3)$), 3.79 (t, 2H, $NCH_2CH_2CH_2C$), 1.92 (t,

2H, $NCH_2CH_2CH_2C$), 1.61 (quin, 2H, $NCH_2CH_2CH_2C$), 1.31 (m, 2H, $CH(CH_3)(CH_2CH_3)$), 1.02 (d, 3H, $CH(CH_3)(CH_2CH_3)$), 0.80 (t, 3H, $CH(CH_3)(CH_2CH_3)$). ^{13}C NMR (400 MHz, C_6D_6): δ 164.10 (N*C*N), 57.36 ($NCH_2CH_2CH_2C$), 49.12 ($NCH(CH_3)(CH_2CH_3)$), 32.86 ($NCH_2CH_2CH_2C$), 29.65 ($NCH(CH_3)(CH_2CH_3)$, 23.49 ($NCH_2CH_2CH_2C$), 20.35 ($NCH(CH_3)(CH_2CH_3)$, 10.28 ($NCH(CH_3)(CH_2CH_3)$. Mass spectral data (EI, *m/z*) (rel. intensity, %): 140.1 (41.2, M^+). Combustion analysis; found (calculated), C: 68.51 (68.52), H: 11.21 (11.50), N: 20.30 (19.98).

Tert-butyl-iminopyrrolidine (tbip, **6**): The same reaction procedure as **(1)** was used substituting the previous amine with tert-butyl amine (8.083g, 110.6mmol), phosphorous pentoxide (5.284g, 37.2mmol), and 2-pyrrolidone (3.062g, 40.0mmol). Volatiles were removed under reduced pressure to afford an off-white solid. The solid sublimed at 65°C under reduced pressure to afford needle-like white precipitate (1.5g, 10.7mmol, 30%). mp (108 – 110°C). ^1H NMR (300 MHz, C_6D_6): δ 3.82 (t, 2H, $NCH_2CH_2CH_2C$), 1.89 (t, 2H, $NCH_2CH_2CH_2C$), 1.54 (quin, 2H, $NCH_2CH_2CH_2C$), 1.38 (s, 9H, $C(CH_3)_3$). ^{13}C NMR (400 MHz, C_6D_6): δ 177.91 ($C(CH_3)_3$), 163.01 (N*C*N), 58.30 ($NCH_2CH_2CH_2C$), 34.44 ($NCH_2CH_2CH_2C$), 28.75 ($C(CH_3)_3$), 22.76 ($NCH_2CH_2CH_2C$). Mass spectral data (EI, *m/z*) (rel. intensity, %): 140.1 (59.3, M^+). Combustion analysis; found (calculated), C: 68.24 (68.52), H: 11.58 (11.50), N: 20.41 (19.98).

Dimethyl aluminum isopropyl-iminopyrrolidinate (ipipAlMe_2, **7**): Isopropyl iminopyrrolidine (1.58g, 12.5mmol) was suspended in approximately 40mL of hexanes and slowly added to a solution of TMA (6.3mL, 12.5mmol, 2M) in about

80mL of hexanes. The reaction was allowed to proceed for 18 h at room temperature. Volatiles were removed under reduced pressure to afford a colourless solid. The solid was dissolved in about 8mL of diethyl ether and allowed to recrystallize at -30°C. Colourless cubic crystals were collected (1.7g, 9.3mmol, 75%). mp (87 – 91°C). ^{1}H NMR (300 MHz, C_6D_6): δ 3.28 (m, 1H, NC*H*$(CH_3)_2$), 3.22 (t, 2H, N(C*H*$_2$)), 1.94 (t, 2H, NC(C*H*$_2$)), 1.35 (quintet, 2H, N(CH_2)(C*H*$_2$)), 1.16 (d, 6H, NCH(C*H*$_3$)$_2$), -0.37 (s, 6H, Al(C*H*$_3$)$_2$). ^{13}C NMR (300 MHz, C_6D_6): δ 179.03 (N-*C*-N), 50.84 (N*C*H(CH_3)$_2$), 49.81 (N(*C*H$_2$)), 31.45 (NC(*C*H$_2$)), 23.33 (NCH(*C*H$_3$)$_2$), 22.52 (N(CH_2)(*C*H$_2$)). Mass spectral data (EI, *m/z*) (rel. intensity, %): 349.2 (4.4, $(M\text{-}Me)^+$). Combustion analysis; found (calculated), C: 58.90 (59.31), H: 10.76 (10.51), N: 15.70 (15.37).

Dimethyl aluminum n-propyl-iminopyrrolidinate (npipAlMe_2, **8**): The same reaction procedure as **(7)** was used substituting the previous iminopyrrolidine with n-propyl-iminopyrrolidine (1.5g, 11.8mmol). Volatiles were removed under reduced pressure to afford a colourless precipitate. The solid was dissolved in about 5mL of diethyl ether and allowed to recrystallize at -30°C. Colourless cubic crystals were collected (1.7g, 9.3mmol, 79%). mp (79 – 83°C). ^{1}H NMR (300 MHz, C_6D_6): δ 3.27 (t, 2H, NC*H*$_2$$CH_2CH_2C$), 3.05 (t, 2H, CH_3CH_2C*H*$_2$N), 1.92 (t, 2H, NCH_2CH_2C*H*$_2$C), 1.39 (sextet, 2H, CH_3C*H*$_2$$CH_2$N), 1.32 (quintet, 2H, NCH_2C*H*$_2$$CH_2$C), 0.77 (t, 3H, C*H*$_3$$CH_2CH_2$N), -0.34 (s, 6H, Al(C*H*$_3$)$_2$). ^{13}C NMR (300 MHz, C_6D_6): δ 181.85 (N*C*N), 51.04 (CH_3CH_2*C*H$_2$N), 51.00 (N*C*H$_2$$CH_2CH_2$C), 31.07 ($NCH_2CH_2$*C*H$_2$C), 25.83 ($CH_3$*C*H$_2$$CH_2$N), 21.83 ($NCH_2$*C*H$_2$$CH_2$C), 11.46 (*C*$H_3CH_2CH_2$N). Mass spectral data (EI, *m/z*) (rel. intensity, %): 349.2 (38.5, (M-

Me)$^+$). Combustion analysis; found (calculated), C: 59.15 (59.31), H: 10.80 (10.51), N: 15.33 (15.37).

Dimethyl aluminum n-butyl-iminopyrrolidinate (nbipAlMe$_2$, **9**): The same reaction procedure as **(7)** was used substituting the previous iminopyrrolidine with n-butyl-iminopyrrolidine (1.86g, 13.3mmol). Volatiles were removed under reduced pressure to afford a colourless precipitate. The solid was dissolved in about 8mL of hexanes and allowed to recrystallize at -30°C. Colourless crystals were collected (2.141g, 10.9mmol, 84%). mp (68 – 70°C). ^{1}H NMR (300 MHz, C_6D_6): δ 3.29 (t, 2H, NC*H*$_2$CH$_2$CH$_2$C), 3.11 (t, 2H, C*H*$_2$CH$_2$CH$_2$CH$_3$), 1.96 (t, 2H, NCH$_2$CH$_2$C*H*$_2$C), 1.37, 1.22 (m, 6H, NCH$_2$C*H*$_2$CH$_2$C, CH$_2$C*H*$_2$C*H*$_2$CH$_3$), 0.86 (t, 3H, CH$_2$CH$_2$CH$_2$C*H*$_3$), -0.34 (s, 6H, Al(C*H*$_3$)$_2$). ^{13}C NMR (400 MHz, C_6D_6): δ 181.85 (N*C*N), 51.01 (N*C*H$_2$CH$_2$CH$_2$C), 48.96 (N*C*H$_2$CH$_2$CH$_2$CH$_3$), 34.86 ((NCH$_2$*C*H$_2$CH$_2$CH$_3$), 31.08 (NCH$_2$CH$_2$*C*H$_2$C), 21.79 (NCH$_2$*C*H$_2$CH$_2$C), 20.36 (NCH$_2$CH$_2$*C*H$_2$CH$_3$), 13.77 (NCH$_2$CH$_2$CH$_2$*C*H$_3$). Mass spectral data (EI, *m/z*) (rel. intensity, %): 377.3 (83.8, (M-Me)$^+$). Combustion analysis; found (calculated) 61.30 (61.20), H: 12.36 (10.78), N: 14.13 (14.27).

Dimethyl aluminum iso-butyl-iminopyrrolidinate (ibipAlMe$_2$, **10**): The same reaction procedure as **(7)** was used substituting the previous iminopyrrolidine with iso-butyl-iminopyrrolidine (1.595g, 11.4mmol). Volatiles were removed under reduced pressure to afford a pale pink precipitate. The solid was dissolved in about 15mL of diethyl ether and allowed to recrystallize at -30°C. Colourless crystals were collected (2.020g, 10.3mmol, 91%). mp (111 – 113°C). ^{1}H NMR (300 MHz, C_6D_6): δ 3.29 (t, 2H, NC*H*$_2$CH$_2$CH$_2$C), 2.95 (d, 2H, C*H*$_2$CH(CH$_3$)$_2$),

1.96 (t, 2H, $NCH_2CH_2CH_2C$), 1.58 (m, 1H, $CH_2CH(CH_3)_2$), 1.34 (quin, 2H, $NCH_2CH_2CH_2C$), 0.83 (d, 6H, $CH_2CH(CH_3)_2$), -0.34 (s, 6H, $Al(CH_3)_2$). ^{13}C NMR (400 MHz, C_6D_6): δ 182.14 (NCN), 57.34 ($NCH_2CH(CH_3)_2$), 51.21 ($NCH_2CH_2CH_2C$), 31.67 ($NCH_2CH_2CH_2C$), 31.44 ($NCH_2CH(CH_3)_2$), 21.82 ($NCH_2CH_2CH_2C$), 20.34 ($NCH_2CH(CH_3)_2$). Mass spectral data (EI, *m/z*) (rel. intensity, %): 377.3 (36.3, $(M\text{-}Me)^+$). Combustion analysis; found (calculated), C: 61.04 (61.20), H: 11.06 (10.78), N: 14.55 (14.27).

Dimethyl aluminum sec-butyl-iminopyrrolidinate (sbipAlMe$_2$, **11**): The same reaction procedure as **(7)** was used substituting the previous iminopyrrolidine with sec-butyl-iminopyrrolidine (1.029g, 7.3mmol). Volatiles were removed under reduced pressure to afford a yellow precipitate. The solid was dissolved in about 15mL of diethyl ether and allowed to recrystallize at -30°C. Colourless crystals were collected (1.3g, 6.62mmol, 90%). mp (62 – 65°C). ^1H NMR (300 MHz, C_6D_6): δ 3.21 (t, 2H, $NCH_2CH_2CH_2C$), 3.01 (m, 1H, $CH(CH_3)(CH_2CH_3)$), 1.94 (dt, 2H, $NCH_2CH_2CH_2C$), 1.57 (m, 2H, $CH(CH_3)(CH_2CH_3)$), 1.37 (quin, 2H, $NCH_2CH_2CH_2C$), 1.16 (d, 3H, $CH(CH_3)(CH_2CH_3)$), 0.82 (t, 3H, $CH(CH_3)(CH_2CH_3)$), -0.38 (s, 6H, $Al(CH_3)_2$). ^{13}C NMR (400 MHz, C_6D_6): δ 177.09 (NCN), 57.61 ($NCH(CH_3)(CH_2CH_3)$), 49.37 ($NCH_2CH_2CH_2C$), 30.91 ($NCH_2CH_2CH_2C$), 30.65 ($NCH(CH_3)(CH_2CH_3)$), 22.59 ($NCH_2CH_2CH_2C$) 20.65 ($NCH(CH_3)(CH_2CH_3)$), 11.64 ($NCH(CH_3)(CH_2CH_3)$). Mass spectral data (EI, *m/z*) (rel. intensity, %): 377.3 (1.2, $(M\text{-}Me)^+$). Combustion analysis; found (calculated), C: 60.92 (61.20), H: 11.03 (10.78), N: 13.88 (14.27).

Dimethyl aluminum tert-butyl-iminopyrrolidinate (tbipAlMe$_2$, **12**): Using a 3mL syringe, TMA (1.4mL, 2.0M) was added quickly into a 100mL Schlenk flask containing hexanes (30mL) and a magnetic stir bar. The flask was sealed using a rubber septum and removed from the drybox. It was secured onto a Schlenk line and kept under N_2 atmosphere. Tbip ligand was dissolved in a 50:50 mixture of hexanes and ether in the drybox. It was delivered to the flask on the Schelnk line, through the rubber septum in two 10mL syringes, one at a time. The addition was drop-wise and with constant stirring at -10°C in a methanol ice bath. Upon total addition of the dissolved tbip to the Schlenk flask, the rubber septum was replaced with a glass stopper and the reaction proceeded. After 2 h, the flask was removed from the ice bath the reaction was allowed to proceed for an additional 2 h until room temperature was reached. After complete evacuation of the solvent, the reaction vessel was remitted to the drybox. The solid was dissolved in about 7mL of diethyl ether and allowed to recrystallize at -30°C. Colourless crystals were collected (52% yield). mp (116 – 118°C). ^{1}H NMR (300 MHz, C_6D_6): δ 3.00 (t, 2H, NC*H*$_2$CH$_2$CH$_2$C), 1.85 (t, 2H, NCH$_2$CH$_2$C*H*$_2$C), 1.43 (quin, 2H, NCH$_2$C*H*$_2$CH$_2$C), 1.06 (s, 9H, C(C*H*$_3$)$_3$), -0.22 (s, 6H, Al(C*H*$_3$)$_2$). ^{13}C NMR (400 MHz, C_6D_6): δ 181.94 (N*C*N), 180.75 (N*C*(CH$_3$)$_3$), 46.66 (N*C*H$_2$CH$_2$CH$_2$C), 30.95 (NC(*C*H$_3$)$_3$), 28.87 (NCH$_2$CH$_2$*C*H$_2$C), 22.70 (NCH$_2$*C*H$_2$CH$_2$C). Mass spectral data (EI, *m/z*) (rel. intensity, %): 377.3 (36.3, (M-Me)$^+$). Combustion analysis; found (calculated), C: 61.04 (61.20), H: 11.06 (10.78), N: 14.55 (14.27).

Diethyl aluminum isopropyl-iminopyrrolidinate (ipipAlEt$_2$, **13**): The same reaction procedure as **(7)** was used substituting the previous aluminum complex with TEA 15.85mL, 15.8mmol, 1M). The solution was clear and colourless. Volatiles were removed under reduced pressure to afford a colourless solid. The solid was dissolved in about 14mL of diethyl ether and allowed to recrystallize at -30°C. Colourless cubic crystals were collected (1.9g, 10.4mmol, 66%). mp (120 – 124°C). ^{1}H NMR (300 MHz, C_6D_6): δ 3.35 (m, 1H, NC*H*$(CH_3)_2$), 3.25 (t, 2H, N(C*H*$_2$)), 2.06 (t, 2H, NC(C*H*$_2$)), 1.42 (quintet, 2H, N(CH_2)(C*H*$_2$)), 1.30 (t, 6H, Al$(CH_2CH_3)_2$), 1.15 (d, 6H, NCH(C*H*$_3)_2$), 0.24 (q, 4H, Al(C*H*$_2CH_3)_2$). ^{13}C NMR (300 MHz, C_6D_6): δ 181.53 (N-*C*-N), 50.08 (N(*C*H$_2$)), 49.80 (N*C*H$(CH_3)_2$), 32.47 (NC(*C*H$_2$)), 23.14 (NCH(*C*H$_3)_2$), 22.41 (N(CH_2)(*C*H$_2$)), 10.22 (Al$(CH_2CH_3)_2$), 1.23 (Al(*C*H$_2CH_3)_2$). Combustion analysis; found (calculated), C: 63.11 (62.82), H: 11.28 (11.02), N: 13.72 (13.32).

Diethyl aluminum sec-butyl-iminopyrrolidinate (sbipAlEt$_2$, **14**): The same reaction procedure as **(7)** was used substituting the previous aluminum complex with TEA (9mL, 9.0mmol, 1M) and the previous iminopyrrolidine with sec-butyl-iminopyrrolidine (1.263g, 9.0mmol). The solution was clear and colourless. Volatiles were removed under reduced pressure to afford a pale yellow, transparent liquid. The liquid was dissolved in diethyl ether and allowed to crystallize at -30°C to afford a colourless crystalline solid (1.43g, 6.4mmol, 71%). ^{1}H NMR (300 MHz, C_6D_6): δ 3.27 (t, 2H, NC*H*$_2$CH$_2$CH$_2$C), 3.09 (m, 1H, C*H*$(CH_3)(CH_2CH_3)$), 2.06 (t, 2H, NCH$_2$CH$_2$C*H*$_2$C), 1.59 (m, 2H, NCH$_2$C*H*$_2$CH$_2$C), 1.41 (m, 2H, CH(CH_3)(C*H*$_2CH_3)$), 1.32 (t, 6H, Al$(CH_2CH_3)_2$), 1.15 (d, 3H,

$CH(CH_3)(CH_2C\mathit{H_3})$), 0.24 (quad, 4H, $Al(C\mathit{H_2}CH_3)_2$). ^{13}C NMR (300 MHz, C_6D_6): δ 180.86 (N*C*N), 56.46 ($NCH(CH_3)(CH_2CH_3)$), 50.06 ($NCH_2CH_2CH_2C$), 32.57 ($NCH_2CH_2CH_2C$), 30.60 ($NCH(CH_3)(CH_2CH_3)$), 22.51 ($NCH_2CH_2CH_2C$) 20.23 ($NCH(CH_3)(CH_2CH_3)$), 12.03 ($NCH(CH_3)(CH_2CH_3)$), 10.37 ($Al(CH_2CH_3)_2$), 1.23 ($Al(CH_2CH_3)_2$). Combustion analysis; found (calculated). C: 64.35 (64.25), H: 11.25 (11.23), N: 12.32 (12.49).

Diethyl aluminum tert-butyl-iminopyrrolidinate ($tbipAlEt_2$, **15**): The same reaction procedure as **(7)** was used substituting the previous aluminum complex with TEA (1.4mL, 1.4mmol, 1M) and the previous iminopyrrolidine with tert-butyl-iminopyrrolidine (0.196g, 1.4mmol). The solution was clear and colourless. Volatiles were removed under reduced pressure to afford a pale yellow, transparent liquid. The liquid was dissolved in diethyl ether and allowed to crystallize at -30°C to afford a colourless crystalline solid (0.106g, 0.47mmol, 34%). mp (63 – 64°C). ^1H NMR (300 MHz, C_6D_6): δ 3.02 (t, 2H, $NC\mathit{H_2}CH_2CH_2C$), 1.88 (t, 2H, $NCH_2CH_2C\mathit{H_2}C$), 1.46 (m, 2H, $NCH_2C\mathit{H_2}CH_2C$), 1.38 (t, 6H, $Al(CH_2C\mathit{H_3})_2$), 1.06 (s, 9H, $C(C\mathit{H_3})_3$), 0.38 (quad, 4H, $Al(C\mathit{H_2}CH_3)_2$). ^{13}C NMR (300 MHz, C_6D_6): δ 180.89 (N*C*N), 179.44 ($NC(CH_3)_3$), 47.09 ($NCH_2CH_2CH_2C$), 30.91 ($NC(CH_3)_3$), 28.74 ($NCH_2CH_2CH_2C$), 25.14 ($NCH_2CH_2CH_2C$), 9.28 ($Al(CH_2CH_3)_2$). Combustion analysis; found (calculated), C: 64.10 (64.25), H: 11.38 (11.23), N: 12.34 (12.49).

Crystallography: A suitable single crystal was selected and mounted on a glass fiber using Paratone oil, flash-cooled to 150K. Data were collected on a Brüker-AXS APEX CCD diffractometer with graphite-monochromated Mo-Kα radiation

(λ= 0.71073 Å). Unit cell parameters were obtained from 60 data frames, 0.3°ω, from three different sections of the Ewald sphere. The systematic absences in the data and the unit cell parameters were uniquely consistent with the reported space group. The data set was treated with SADABS absorption corrections based on redundant multiscan data.[51] All non-hydrogen atoms were refined with anisotropic displacement parameters. All hydrogen atoms were treated as idealized contributions. Structure factors are contained in the SHELXTL 6.12 program library.

3.5 Conclusions

Six iminopyrrolidine ligands were synthesized with excellent yields and purified by sublimation. They were reacted with TMA and TEA at room temperature with good yields resulting in nine novel heteroleptic aluminum complexes. The ligands demonstrated a melting point trend within the propyl and butyl groups that was mimicked in the aluminum iminopyrrolidinate species. The iminopyrrolidinate ligands proved to be more thermally stable than their guanidinate and amidinate counterparts as they did not undergo CDI deinsertion and their decomposition was shown to be simpler by means of a ^{1}H NMR thermolysis study. The formation of a dimer of the ligand was seen after the aluminum species were heated for several days at elevated temperatures.

Chapter 4 – Trends in Copper Precursor Development for CVD and ALD Applications

Please see preface, page 4, for more details and full article citation. Author contributions listed below are paraphrased from signed Letters of Permission to reprint this material.

Agnieszka Kurek is first second of this review paper. Her contributions to this published work included literature research, some writing, editing and figure composition. Please see preface, page 4, for more details and full article citation.

Peter Gordon contributed literature research, writing, and editing.

Sean Barry contributed literature research, interpretation, writing, and editing.

4.1 Abstract

The continued dominance of copper in microelectronic manufacturing is due in part to the techniques that have kept pace with the relentless trend towards smaller feature sizes. Pure and defect-free copper features can be created at these and smaller scales using gas phase deposition methods such as chemical vapor deposition (CVD) and atomic layer deposition (ALD). Here we review the deposition processes and in particular surface chemistry for depositing copper metal by CVD and ALD. A summary of known processes is given, and new trends in copper film deposition research are discussed. As well, process parameters and properties of copper films deposited from precursors using key ligand systems such as aminoalkoxides, amidinates, guanidinates, betadiketonates and betaketoiminates are presented. Surface chemistry is examined from the point of view of the similarities of CVD and ALD, considering precursors that can be used in both types of processes. This serves to highlight trends in decomposition mechanisms and illuminates some interesting similarities in process temperature and other parameters.

Copper metal is an important conductive material, particularly in microelectronics. It was introduced by IBM in 1997, and has been used as the interconnect material in computer microprocessors since that time.[52] The electrochemical deposition of copper metal for this application took nearly ten years to develop, and continued effort in electroplating has extended the utility of this method to today.[53] Copper metal has a bulk resistivity of 1.7241μΩ·cm[54], which should be used as a reference for reported resistivities in this review.

According to the international road map of semiconductors[55], manufacturing is reaching the point whereby electrochemical deposition will no longer be sufficient to achieve the nanoscale needed to meet technical requirements. The challenge of producing pure, defect-free, conductive metal films at nearly atomic levels is expected to rely on vapor deposition methods driven by chemical reactions from gas phase precursors to deposit copper at a given surface. With vapor phase deposition techniques, it is the surface chemistry of the precursors that to a large extent determines many of the characteristics of the film. The main principle behind vapor deposition is the chemical reaction of a precursor compound to form a surface species after it is introduced into the reaction chamber where the substrate is located. The process is usually thermally activated but other methods (e.g., plasma) can be implemented. If the precursor is designed appropriately, once the surface reaction occurs, volatile fragments of the compound will be released and can be removed from the reactor by a purge of inert gas or vacuum purge. Ligand and unwanted components can be removed cleanly before they have a chance to be incorporated into the growing material. Among vapor deposition methods, chemical vapor deposition (CVD) and atomic layer deposition (ALD) have emerged as highly scalable, versatile and easily modified techniques that are widely researched and continually developed for improved copper metal deposition.

A wide variety of surface reactions can result from interaction of a precursor with a surface, but the production of a metal film relies on the chemisorbed precursor undergoing reduction of its copper center, and eliminating

its byproducts. Thus, the surface chemistry of successful CVD and ALD processes likely share many characteristics. Herein, we review the deposition processes and in particular surface chemistry of copper metal deposition by these two techniques.

4.2 Introduction

Chemical Vapor Deposition (CVD) vs. Atomic Layer Deposition (ALD)

CVD is a broad term that covers both the continual deposition methods that adopt this name, as well as the more specific, layer-by-layer growth method of ALD. CVD involves the entrainment of gaseous precursor compounds into a reaction chamber where a change in the thermodynamic state induces the conversion of the precursor to a target film at a surface (Figure 4.2.1a). This change can be caused by any systematic variable, and commonly is controlled thermally. There are several excellent introductions to CVD that highlight the significant development in computational and kinetic modeling, as well as the engineering of CVD reactors.[56] In a typical CVD process, the precursor reacts with a secondary gas to produce a target film. This reaction needs to be surface-activated, i.e., the reaction to form the target film must occur at a surface to promote dense, cohesive films and avoid loose layers of flakes. This process is continual, since the target film is always forming at some specific rate, and the uniformity of the film is highly dependent on the mass transport of the precursor to the film as well as the rate constant of the uptake of the precursor by the surface. Although CVD is generally thought of as a precursor compound reacting

with a secondary gas at a surface to form a target film, it is not uncommon for the precursor to undergo this deposition without a secondary gas. Indeed, copper compounds are easily reduced to metal, and so many copper precursors will act as “single source precursors”, with the ligand system acting as the reducing agent. Such precursors delicately balance thermal stability in the gas phase with chemical reactivity at the surface (vide infra).

The idea of continual growth at the surface is what separates common CVD from ALD (Figure 4.2.1b).[57] In ALD, the precursor is chosen or designed in such a way that it will chemisorb to the growth surface, but it will not convert to the target film. The introduction of a second precursor (the “secondary reactant gas” of CVD) will subsequently chemically react to convert this stable monolayer to the target film. Again, this can be thought of as a thermally activated process at the surface, but any number of techniques or conditions can invoke this change. For example, in both CVD and ALD, plasma is commonly used in this role to allow lower temperature processes. Typical metal deposition occurs at above 200°C, while plasma assistance can lower this practically to room temperature by activating the reaction chemically, rather than thermally. In ALD, the growth rate is determined by cycles, commonly consisting of a pulse of each precursor, separated by purges with inert gases, vacuum, or both to remove reaction by-products and excess precursor molecules (Figure 4.2.1b). Film thicknesses after one cycle vary significantly, but typically are below one Ångström for metals. This is an indication that growth does not occur in ideal monolayer-by-monlayer fashion, but by *sub-monolayer* growth. This means that

the surface sites are not completely saturated each time a new precursor is introduced. Puurunnen reported an excellent summary of known ALD processes, and many copper processes are reported there.[7]

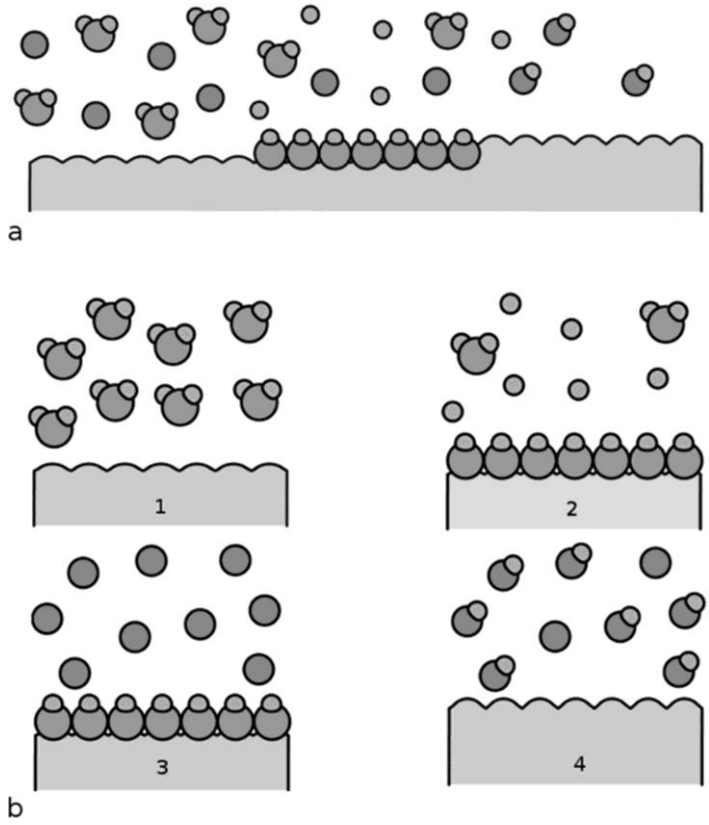

Figure 4.2.1: CVD (a) is a continual deposition where all reactants are introduced simultaneously, and reaction ideally occurs at the surface by chemisorbed species. ALD (b) occurs in several steps, ideally by 1) chemisorption of the precursor, 2) purge of the byproducts, 3) reaction with a second precursor or "secondary reactant gas," and 4) another purge of byproducts.

The stability of the chemisorbed precursor monolayer is the defining factor for growth rate per cycle (GPC). Deposition processes can range from strictly ALD growth where the monolayer is completely, thermodynamically stable to processes that exhibit ALD growth at shorter cycle times, but show a continual growth CVD component at higher cycle times. This indicates the decomposition

or auto-conversion of the chemisorbed monolayer. This nuance, where the cycle time can differentiate whether a process is ALD or CVD, is a common concept in copper metal deposition. It is notable that having a “CVD” component of growth in a step-wise ALD process does not render it useless, and such processes can show excellent conformality of the deposited film.

Copper Reduction

Copper metal is easily reduced compared to many metals on the periodic table, a discussion that was central to an excellent review of transition metal precursors by Winter.[58] As discussed by this review, copper (in its +2 state) has a standard reduction potential of 0.3419V, making it the most easily reduced metal in the first row of the transition metals. In contrast, Ti^{2+} has a standard reduction potential of –1.630V. Although this means that copper films are easily produced, it also means that copper precursors need to be designed with stability in mind so that the compounds only undergo self-reduction in desired conditions. It is even easier to reduce Cu(I) to copper metal, which has a standard reduction potential of 0.521V. Therefore, the thermal stability of copper precursors is an often-discussed characteristic when designing precursor compounds.

Typically, hydrogen gas is used as a reductant for copper precursors. Dihydrogen can homolytically dissociate to hydrogen adatoms on clean metal surfaces, greatly increasing the rate of reduction. However, there have recently been some interesting attempts to use a variety of other reducing agents, and novel techniques to do so. Table 4.2.1 outlines many key CVD and ALD processes for copper deposition, and gives several typical process parameters

and conditions. This table highlights the predominance of dihydrogen gas as a reducing agent.

It should be noted that the substrate influences the effectiveness of hydrogen gas. Metal substrates can help cleave dihydrogen into hydrogen adatoms, which are at a higher chemical potential and so more effective at reduction. This has made noble metals a favored substrate for copper deposition.[59] However, these metals (with some exceptions) are less useful for microelectronics applications. Ruthenium is a notable exception: copper has a low (i.e., preferable) wetting angle when deposited on a ruthenium substrate. This allows for better conductivity due to less crystallization and better connectivity of the copper.

Table 4.2.1: Summary of Copper Metal Deposition Processes by Chemical Vapor Deposition or Atomic Layer Deposition

Process	Precursor A/ T (°C)	Precursor B/ T (°C)	Process T (°C)	Substrate	Growth rate	Resistivity (μΩ·cm) / thickness (μm)	Year Reported [Ref]
CVD	CuCl/ 300-350	H_2	350 – 500	Si, SiO_2	8 Å/min	3.3/1.5	1992 [60]
ALD	CuCl/ 350	H_2	360 – 410	Ta	0.8 – 1.25 Å/cycle	NR	1997 [61]
ALD	CuCl/ 340	H_2O, H_2	375 – 475	Al_2O_3, SiO_2	1.6 Å/cycle	NR	2004 [62]
ALD	CuCl/ 390	Zn/ 435	500 (Cu:Zn alloy)	Al_2O_3	1 – 5.5 Å/cycle	NR	1997 [63]
CVD	$Cu(dmae)_2$/ 90-98		200 – 210	$SrTiO_3$	NR	200/ NR	1993 [64]
CVD	$Cu(OCR_2CH_2NHR')_2$; R: CH_3, CF_3; R': tBu, $CH_2CH_3OCH_3$/ 155		250	Si	19.0 Å/min	3.44/0.15	2001 [65]
CVD	$Cu(dmap)_2$/ 55		230 – 350	Si	13 – 30 Å/min	2.19/1.8	2003 [66]
CVD	$Cu(deap)_2$/ 65		230 – 350	Si	50 – 75 Å/min	2.16/4.0	2003 [66]
ALD	$Cu(dmamb)_2$ / 70	H_2 plasma	150	Ta	0.65 Å/cycle	5.2/0.010	2011 [67]
ALD	$Cu(dmamb)_2$ / NR	HCO_2H + N_2H_4	120	Si	0.5 Å/cycle	9.6 – 16.4/ 0.040 – 0.050	2011 [68]
ALD	$Cu(dmap)_2$/ NR	BH_3NMe_2	130-160	Ru	0.13 Å/cycle	68/0.017, 1250/0.025	2014 [69]
ALD	$Cu(dmap)_2$/ NR	HCO_2H + BH_3NMe_2	135-165	Pt, Pd	0.20 Å/cycle	Pt: 15.6 – 21.4/0.020; Pd: 6.4 – 21.4/0.020	2014 [69]
ALD	$[Cu(sBu\text{-}amd)]_2$/ 100	H_2	185	Al_2O_3, SiO_2	1.9 Å/cycle	NR	2006 [70]
ALD	$[Cu(sBu\text{-}amd)]_2$/ 100	H_2	185	Si_3N_4	1.50 Å/cycle	NR	2006 [70]
ALD	$[Cu(sBu\text{-}amd)]_2$/ 100	H_2	185	WN	0.54 Å/cycle	NR	2006 [70]
ALD	$[Cu(sBu\text{-}amd)]_2$/ 100	H_2	185	Ru	0.11 Å/cycle	NR	2006 [70]
ALD	$[Cu(sBu\text{-}amd)]_2$/ 100	H_2	185	Co	0.40 Å/cycle	NR	2006 [70]
ALD	$[Cu(sBu\text{-}amd)]_2$/ 100	H_2	185	Cu	~0.5 Å/cycle	NR	2006 [70]
ALD	$[Cu(sBu\text{-}amd)]_2$/ 100	H_2	185	Glass	NR	2.9/0.080	2006 [70]
CVD	$[Cu(iPr\text{-}amd)]_2$/ 95	H_2	200 – 300	Steel, Si, Si/SiO_2	2.0 – 4.2 Å/min	4/0.270	2009 [71]
ALD	$[Cu(iPr\text{-}amd)]_2$/ 95		280	Si, Glassy C, Glass	0.5 Å/cycle	NR	2003 [43]
CVD	$[Cu(iPr\text{-}guan)]_2$/ 125		200	Optical fiber	18 Å/min	NR	2011 [73]

CVD	$Cu(acac)_2$, $Cu(tfac)_2$, $Cu(hfac)_2$/ 60 – 200	H_2	225 – 390	NR	4.0 Å/min	3 – 6/NR	1991 – 2002 [74-76]
CVD	$Cu(hfac)_2 \cdot H_2O$/ 30 – 60	H_2	250 – 350	NR	10 Å/min	1.9 – 2.8/NR	2002 [75]
CVD	Cu(bdk)*L/ 33 – 77		30 – 400	NR	NR	NR	2002 [75]
CVD	Cu(hfac)(vtms)/ 50		75 – 420	NR	>140 Å/min	NR	1991 [77]
ALD	$Cu(acac)_2$/ 130	H_2	250	Al, Ti, Glass	NR	NR	2002 [78]
ALD	$Cu(acac)_2$/ 125	H_2 plasma	140	Si, Glass	0.18 Å/cycle	15/0.025	2007 [79,80]
ALD	$Cu(thd)_2$/ 120		150 – 350	Pt/Pd	0.36 Å/cycle	8/0.060	1998-2007 [81-83]
ALD	$Cu(thd)_2$/ 120		235	Ti/Pt	0.7 Å/cycle	NR	2009 [84]
ALD	$Cu(thd)_2$/ 123.5	H_2 plasma	180	Si, Pt	0.12 Å/cycle	NR	2005 [85]
ALD	$Cu(hfac)_2 \cdot H_2O$/ 75	CH_2O, MeOH, EtOH	300	Si	NR	1.78/0.120	2000 [86]
ALD	$Cu(hfac)_2$/ 60	H_2 + cat. pyridine	RT – 100	TiN	0.185 Å/cycle	19/0.015	2010 [87]
ALD	Cu(hfac) (vtmos)/ 60	H_2 plasma	200 – 300	TiN	0.5 Å/cycle	2/0.040	2009 [88]
ALD	$Cu(dmap)_2$/ 70	$ZnEt_2$	100 – 120	Si	0.2 Å/cycle	2.78/0.050	2009 [89]
ALD	$Cu(pyrim)_2$/ 120	$ZnEt_2$	130	SiO_2, Ta, Ru	NR	89/0.120	2010 [90]
ALD	Cu(dki)(vtms)	SiH_2Et_2	120	NR	NR	NR	2006 [91]
ALD	Cu(nhc) (hmds)/ 90	H_2 plasma	225	Si	0.2 Å/cycle	11.23/0.035	2013 [92]
CVD	$[CuN(tms)_2]_4$/ 200	H_2, UV light	200	Si, Glass	NR	NR	1998 [93]

*"NR" herein means that the film thicknesses were not reported with the resistivity data.

4.3 Results and Discussion

Diethyl Zinc

An interesting reducing agent was introduced in 2009 from Hanyang University (Figure 4.3.1).[88] Using $[Cu(dmap)]_2$ volatilized at 70°C (where "dmap" is dimethylamino-2-propoxide), copper metal films were deposited between 100°C – 120°C using diethylzinc as the second reactant. Here, the copper and zinc undergo a ligand exchange, and the resulting copper alkyl surface species spontaneously reductively eliminates to produce copper metal. The film was found to incorporate significant zinc, oxygen, and carbon impurities above a deposition temperature of 120°C. Diethylzinc was used in a similar manner with $Cu(pyrim)_2$ (where "pyrim" is N-ethyl-2-pyrrolylaldiminate) at a evaporation temperature of 120°C, and a deposition temperature of 130°C.[89] In this study, SiO_2, Ta, and Ru substrates were used, and relatively smooth copper (120nm) with a resistivity of 89μΩ·cm was found on SiO_2 as well as Ta. There was significant incorporation of impurities, with the metallic film containing roughly 10% zinc and significant oxygen contamination in the bulk film. In both cases where diethyl zinc was used, reductive elimination of butane from diethyl zinc is the likely contributor to the metallic impurity, as discussed at length in a computational model from Tyndall.[93]

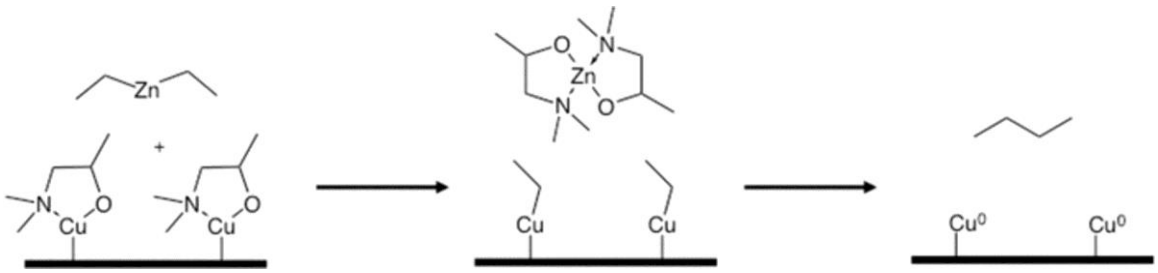

Figure 4.3.1: The reduction of copper "dmap" by dielthyl zinc through ligand exchange and subsequent reductive elimination.

It should be noted that the computational study modeled all species as gas phase molecules, while this review uses surface species notation for consistency with subsequent chemical equations and schemes. In general, the elimination of ZnX_2 where X is an anionic ligand, is more likely when ZnX_2 is a more volatile species, and this was modeled in two steps in this paper (Figure 4.3.2). It is interesting to note that this study finds that the reduction of the surface species is more likely if the surface species is Cu(I). If the precursor is Cu(II) and remains in this oxidation state when chemisorbed, then a "double" ligand exchange will result in a surface bound $CuEt_2$ species, which will not easily reductively eliminate to form metallic copper. However, two chemisorbed CuEt moieties will undergo reductive elimination to form metallic copper and butane:

$$\|\text{-}CuEt_2 \rightarrow \text{unfavorable reaction}$$

$$2\ \|\text{-}CuEt \rightarrow 2\ \|\text{-}Cu^0 + C_4H_{10(g)}$$

The reductive elimination of two ethyl groups to form butane is always more favorable than any other reductive elimination with respect to the ligands modeled in this study. It was also noticeable that the “pyrim” ligands had a greater propensity to drive the deposition of zinc metal through favorable disproportionation from a chemisorbed Zn(I) species:

$$2\ \|\text{-}ZnX \rightarrow \|\text{-}Zn^0 + ZnX_{2(g)}$$

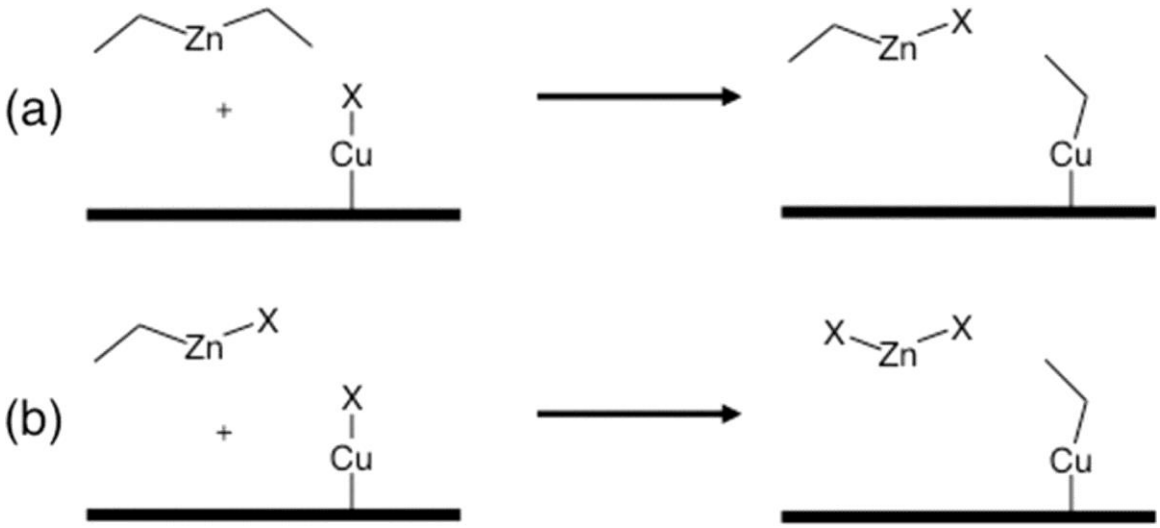

Figure 4.3.2: Diethylzinc likely undergoes ligand exchange with copper surface species in a two-step reaction, generating an intermediate mixed ligand zinc compound before fully eliminating $ZnCl_2$.

Iodine Catalyzed Copper Deposition

In 2000, Seoul National University published a study showing that copper-adsorbed iodine could greatly enhance copper metal deposition.[94] Using Cu(hfac)(vtms), where hfac is hexafluoroacetylacetonate and vtms is vinyltrimethylsilane, copper was shown to deposit with an enhanced rate of 155Å/min at 150°C without hydrogen. Ethyl iodide was used to catalyze the reaction, and was found to cover the surface with about 1/10th of a monolayer. The enhancement was so successful that copper even deposited with a growth rate of 25Å/min at 50°C, well below the common deposition temperature required for such a system. Interestingly, the authors found that the hfac desorbed from the surface as a dimer. This discovery led to a flurry of research with a variety of precursors,[95,96] surface treatments,[97,98] and substrates.[99] Molecular iodine has also been used to catalyze copper metal deposition.[100] The substrate was pretreated with I_2 plasma and using the same copper precursor, growth was enhanced from 10 – 20Å/min at 170°C.

Catalyzed surface growth also showed the excellent characteristic of allowing bottom-up pore filling by deposited copper metal.[101] This was shown be the result of a concentration of the iodine adatoms at the bottom of the feature compared to on the side-walls, thus accelerating bottom-up growth.[102]

Solution Testing of Second Precursors

One burgeoning method of testing secondary “co-reagents” for copper metal deposition is solution testing. An excellent example of this was published in 2010 from a collaboration between McMaster University and Intel.[89] In this

publication, $AlMe_3$, BEt_3, and $ZnEt_2$ were tested with a variety of Cu(II) precursors to ascertain whether copper metal would precipitate from the solution reaction. These three compounds were of interest because they are all hard and borderline Lewis acids and can alkylate copper reagents easily. Also, their tolerance for oxygen and nitrogen-containing ligands make them more chemically compatible as reducing agents. The copper compounds used in this study can be found in Figure 4.3.3, which has structural diagrams for all precursors mentioned in this review.

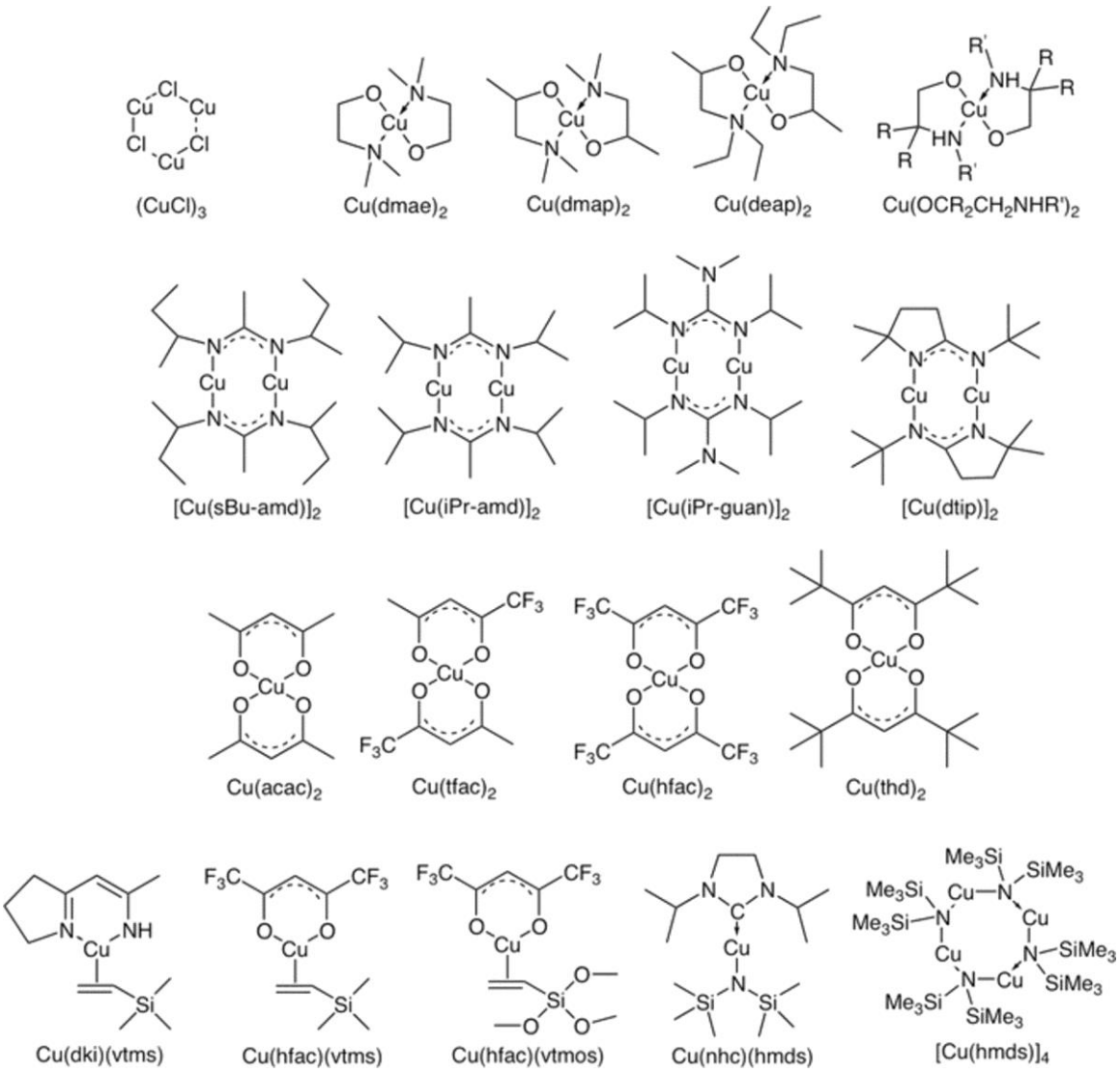

Figure 4.3.3: Chemical structures for the variety of copper precursors discussed in this review.

The reactions were carried out in a 1:1 or 2:1 stoichiometric mixture of coreagent:copper precursor in toluene. These were kept for 24 hours at each of the following temperatures: 25°C, 50°C, 75°C, 100°C, and 120°C while being observed for copper metal formation. Any suspected copper metal depositions were verified by PXRD and XPS. Successful reactions were repeated in the

presence of a variety of substrates to produce copper films for imaging by SEM. In general, $AlMe_3$ and $ZnEt_2$ were found to be better co-reactants than BEt_3. Interestingly, in the case of copper(II) N-isopropyl-2-salicylaldiminate, the precipitate was seen to be a mixture of amorphous zinc and brass (β-CuZn).

This straightforward technique can be quite easily adapted to any synthetic lab, and is likely in our opinion to become a common screening technique for precursors and co-reactants alike. Caution should be taken in its employment, however: it is possible that solvent polarity could influence both the stability and reactivity of given precursor/co-reactant pairs by either stabilizing the copper compound through coordinative bonding, or enhancing reactivity by solvent cage or similar effects. This is certainly an excellent technique to use in conjunction with other reactivity studies to enhance reactivity studies prior to committing to full-scale deposition process development.

Comparison of CVD and ALD of Copper

In a field as diverse and widely researched as copper deposition, it is impossible to assess the chemistry and deposition characteristics of every process. However, since the driving force behind the deposition of copper metal by CVD and ALD is undeniably the surface chemistry that is involved, it is useful to investigate this aspect more deeply. It is particularly instructive to compare CVD and ALD processes that exist for the same chemical precursors. This will highlight the necessary surface chemistry involved in physisorption, chemisorption, and chemical reaction to produce a target film.

From the outset, Cu(II) (d9) centers and Cu(I) (d10) centers need to be differentiated. Cu(II) prefers a square planar arrangement due to its favorable electronic configuration, but distortion from this geometry by steric effects is not uncommon.[93] This generally means that CuX_2 species undergo cleavage upon chemisorption to a surface. In general, one can consider the growing film to consist of copper metal atoms, and so one ligand can adsorb to the surface, while the copper center in the precursor becomes a ligand-supported surface adatom.[93] A simple formalism is the comproportionation to Cu(I) of the surface Cu(0) state and the Cu(II) precursor state:

$$Cu^{2+}X_{2(g)} + \Vdash Cu^{0} \rightarrow 2 \Vdash Cu^{+}X$$

This is in contrast to Cu(I). The d10 electronic configuration favours a linear geometry, and by only supporting one anionic ligand, the precursor compound needs to satisfy its coordination sphere somehow. Thus, there are generally two forms of volatile Cu(I) compounds. If there is an attendant coordinative ligand, the linear geometry will be satisfied through a coordinative bond to form CuX·L (where L is a neutral ligand). In this case, loss of the coordinative ligand is the most straightforward method of chemisorption:

$$Cu^{+}X{\cdot}L_{(g)} + \Vdash \rightarrow \Vdash Cu^{+}X + L_{(g)}$$

In the absence of a coordinating ligand, the compound can oligomerize, typically to a dimer (i.e. $[CuX]_2$). Thus chemisorption can be a simple matter of cleaving the dimer into surface-supported monomers:

$$[CuX]_{2(g)} + 2 \Vdash \rightarrow 2 \Vdash Cu^{+}X$$

It should be noted that CVD and ALD growth rates cannot necessarily be compared directly: CVD growth rates here are reported in Å/min, while ALD growth rates are reported in Å/cycle. The cycle time for different ALD processes can vary significantly, and are not necessarily optimized to be the shortest possible cycle. Thus, while ALD growth rates are typically lower than CVD growth rates, the reader should keep in mind that CVD is reported with respect to time, and ALD is reported with respect to "cycle".

Copper Chloride

Cuprous chloride (CuCl) was first reported as a deposition precursor in 1992 at Uppsala University.[60] Here, CVD deposition of copper metal was seen at temperatures between 350 – 500°C in a quartz tube furnace with a growth rate of 5 – 8Å/min. This precursor required an extremely high temperature to volatilize (300 – 350°C), limiting its practicality. However, conductive films of copper metal (1.5μm, with a resistivity of 3.3μΩ·cm) were deposited on silica using hydrogen as a reducing agent. There was no further exploration of the surface chemistry of this deposition in this paper, but the authors suppose the copper is formed by elimination of hydrogen chloride gas.

The Uppsala group were also able to undertake deposition of copper metal by ALD using copper(I) chloride.[61] In this case, the copper metal was deposited on tantalum metal foils, using an evaporation temperature of 350°C and a deposition temperature range of 360 – 410°C. The growth per cycle (GPC)

was limited at 0.8Å/cycle with respect to a pulse of CuCl of less than 10s, but increased at higher deposition times. This led the authors to speculate that the chloride disproportionated to Cu(0) and Cu(II) at higher temperatures. The growth rate of deposited copper increased as the hydrogen pulse increased, from 0.8 –1.25Å/cycle at 410°C. This also showed a 1/T relationship with respect to the deposition temperature. The authors speculate that the surface maintains a saturated copper chloride monolayer, but the hydrogen inserts itself into the adsorbed CuCl bond, and eliminates HCl while leaving a surface hydride (Figure 4.3.4). We speculate that this surface hydride can react with the next pulse of CuCl and eliminate HCl to form a clean copper metal surface. This surface is then able to uptake another equivalent of CuCl, thus showing the increased deposition rate.

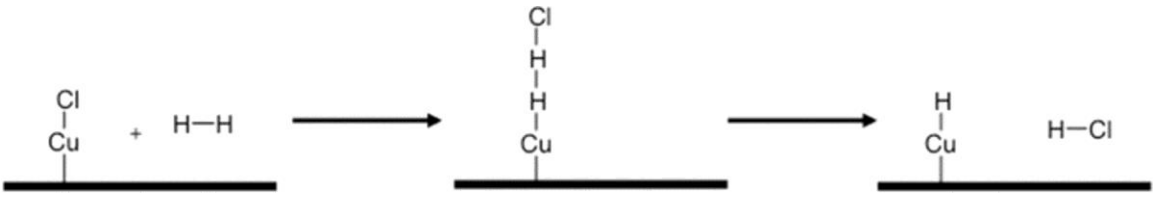

Figure 4.3.4: Insertion of dihydrogen gas into the existing copper-chloride bond of a copper chloride surface species, with subsequent elimination of hydrogen chloride gas.

ALD of copper metal on alumina-covered silica using CuCl was reported in 1997 from the University of Helsinki.[63] In this case, the CuCl was held at 390°C and zinc vapor was used as the reducing agent, held at 435°C. Cu:Zn alloy films were deposited on alumina at 500°C. Saturation was not observed in this case, and very large growth rates (1.0–5.5Å/cycle) were seen. The authors speculate

that self-limiting growth initially occurs, but once copper was formed, the zinc metal started to dissolve in it, as well as acting as a reducing agent. This report showed no reaction using hydrogen for a reducing agent at these temperatures.

The Uppsala group also deposited copper metal by ALD using hydrogen and water as second precursors in the deposition process.[62] Here, the evaporation temperature was 340°C, and deposition occurred on alumina and silica between 375 – 475°C, which was very similar conditions to the deposition on tantalum. Herein, the authors added water to the deposition process between the copper and hydrogen pulses (i.e., $CuCl/H_2O/H_2$). As reported, this generally had the effect of significantly increasing the rate of copper metal deposition on alumina, but not on silica. The authors reported that this enhancement was caused by the formation of an intermediate copper oxide:

$$2\,\|\text{-CuCl} + H_2O_{(g)} \rightarrow \|\text{-}Cu_2O + 2\,HCl_{(g)}$$

With alumina as the substrate, water greatly improved the growth rate, giving a saturation “plateau” at 1.6Å/cycle, but the “saturation curve” with respect to hydrogen pulse length showed a significantly decreasing plateau. We suggest that this could be desorption of the copper species. In the process without water (i.e., $CuCl/H_2$), this report showed some growth, which contrasts the results from the Helsinki group. There was no saturation curve for this process, and the difference in deposition might be attributed to reactor design.

The effect of water in the growth process on silica did not change the deposition rate. The rate topped out at 1.1Å/cycle, again showing a decreasing plateau. With both substrates, saturation started somewhere between pulse

times of 10s and 15s, showing a slower reaction to hydrogen than when tantalum was used as the substrate. This supports the idea that the metal substrate participates in fixing hydrogen for the reaction.

Our interpretation of using CuCl as a precursor is that the CVD process is limited by the kinetics of decomposition of cuprous chloride by hydrogen, a process estimated to have an activation energy of 80kJ/mol.[61] With CuCl pulse lengths lower than 10s, the kinetic stability of the adsorbed layer is sufficient to allow layer-by-layer ALD growth, but CVD deposition occurs at higher exposures. Thus, kinetic stability of the monolayer can be sufficient to allow an ALD process to occur. The process is obviously quite sensitive to substrate, and this highlights an important aspect of CVD and ALD: the process is often thought to mainly concern the gaseous precursors, but the substrate plays an obvious and important role in defining the thermodynamics of the system, and thus is an important chemical partner in the process.

There are no known CVD or ALD processes using copper(II) chloride. Presumably this is due to the low volatility of this species compared to the Cu(I) compound.

Aminoalkoxides

Copper aminoalkoxides were first used for copper metal deposition in 1993 at Virginia Tech.[64] Deposition of copper metal occurred on strontium titanate using copper(II) dimethylaminoethoxide. Pure copper films were deposited between 200 – 210°C with the precursor held between 90 – 98°C. The resulting films had resistivities on the order of 200μΩ·cm with low levels of

oxygen, and no detectable levels of nitrogen. Careful thermal decomposition studies showed metal formation by the oxidation of a ligand through β-hydrogen abstraction, coupled with reductive elimination to produce one equivalent of the parent ligand (Figure 4.3.5). It should be noted that the mechanism given in Figure 4.3.5 incorporates the chemisorption modeled at the Tyndall Institute,[93] and so is our reinterpretation of the similar, original mechanism. In this model, the simple chemisorption of a variety of Cu(II) precursors (CuX_2) was shown to undergo a ligand shift of one ligand to a growing copper surface while the chemisorbed species maintained its second ligand:

$$\|\text{-Cu} + CuX_{2(g)} \rightarrow 2\ \|\text{-CuX}$$

This comproportionation has been discussed earlier in this review, but seems to be a common surface adsorption mechanism.

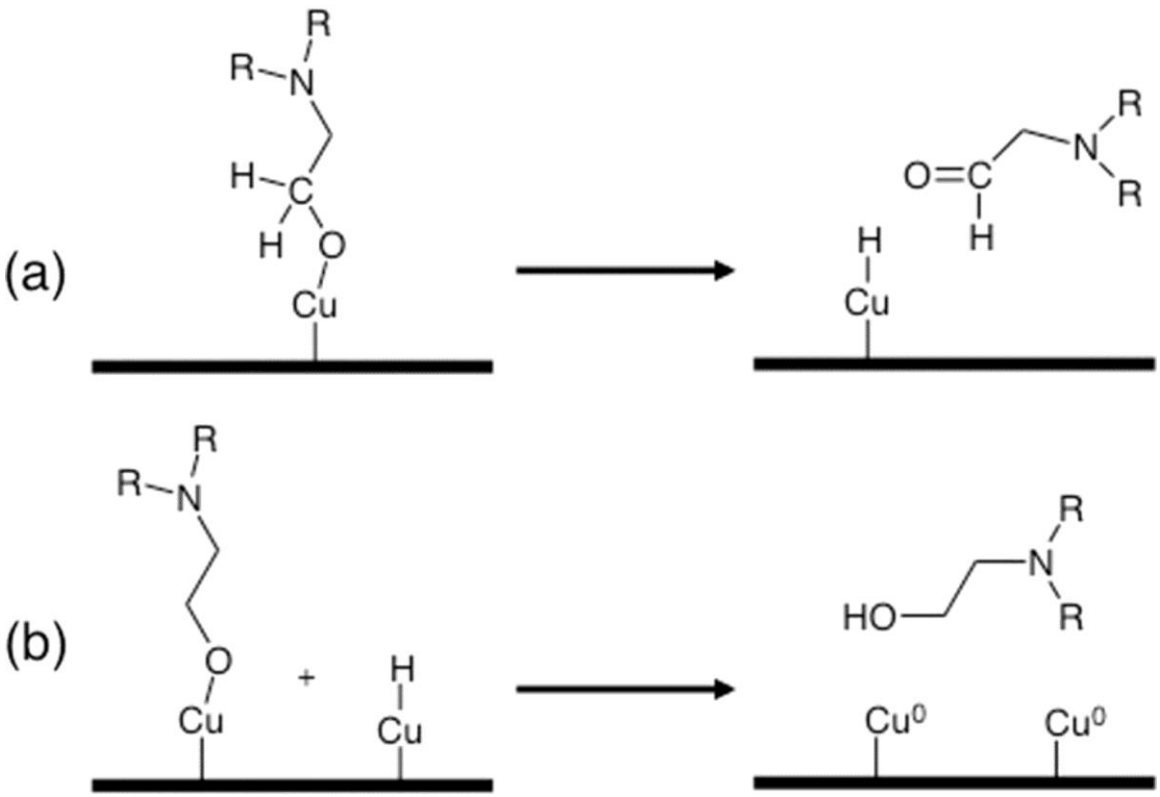

Figure 4.3.5: Reaction of chemisorbed copper dimethylaminoethoxide undergoing (a) beta-hydrogen elimination and subsequently (b) reductive elimination to produce copper metal from copper(II) dimethylaminoethoxide.

Similar compounds were used to deposit copper at the National Research Council Canada in 2001.[102] Here, the ligands were of the general formula O-CR_2-CH_2-NHR′, where R was CH_3 or CF_3, and R′ was tert-Bu or $CH_2CH_2OCH_3$. The best deposition had a precursor evaporation temperature of 155°C and a deposition temperature of 250°C. The deposition rate was 19Å/min and the films (150nm) had a sheet resistance of 3.44μΩ·cm. These depositions again showed minimal impurities of oxygen and nitrogen.

Copper(II) dimethylamino-2-propoxide ($Cu(dmap)_2$) was used as a CVD precursor in 2003 at Ruhr-University Bochum along with the ethyl analogue

copper(II) diethylamino-2-propoxide ($Cu(deap)_2$).[66] The deposition of copper metal was found to occur without an external reducing agent at temperatures between 230 – 350°C for both compounds, with the precursor evaporated at 65°C for $Cu(deap)_2$ and 55°C for $Cu(dmap)_2$. The growth rate for both precursors was similar on silica, at about 50 – 75Å/min for $Cu(deap)_2$ and 13 – 30Å/min for $Cu(dmap)_2$, with growth rate increasing with deposition temperature. The films were found to produce their best resistivities (2.16 – 2.19μΩ·cm, 1.8 – 4.0μm) at 260°C. Although there was surface oxygen present as an impurity, the bulk of the film had undetectable levels of impurities.

The first ALD process reported in the literature was by Hanyang University, using an aminoalkoxide was Cu(II) dimethylamino-2-methyl-2-butoxide ($Cu(dmamb)_2$) and hydrogen plasma.[67] The process showed saturated growth at 150°C after 3s of the copper precursor exposure. The growth rate was 0.65Å/cycle and this film (10nm) showed good wetting and a resistivity of 5.2μΩ·cm when deposited on Ta. The growth rate increased to 1.5Å/cycle at 200°C, suggesting that this precursor started to undergo CVD growth at this temperature.

At the same time, the thermal ALD of copper metal using formic acid and hydrazine was reported from Wayne State University.[68] Herein, chemisorbed $Cu(dmap)_2$ was converted to copper(II) formate at the surface, and subsequently reduced with hydrazine at 120°C (Figure 4.3.6). The process saturated after a 1s pulse of $Cu(dmap)_2$, and produced low nitrogen and oxygen impurities, and about 1% hydrogen impurities. The films (40 – 50nm) showed resistivities of 9.6 –

16.4μΩ·cm and growth rates of about 0.5Å/cycle. Interestingly, at temperatures above 170°C, the growth rates dropped.

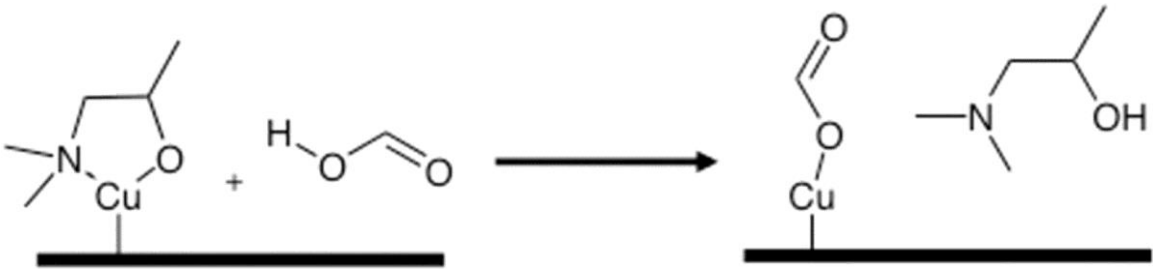

Figure 4.3.6: Exchange of a surface bound "dmap" ligand with formic acid to form a surface formate.

Tyndall undertook a study of the decomposition of formate by hydrazine.[103] They were able to show that ǁ-Cu-O-CH=O is indeed a stable surface species, and showed that the hydrazine undergoes homolytic cleavage to surface NH_2 moieties which then causes formate to decompose by abstracting a proton and producing carbon dioxide to produce copper metal (Figure 4.3.7).

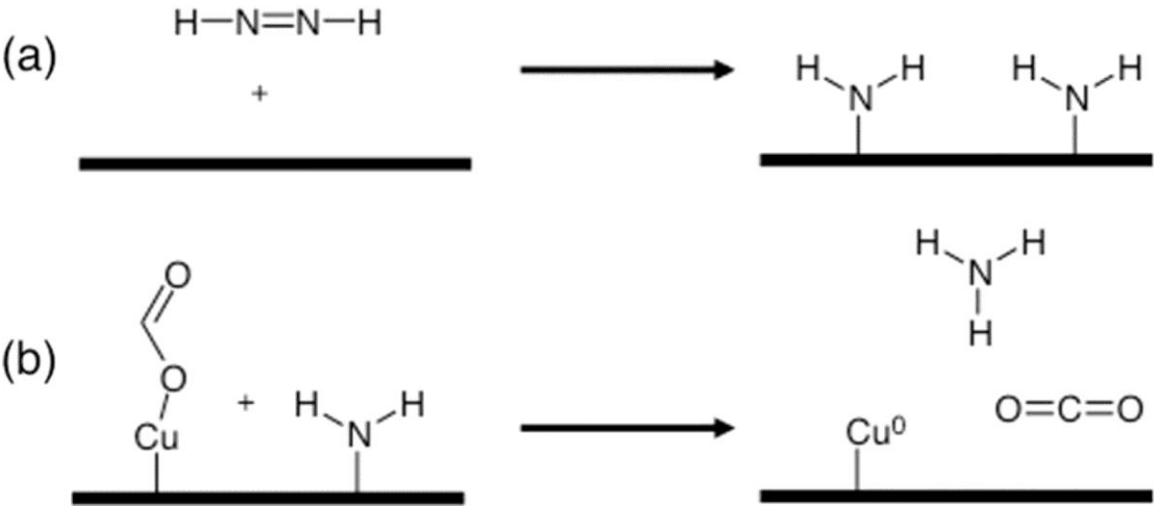

Figure 4.3.7: The surface reaction of hydrazine and subsequent reaction to produce copper metal from surface bound copper formate.

In 2014, $Cu(dmap)_2$ was used at Wayne State to thermally deposit copper

metal by ALD using borane dimethylamine as the coreactant.[69] The process had ALD window from 130 – 160°C, and showed saturated growth with a growth rate of 0.13Å/cycle on both Pd and Pt substrates with a 3s pulse of $Cu(dmap)_2$. At >170°C, the growth rate increased dramatically, showing that the substrate might activate $Cu(dmap)_2$ to undergo CVD at lower temperatures than on silica. The resistivity was similar to the Ru substrate, suggesting that the films were not very conductive. Interestingly, this process required a 50-cycle nucleation initiation step on ruthenium before growth started.

The aminoborane could also be used with formic acid to convert the copper-containing monolayer to formate in order for reduction to occur. In this case, the growth rate was 0.20Å/cycle on Pt and Pd with an ALD window of 135 – 165°C without the necessity of nucleation cycles. It should be noted that the resitivities reported for this process in Table 4.2.1 might be misleading, since the deposited copper formed alloys with the Pt and Pd in this process. Here, as in the previous use of formic acid, the growth rate dropped when the temperature was higher than 160°C. This paper suggests that dimethylaminoborane is acting as a reducing agent: we speculate this occurs by producing dihydrogen at the process temperature. The dihydrogen could then react with the monolayer to eliminate the parent ligand, and generate copper metal (Figure 4.3.8).

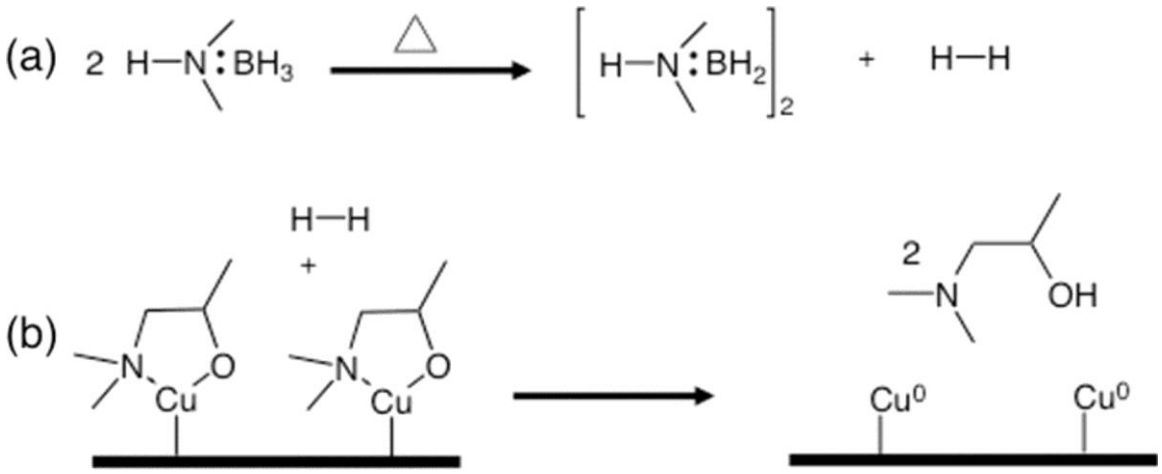

Figure 4.3.8: Dimethylaminoborane forming dihydrogen in the gas phase, and the subsequent reaction of dihydrogen to reduce surface-bound copper "dmap" to metallic copper.

Copper(II) dimethylamino-2-propoxide and related compounds all show similar, and very promising behavior. With low volatilization temperatures, these compounds undergo CVD at relatively low temperatures (~225°C), and can be activated by plasma hydrogen or novel thermal processes to produce copper thin films. In general, the surface chemisorbed precursors are stable up to about 160 – 170°C, where they typically undergo β-hydrogen abstraction and act as "single-source" precursors for copper metal.

Amidinates

Amidinates are relatively new precursors for CVD and ALD, with the first report of a copper(I) amidinate in 2005 from Harvard.[104] In this case, the compound was $[Cu(iPr\text{-}amd)]_2$, where iPr-amd is N,N′-diisopropyl-acetamidinate. The virtue of amidinates and guanidinates are their flexibility with respect to replacing alkyl groups, and the Harvard group ultimately published a paper

reporting the use of the secondary butyl version of this precursor for copper metal deposition.[70] This precursor was used with hydrogen as a reducing agent. It was evaporated at 100°C, and deposition occurred at 185°C. The copper film (80nm) was granular, but on alumina it had a resistivity of 2.9μΩ·cm. The authors speculate that the mechanism of the deposition is protonation of the amidinate by dihydrogen, thus reducing the Cu(I).

Interestingly, $[Cu(iPr\text{-}amd)]_2$ was used for CVD deposition of copper metal in 2009.[71] Here, the precursor was heated to 95°C, and the deposition was carried out between 200 – 300°C with hydrogen as a reducing agent. At 280°C, the films (270nm) had a resistivity of 4μΩ·cm, and the process had a growth rate in the mass-transport limited regime of 2.0 – 4.2Å/min. This same group found that this precursor would decompose at 140°C without hydrogen.[105] This corroborated decomposition work that was under taken at UC-Riverside.[106] These works highlight the fact that the copper amidinate compounds undergo very slow decomposition at 140°C that accelerates when temperatures reach >200°C. The ligand undergoes complex fragmentation at these high temperatures (Figure 4.3.9).

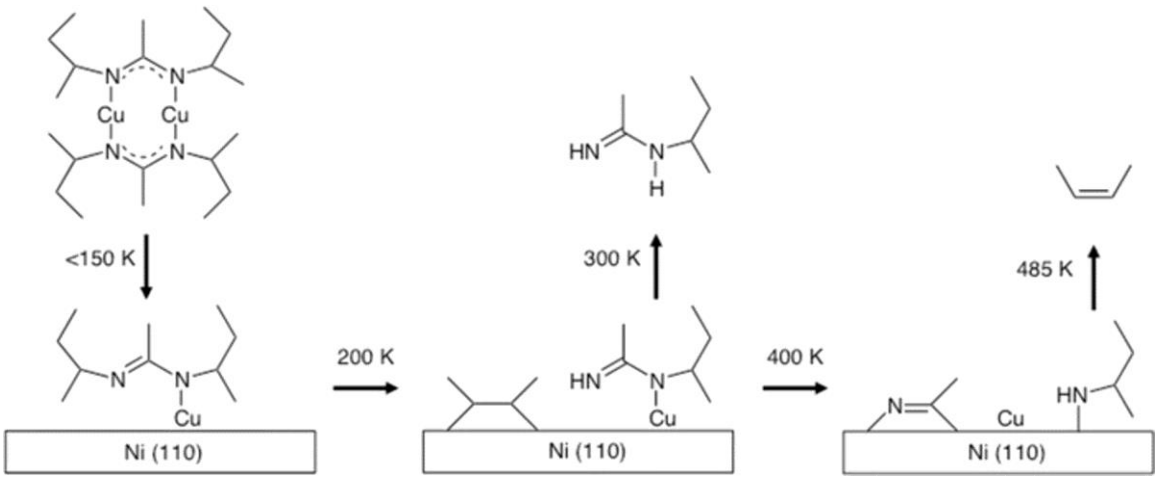

Figure 4.3.9: Thermal fragmentation of copper(I) amidinate at a nickel surface with increasing temperatures.

This thermal profile is mirrored by copper guanidinates, although the thermolysis follows a different path.[107] Here, copper metal was found to deposit without a reducing gas at 225°C. Further exploration of the decomposition showed that Cu(I) guanidinates decompose by β-hydrogen elimination (Figure 4.3.10). This copper guanidinate $[Cu(iPr\text{-}guan)]_2$ where iPr-guan is N, N′-diisopropyl-N",N"-dimethylguanidinate was later shown to deposit copper metal as low as 200°C using pulsed CVD at Carleton University.[72] The precursor was evaporated at 125°C and was used without a reducing agent. The copper film was deposited on an optical fibre, and the growth rate was 18Å/min, based on the pulse length of the deposition.

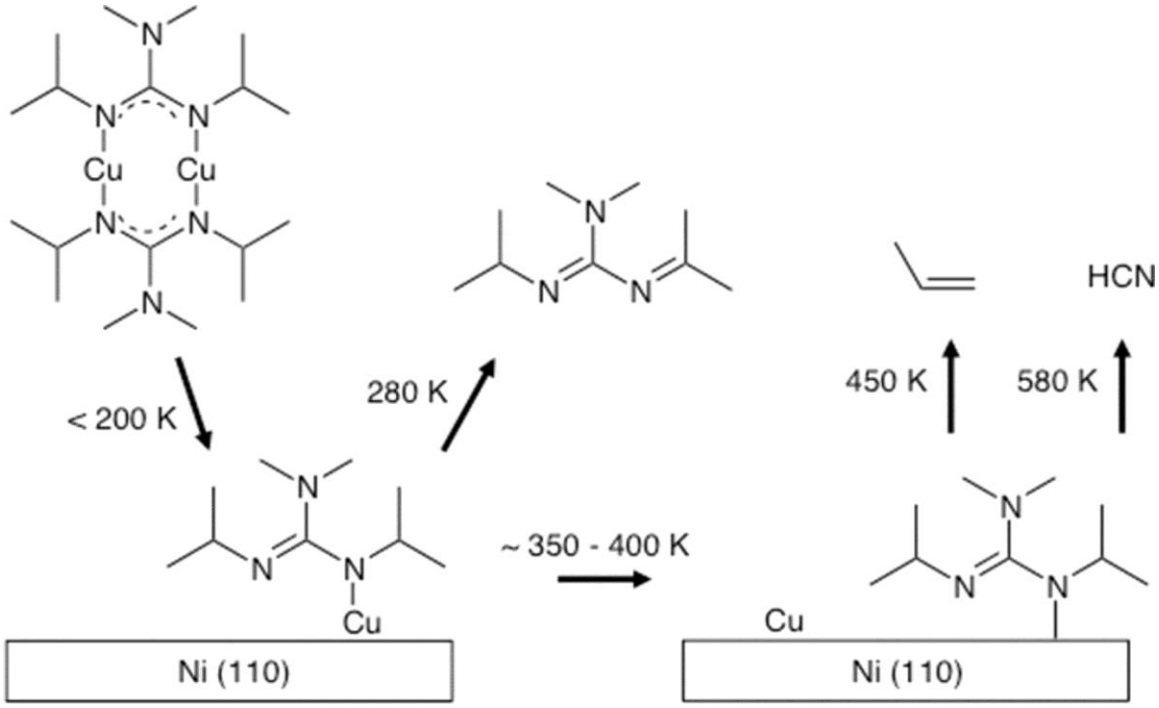

Figure 4.3.10: Thermal fragmentation of copper(I) guanidinate at a nickel surface with increasing temperatures.

Typically, Cu(I) precursors have a tendency to disproportionate at a surface. However, very careful investigation of the surface chemistry of $[Cu(guan)]_2$ was undertaken by matrix-isolated IR and TOF-MS analysis[10], and no evidence of this disproportionation was found. This is striking, considering the strong evidence for this disproportionation as a major thermal decomposition pathway for surface species containing β-diketonates. Amidinates and guanidinates do not show significant improvement in their range of thermal deposition, and the switch-over between ALD to CVD growth occurs around 225°C. This is in line with other precursor families.

Thermolysis can be tuned in these systems by redesigning the amidinate so that it lacks the ability to undergo β-hydrogen elimination. By using

iminopyrrolidinates with judiciously placed methyl groups, the temperature of the onset of thermolysis can be raised by over 200°C (Figure 4.3.11).[108] Although the ligand undergoes some decomposition at 275°C, there is still an intact, chemisorbed monolayer at 350°C, and copper metal formation is not seen until above 400°C. Although high temperature copper deposition by CVD is not particularly sought after, this thermally stable precursor may show promise for ALD applications.

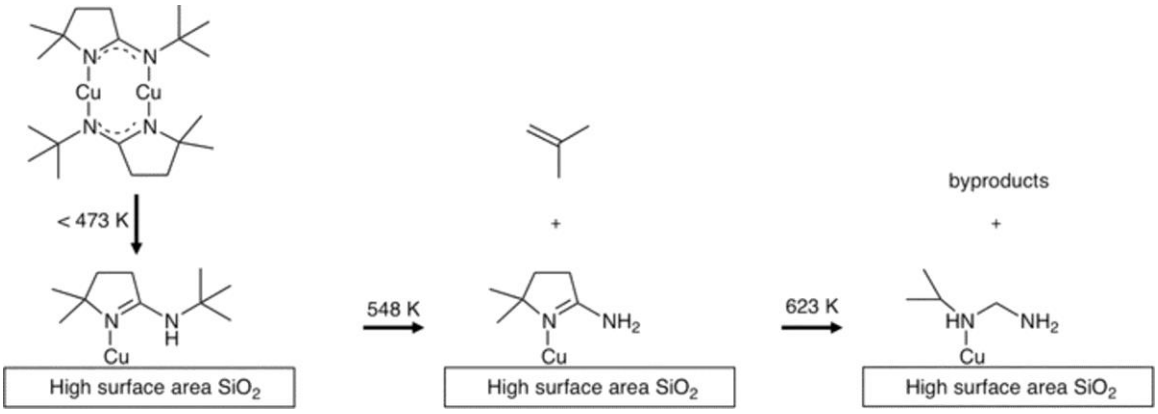

Figure 4.3.11: The decomposition of copper(I) "dtip" at elevated temperatures.

Betadiketonates and Betaketoiminates

Copper β-diketonates exist for both oxidation states: Cu(II) β-diketonates are typically monomers, while Cu(I) β-diketonates typically have an attendant ligand to saturate their coordination sphere. The CVD of copper β-diketonates has previously been the subject of an excellent review, and so a summary of these precursors is presented in the following paragraph.[73,74]

Copper(II) bis(acetylacetonate) ($Cu(acac)_2$) evaporates between 180 – 200°C and deposits copper metal between 225 – 250°C with hydrogen as a

coreactant. Generally, fluorination improves the volatility of this compound while increasing the deposition temperature, with copper(II) bis(trifluoroacetylacetonate) ($Cu(tfac)_2$) evaporating between 135 – 160°C and depositing between 250 – 300°C and copper(II) bis(hexafluoroacetylacetonate) ($Cu(hfac)_2$) evaporating at 120°C and depositing metal between 340 – 390°C. This hexafluoro precursor also can be used in its monohydrate form ($Cu(hfac)_2 \cdot H_2O$), which drastically lowers the evaporation temperature to between 30 – 60°C and the deposition temperature to 250 – 350°C. Interestingly, this precursor also produces a lower resistivity copper film (1.9 – 2.8μΩ·cm) compared to the water-free precursor (3 – 6μΩ·cm). Thus, it appears that the fear that an equivalent of water might produce some copper oxide is ungrounded. Other β-diketonate ligands on Cu(II) fall into these ranges for evaporation, deposition, and resistivity.

Copper(I) β-diketonates overshadow the Cu(II) precursors by having much lower volatilization temperatures as well as lower deposition temperatures. In this oxidation state, the copper precursor is supported by an ancillary ligand. There are many examples of this precursor family listed in the very thorough review by Rickerby and Steinke,[74] and these show a range of volatilization temperatures from 35 – 77°C and deposition temperatures from 30 – 420°C. As an example, Cu(hfac)·vtms where vtms is vinyltrimethylsilane (known by the trade name “Cupraselect”) has an evaporation temperature of 50°C and a deposition range of 75 – 420°C. This large range for both evaporation and deposition makes this family of CVD precursors very useful in many different applications.

The surface chemistry of the β-diketonates (bdk) changes depending on copper's oxidation state. In the case of $Cu(bdk)_2$, the surface decomposition chemistry has been shown to follow the typical CuL_2 decomposition of loss of one ligand to the growing surface, followed by combination of the ligand with an adsorbed hydrogen atom to produce the protonated ligand.[109] This same study showed that Cu(bdk)·L, where L is a coordinative ligand, undergoes disproportionation. After coordination to the surface and loss of the coordinative ligand, the copper disproportionates, and the Cu(II) center carries away the surface-bound ligands:

$$Cu(bdk)\cdot L_{(g)} \rightarrow \| \text{-} Cu(bdk) + L_{(g)}$$

$$2 \| \text{-} Cu(bdk) \rightarrow \| \text{-} Cu^0 + Cu(bdk)_{2(g)}$$

It is reasonable to expect that this surface etching limits the growth rate of the copper(I) precursors compared to the Cu(II) precursors. However, this is not the case, and the Cu(I)(bdk)·L precursors have higher growth rates than their Cu(II) cousins because of the kinetics of growth. In fact, $Cu(hfac)_2$ has a growth rate at 350°C of 4.0 – 10Å/min,[76] depending on substrate while Cu(hfac)·vtms has a growth rate of greater than 140Å/min at 200°C.

The ALD of copper metal from β-diketonates is dominated by Cu(II). Initially, the thermal deposition of copper metal using $Cu(acac)_2$ and H_2 was reported by the Technical University of Helsinki (now Aalto University).[77] The $Cu(acac)_2$ was volatilized at 130°C and deposition occurred at 250°C. Copper

metal was deposited on glass, Si, Al, and Ti substrates, but the report gave no other deposition data. Plasma-assisted ALD of copper metal using dihydrogen was demonstrated at the University of Helsinki in 2005.[78] Here, the precursor was evaporated at 125°C and the substrate was kept at 140°C. The growth saturated at around 5s pulse time of $Cu(acac)_2$. The process had a growth rate of 0.18Å/cycle and the copper films showed a resistivity of 15μΩ·cm (25nm) on a variety of silicon, glass, and conductive substrates. These results were corroborated by a similar study carried out at SUNY.[79]

A related $Cu(bdk)_2$ was reported to undergo ALD deposition of copper in 1998 from Uppsala.[80] In this case $Cu(thd)_2$ was used, where thd is 2,2,6,6-tetramethylheptane-3,5-dionate: the tert-butyl analogue of acac. A Pt/Pd seed layer was used to nucleate the copper film, and substrate temperature was varied between 150 – 350°C. The precursor was evaporated at 120°C. Growth saturated at about 3s and the film (60nm) had a growth rate of 0.36Å/cycle and a resistivity of 8μΩ·cm. These values were corroborated by other studies,[81,82] and a higher growth rate of 0.7Å/cycle was found in one instance.[83] $Cu(thd)_2$ was also used to deposit copper metal using plasma assisted ALD at Rensselaer Polytechnic Institute in 2005.[84] The process used an evaporation temperature of 123.5°C with the Pt and silica substrates held at 180°C. In the absence of hydrogen plasma, no copper growth was seen before 400°C, which agrees with the previously reported CVD studies. The growth rate of copper metal was found to be 0.12Å/cycle, and varied with substrate. Interestingly, this study found that the growth had a CVD component at 250°C, which suggests that the plasma left

an active surface species that, permitted some CVD growth.

$Cu(hfac)_2 \cdot H_2O$ was also used as a thermal ALD precursor.[85] Here, the precursor was heated to 75°C. Several reducing agents were used, including methanol, ethanol and formaldehyde. The best film was grown at 300°C using formaldehyde as the reducing agent on a silica substrate. The resistivity was 1.78μΩ·cm (120nm), but no saturation curve or growth rates were reported. Interestingly, fluorine was not found as an impurity, and less than 2% of oxygen and a trace of carbon were found. The authors proposed a mechanism for alcohol reduction at the surface, but since it is not chemically balanced and involves some unsubstantiated side-products, the surface chemistry of this interesting process needs further study.

Another interesting thermal ALD process using $Cu(hfac)_2$ and H_2 was shown with pyridine as a catalyst.[86] The copper was deposited on TiN with the pyridine added during the dihydrogen pulse. The precursor was evaporated at 60°C and depositions were performed from room temperature to 100°C. The growth rate was 0.185Å/cycle and the resistivity was 19μΩ·cm (15nm). The films showed higher than normal impurities, with carbon ranging from 5 – 16% and oxygen from 4 – 5% over the deposition range. The role of pyridine was clarified by computational analysis: the pyridine stabilized the copper center as a coordinative ligand, but also weakened the Cu–O bond in the surface species by interacting with the bridgehead proton in the hfac ligand. This allowed the surface species to react with adsorbed hydrogen adatoms at lower the typical temperatures (Figure 4.3.12).

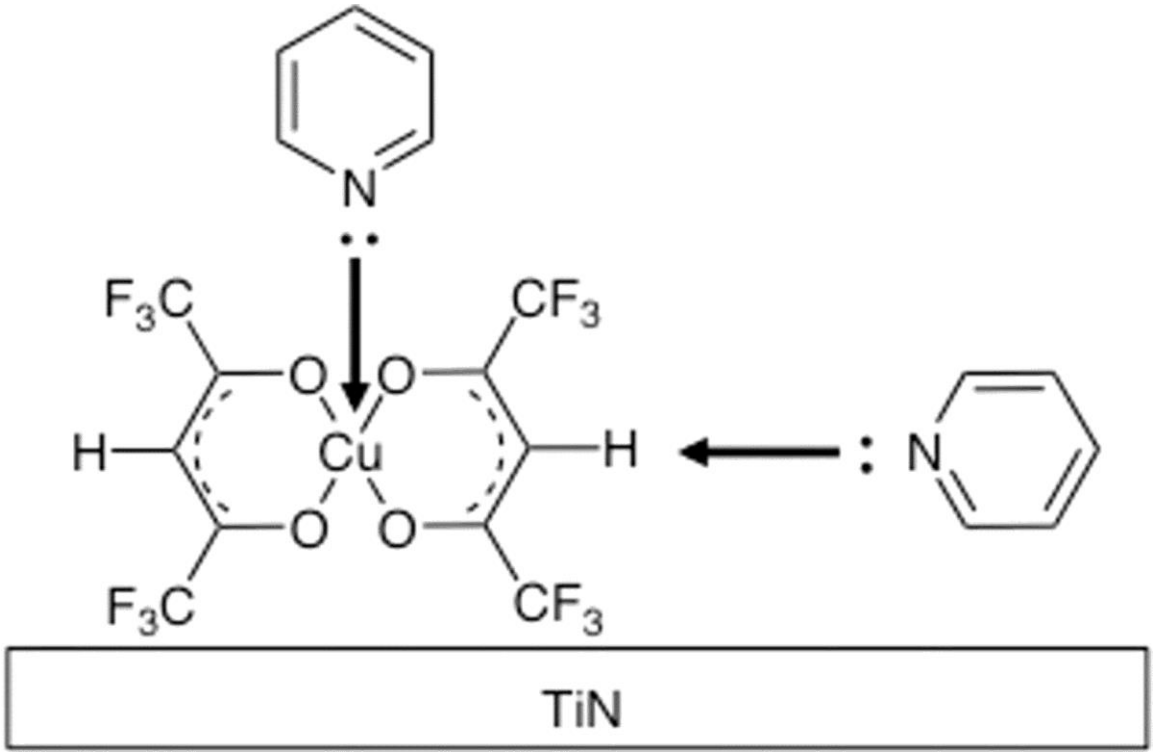

Figure 4.3.12: Stabilization of copper by pyridine, and activation of the copper-oxygen bond through interaction with the hexafluoroacetylacetonate ligand.

The only example of a Cu(I) precursor employing a β-diketonate comes from Hanyang University.[87] This group reports plasma-assisted ALD of copper metal from the precursor Cu(hfac)·vtmos where vtmos is vinyltrimethoxysilane. The precursor was evaporated at 60°C, and deposition was seen between 200 – 300°C on TiN using hydrogen plasma. The growth rate was 0.5Å/cycle and the resistivity was 2μΩ·cm (40nm).

4.4 Conclusions

In general, the deposition of copper metal by thermal atomic layer deposition can be accomplished using a wide variety of precursors exhibiting a wide variety of evaporation rates and decomposition mechanisms. However, it

stands out that ALD of copper, in general, starts to show CVD behavior around 200 – 230°C. This is a surprisingly small range, considering significant differences in the ligands described above. This highlights the fact that chemisorption, and the lower thermal limit of that process, is a very important factor in designing ALD processes, and the second precursor that is used can activate copper metal deposition at surprisingly low temperatures.

With respect to CVD, the picture is also clear: given the success of the copper(I) β-diketonate family, any new copper precursor of metallization would have to be remarkable and remarkably versatile to compete as a process. However, there is significant opportunity in process design, and given the ranges of CVD process temperatures, CVD can still compete with ALD to deposit low temperature copper metal films.

Chapter 5 – Novel Copper Compounds: Characterization and Thermolysis

5.1 Abstract

Copper metal atomic layer deposition (ALD) is an important process for the microelectronics industry. The conformality that is achievable by this approach is unrivaled by any other industrial process due to the self-limiting nature of ALD that allows precise, incremental film growth. The challenge with thin copper films arises at the nanoscale where grain boundaries really begin to impact the conductivity of the film. Although many volatile precursors have been reported,[110] there is still a driving force for discovering new precursors that promote film purity and single crystallinity to achieve the best conductivity. The challenge of precursor design is in tuning the physical properties of the compound. Ligands on the metal center play an important role in this and often, subtle changes to the ligand can impart dramatic changes thermal behavior of the compound as a whole, for example changing the pendant R groups or a ligand can change the molecular weight and other physical characteristics such as crystal structure.

The syntheses of new N-heterocyclic carbene – copper (I) – (L) where L is an easily interchangeable amide, including N-acetyl benzamide (**1**), diacetamide (**2**) and acetyl acetone (**3**) are described herein. These compounds have been shown by thermogravimetric analysis to have low onsets of volatility (<195°C) and residual masses of 10.1, 18.0, and 5.8%, respectively. The trends in volatility, thermal stability and reactivity in these three compounds will be the focus of this

study to identify new precursors for copper metal deposition. Facile, nearly quantitative synthesis from commercially available starting material makes these precursors interesting candidates for future copper film deposition.

5.2 Introduction

As described in Chapter 4, many copper precursors exist but there is still motivation to explore new complexes. Recently, a promising precursor, 1,3-diisopropyl-imidazolin-2-ylidene copper hexamethyl disilazide, was reported by our group.[111] The N-heterocyclic carbene moiety stabilizes the copper metal centre and promotes a monomeric structure (Figure 5.2.1). The hexamethyldisilizine ligand is a strong Lewis base so it stabilizes the copper centre, however, the $Si(Me)_3$ groups are relatively heavy. A lighter ligand may increase volatility and decrease the deposition temperatures reported (~220°C).

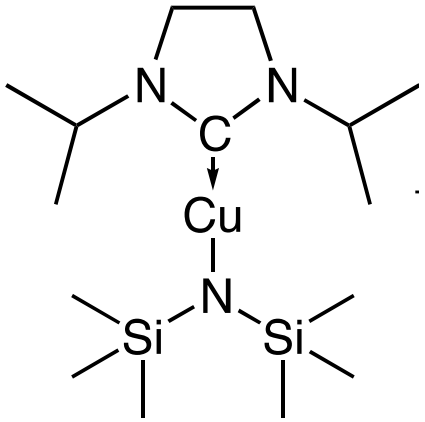

Figure 5.2.1: Structure of 1,3-diisopropyl-imidazolin-2-ylidene copper hexamethyl disilazide.

Typically, copper precursors avoid heteroatoms like oxygen that can potentially contaminate growing films. However, if the ligand is stable and volatile on its own, it can potentially be removed and not incorporated during the CVD or

ALD process. An interesting ligand, N-acetylbenzamide, has recently been reported in phosphite-stabilized Ag(I) complexes.[112] CVD depositions resulted in Ag films with no silver oxide detectable by EDX. The oxygen content of the N-acetylbenzamide ligand did not promote silver oxide formation and perhaps it would be similar in the case of copper. The reactivity of 1,3-diisopropyl-imidazolin-2-ylidene copper hexamethyl disilazide is tested here with weakly acidic N-acetylbenzamide, diacetamide and acetylacetone ligands to undergo ligand exchange and generate lower molecular weight copper precursors that would ideally have lower onsets of volatility than 1,3-diisopropyl-imidazolin-2-ylidene copper hexamethyl disilazide.

5.3 Results and Discussion

Thermogravimetric Analysis of Ligands

The volatility of neutral ligands, N-acetylbenzamide and diacetamide was evaluated by thermogravimetric analysis. Thermally combusting copper compounds may release detectable amounts of protonated ligand therefore determining whether the ligands themselves are volatile is an important step in the design of a new precursor. Figure 5.3.1 shows both ligand TGA traces. Each compound was subjected to a temperature ramp rate of 10°C/min, under nitrogen atmosphere at a flow rate of 40mL/min. N-acetylbenzamide (31mg), volatilized completely from the pan in about 23 min. The onset of volitalization, where about 5% of the initial mass was lost, was about 147.6°C and no mass remained after

226°C. Diacetamide (24mg) also volatilized completely, in about 15 min. The onset of volatilization was about 82.6°C and 0% mass remained after 147°C.

The derivative curves of both traces showed a relatively smooth curve followed by a sharp, asymptotic descent is a good indicator of a volatilization event over decomposition. Both ligands were chosen to study on copper due to their lack of thermal decomposition, although it is likely that diacetamide was a better choice due to its smaller size, lack of bulky R groups and its demonstrated lower onset of volatility.

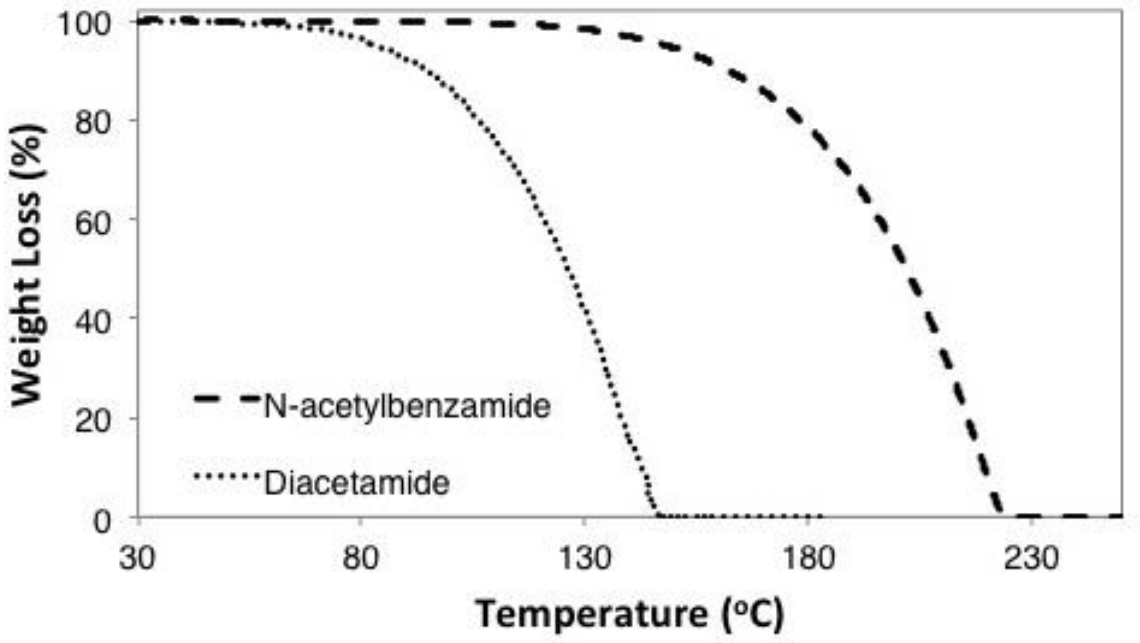

Figure 5.3.1*:* Thermogravimetric analysis curves of protonated ligands: N-acetylbenzamide and diacetamide.

Synthetic Procedure

The copper starting material is commercially available. A solution of N-acetylbenzamide was slowly added to a stirring solution of 1,3-diisopropyl-imidazolin-2-ylidene copper hexamethyl disilazide. After stirring for 23 h, the solvent was evacuated and solid **1** was isolated. This simple transamination reaction produced hexamethyldisilizane that was also removed under reduced pressure. Figure 5.3.2 depicts the reaction scheme.

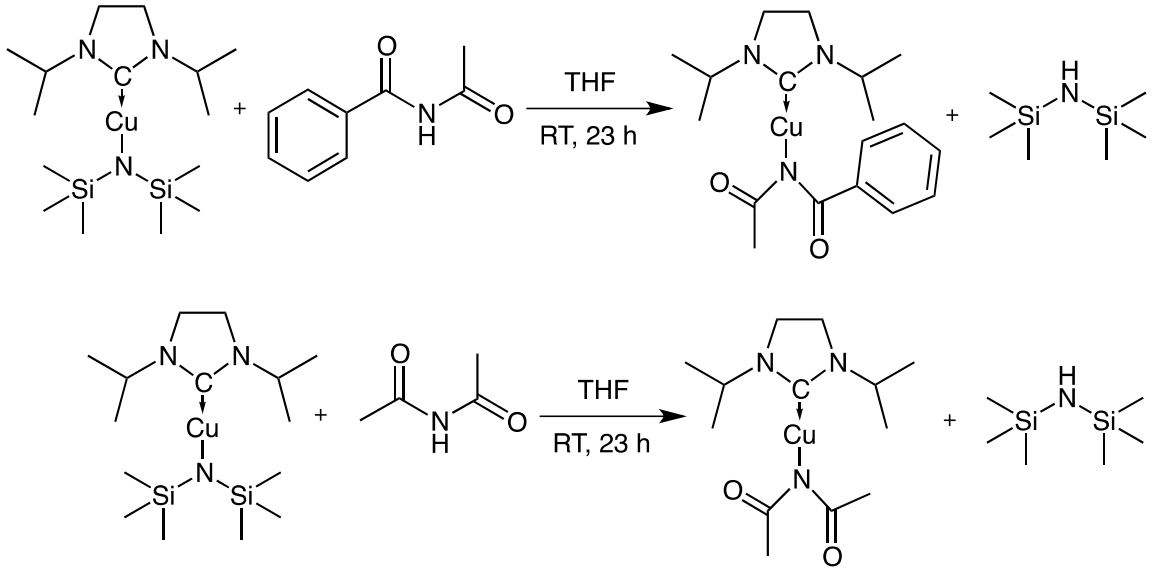

Figure 5.3.2: Synthetic scheme of **1** (top), and **2** (bottom).

Compound **1** was recrystallized from THF in good yield and characterized by ^{1}H and ^{13}C NMR. All expected chemical shifts were present in the NMR spectra, with negligible solvent (THF) impurity. An IR spectrum was collected of **1** to determine the ligand coordination to the copper. The N–H stretch in free N-acetybenzamide disappeared, indicating deprotonation and reaction with 1,3-diisopropyl-imidazolin-2-ylidene copper hexamethyl disilazide. The carbonyl

stretch shifted from 1736.5cm^{-1} to 1727.4cm^{-1} and the conjugated carbonyl stretch shifted just 1679.1cm^{-1} to 1680.7cm^{-1} after reaction. Delocalization of the anionic charge into the carbonyl group would decrease the bond order and lower the frequencies of the carbonyl stretches by a significant amount; a 58 – 115cm^{-1} shift was reported for Ag complexes[112]. The relatively small aforementioned shifts indicate the carbonyl is not participating in bonding with the Cu metal centre; this is further supported by the crystal structure, vide infra. Compound **1** had a relatively low bench top melting point of 98 – 102°C.

Compound **2** was synthesized in an analogous route to **1**, shown in Figure 5.3.2. It was recrystallized from THF in 93% yield and characterized by ^{1}H and ^{13}C NMR. Difficulties were met in trying to grow a crystal of good enough quality for single crystal x-ray diffraction. In all recrystallization attempts, very small, powder-like crystals were attained.

Compound **3** was synthesized to determine whether the weak acid, acetylacetone, would also displace the hexmethyldisilazide moiety (Figure 5.5.3).

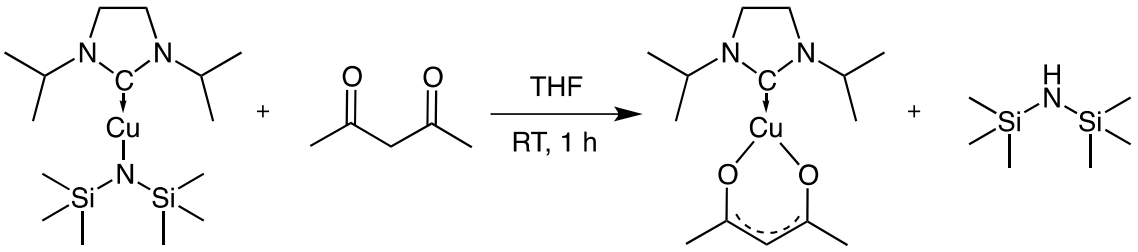

Figure 5.3.3: Synthetic scheme of **3**.

The chemical reaction took place in about one hour. The strongly basic

hexamethyldisilazide moiety quickly deprotonated acetylacetone and formed solid green **3** which was recrystallized from THF in a 75% yield and analyzed by ^{1}H NMR and ^{13}C NMR in deuterated benzene. All chemical shifts were observed as expected. Single crystal XRD revealed the crystal structure of **3** and is discussed below.

Single Crystal X-ray Diffraction

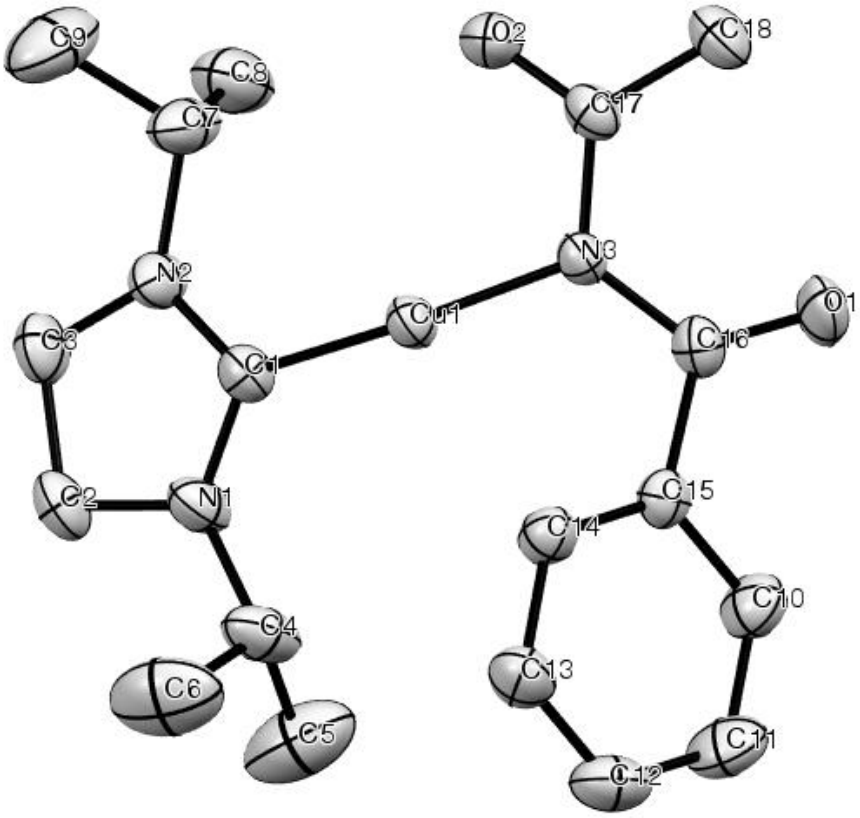

Figure 5.3.4: Molecular structure of **1**. Thermal ellipsoids are drawn at 50% probability, and the H atoms have been omitted for clarity.

Table 5.3.1: Metrical Data for 1

Selected Bond Lengths (Å)			
Cu1 – N3	1.892(1)	C1 – N1	1.335(2)
Cu1 – C1	1.882(2)	C1 – N2	1.328(3)
C1 – N2	1.328(3)	Cu1 – O2	2.782(1)
Selected Bond Angles (°)			
N1 – C1 – N2	108.8(1)	C16 – N3 – C17	122.8(1)
N3 – Cu1 – C1	174.51(7)		

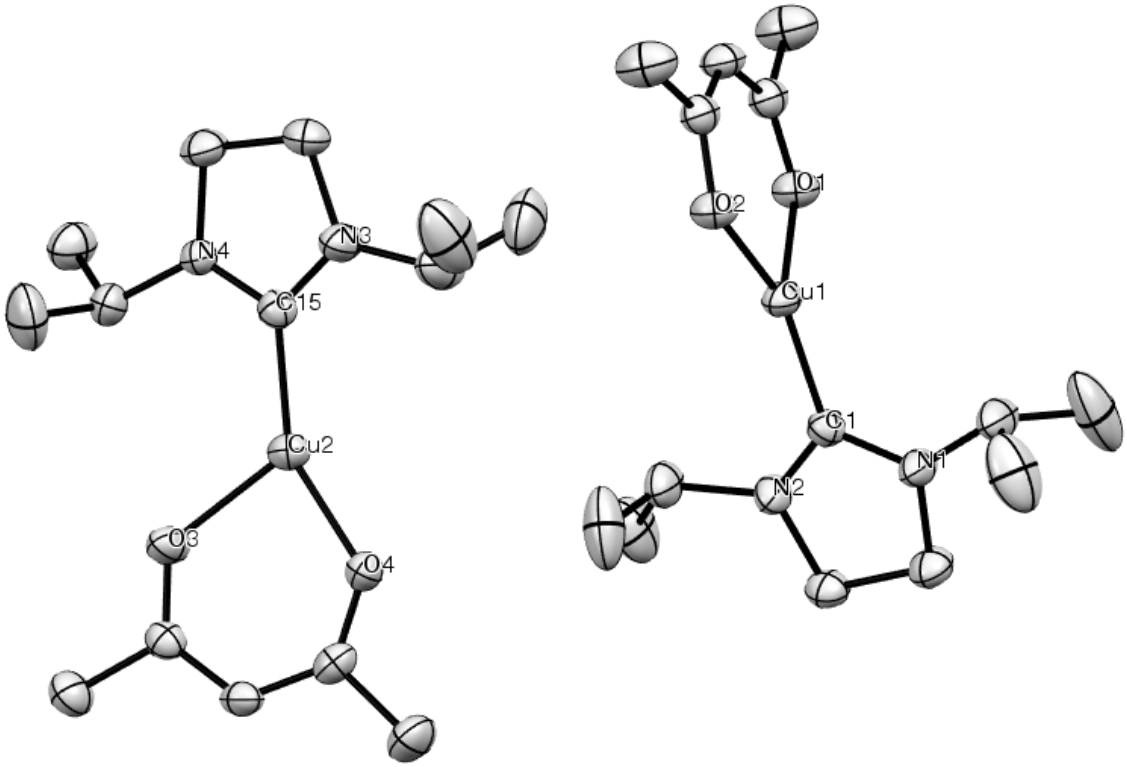

Figure 5.3.5: Molecular structure of **3**. Thermal ellipsoids are drawn at 50% probability, and the H atoms have been omitted for clarity.

Table 5.3.2: Metrical Data for 3

Selected Bond Lengths (Å)			
Cu1 – C1	1.872(2)	Cu2 – C15	1.889(2)
Cu1 – O1	2.018(2)	Cu2 – O3	2.119(1)
Cu1 – O2	1.926(2)	Cu2 – O4	1.936(1)
C1 – N1	1.333(2)	C15 – N3	1.336(2)
C1 – N2	1.336(2)	C15 – N4	1.335(2)
Selected Bond Angles (°)			
N3 – C15 – N4	107.51(1)	N1 – C1 – N2	107.51(1)
O3 – Cu2 – O4	89.50(5)	O1 – Cu1 – O2	92.8(1)

Table 5.3.3: X-ray Data for 1, and 3		
	1	**3**
empirical formula	$C_{18}H_{26}N_3O_2Cu$	$C_{14}H_{25}N_2O_2Cu$
Fw	379.96	316.90
cryst syst	monoclinic	monoclinic
space group	P 2_1/n	P 2_1/c
a (Å)	10.5071(5)	19.499(4)
b (Å)	16.3708(8)	9.9006(17)
c (Å)	12.3774(6)	17.827(3)
α (deg)	90	90
β (deg)	113.9250(10)	109.198(4)
γ (deg)	90	90
V (Å^3)	1946.1	3250.14
Z	4	8
Z'	0	0
D_c (kg/L)	1.297	1.295
μ (mm^{-1})	1.136	1.344
T(^{o}C)	200(2)	200(2)

The structure of **1** was in a *P2$_1$/n* space group, without an inversion centre located in the middle of the molecule (Figure 5.3.4, Table 5.3.1). The copper atom is in a linear coordination with the N3 – Cu1 – C1 bond angle of 174.51(1)°. The N-acetylbenzamide ligand coordinated with the copper atom in a monodentate fashion with bond lengths of 1.892(1)Å for Cu1 – N3. For 1,3-diisopropyl-imidazolin-2-ylidene copper hexamethyl disilazide, the comparable Cu – N3 bond length was reported to be 1.836(4)Å.[111] The lengthening of this

bond may be beneficial in an ALD process where this bond may be relatively easier to break. Interestingly, the carbene bond to the metal, Cu – C1, is unchanged in the two structures; 1.872(2)Å and 1.870(5)Å[111], respectively. The phenyl ring is twisted outwards with the Cu1 – N3 – C16 – C15 torsion angle of -39.5(2)°. Surprisingly, packing within the unit cell reveals some hydrogen bonding, but does not show stacking of the π-systems of the phenyl groups (Figure 5.3.6). This strong interaction is why phenyl groups are often avoided in precursor design. In comparison with **2**, which lacks this R-group, it is likely that the mass of the extra carbons contributes to the higher melting point and higher onset of volatility rather than π-π interactions.

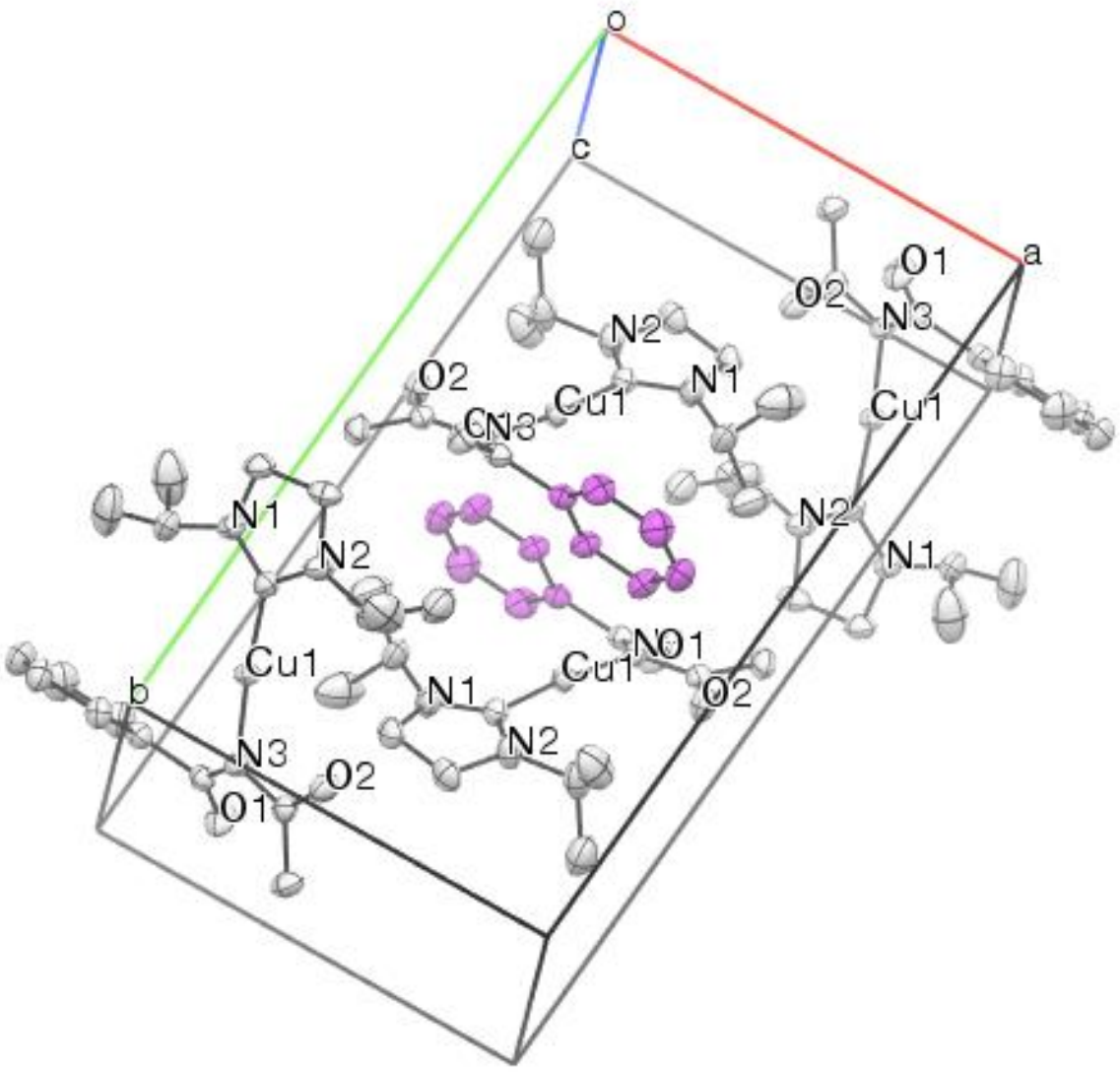

Figure 5.3.6: Crystal structure unit cell for **1**.

The structure of **3** was in a P $2_1/c$ space group (Figure 5.3.5). The acetylacetone ligand is chelated in a bidentate fashion to the copper atom. The intramolecular Cu – O bond lengths in both conformers were slightly different from one another, likely due to packing forces in the solid phase (Table 5.3.2). Interestingly, the two conformers differ in the orientation of the acetylacetonate ligand with respect to the NHC ligand. The torsion angle between O1 – Cu1 – C1

– N1 is 92.3(2)° and O2 – Cu1 – C1 – N2 is 89.9(2)°. Alternatively, the torsion angle between O3 – Cu2 – C15 – N3 is nearly planar at 169.9(1)° and O4 – Cu2 – C15 – N4 is -175.9(1)°, again due to packing forces.

Thermogravimetric Analysis of Copper Compounds

Compound **1** (6.36mg) was analyzed by thermogravimetric analysis at a ramp rate of 10°C/min following a brief isotherm at 70°C to remove any excess THF solvent (Figure 5.3.7). The onset of volatilization was 194.7°C and residual mass at the end of the experiment was 10.1%. The colour of the platinum TGA pan was slightly copper-tinged. The calculated molecular percentage of copper in the compound is 16.72%. Along with an irregular derivative curve, this supports the conclusion that as temperature was increased in the experiment, **1** was volatilizing as well as decomposing to some degree. Based on the colour of the pan, some copper component remained but since the residual mass was below 16.72%, some copper precursor must have volatilized as well. This thermal behavior is not ideal for an ALD precursor because it would likely decompose in the precursor container (or bubbler) and at low bubbler temperature, i.e. near 194.7°C, vapour pressure may not be adequate. However, this precursor may be useful for a simple CVD reactor where the vapour would not need to travel very far to the substrate.

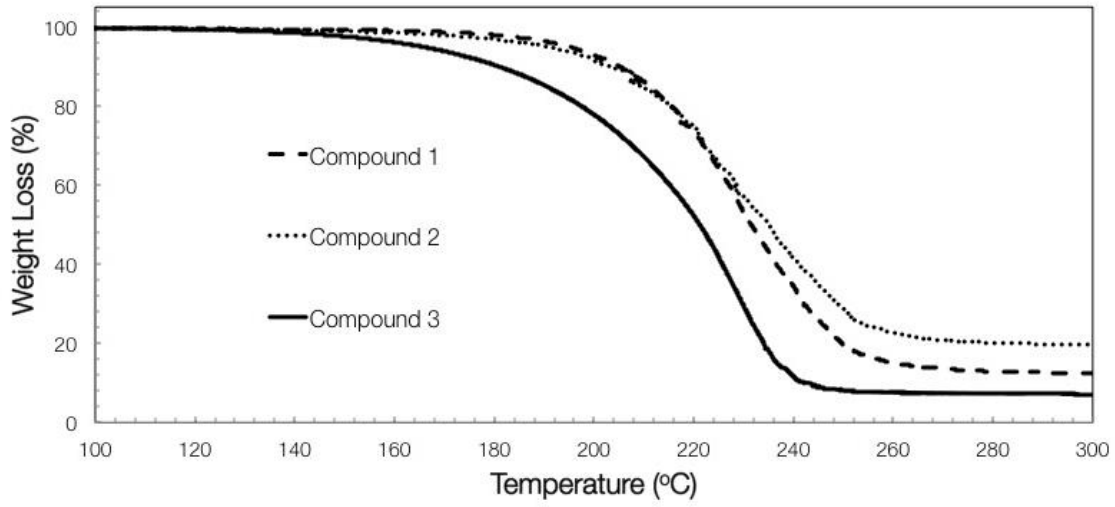

Figure 5.3.7: Thermogravimetric analysis curves of **1**, **2** and **3**.

Thermogravimetric analysis of Compound **2** (22.24mg) was undertaken under similar conditions but with a ramp rate of 7°C/min following a brief isotherm at 60°C to remove any excess THF solvent (Figure 5.3.7). Due to a technical problem with the thermocouple of the TG analyzer, the temperature ramp rate was decreased to afford a more accurate curve. The onset of volatilization was 190.2°C and residual mass was 18.0%. The colour of the platinum TGA pan was slightly copper-tinged. The calculated molecular percentage of copper in the compound is 20.0%. The small difference between the residual mass and percentage of copper in the compound, and the remaining copper colour, are strong indicators that a high degree of decomposition occurred during the experiment. Interestingly, **1** was more volatile than **2**, even with the extra mass of the phenyl ring. Typically, intermolecular forces between phenyl rings increases the volatilization temperature, as more energy is required to break these bonds.

Thermogravimetric analysis of Compound **3** (13.28mg) was undertaken under similar conditions but with a ramp rate of 10°C/min (Figure 5.3.7). The onset of volatilization was 165.4°C and residual mass was 5.8%. The colour of the platinum TGA pan was black and slightly copper-tinged. The calculated molecular percentage of copper in the compound is 20.1%. This compound showed the most promise as a potential precursor, as it showed the least amount of thermal decomposition and had the earliest onset of volatility.

5.4 Experimental

Genereal Considerations: All manipulations involving the synthesis and handling of copper(I) compounds were performed in a nitrogen filled drybox. The chemical diacetamide, and acetic anhydride, were purchased from Aldrich Chemical Company and used as received. 1,3-diisopropyl-imidazolin-2-ylidene copper hexamethyl disilazide was supplied by Green Centre Canada and used as received. All solvents used in manipulation of Cu(I) compounds were ACS grade and purified from an MBraun Solvent Purifier System. All other solvents were ACS grade and used as received. Nuclear Magnetic Resonance was done on 300 MHz Avance 3 and 400 MHz Bruker AMX. Thermogravimetric analysis was performed on a TA Instruments Q50 apparatus located in an MBraun Labmaster 130 drybox under a nitrogen atmosphere. IR Spectroscopy was performed on a Varian Scimitar series 1000 FTIR. KBr pellets. N-acetylbenzamide was prepared following literature procedure.[113]

1,3-diisopropyl-imidazolin-2-ylidene copper n-acetylbenzamide (1) A 100mL pressure vessel equipped with a magnetic stir bar was charged with 1,3-diisopropyl-imidazolin-2-ylidene copper hexamethyl disilazide (0.268g, 0.7mmol). 1,3-diisopropyl-imidazolin-2-ylidene copper hexamethyl disilazide was dissolved in 4mL of THF, and a further 20mL of THF was added. A solution of N-acetylbenzamide (0.116g, 0.7mmol) in THF (4mL) was added drop-wise to the pressure vessel with rigorous stirring. The pressure vessel was sealed and the reaction proceeded for 23 h. Volatiles were removed under reduced pressure to afford off-white, solid (0.254g, 0.67mmol, 95%, m.p. 98-102°C). ^{1}H NMR (400 MHz, C_6D_6): δ 8.236 (m, 2H, meta, CHC*H)*, 7.081 (m, 3H, ortho + para, CC*H*CHC*H*), 4.084 (sept, 2H, NC*H*$(CH_3)_2$), 2.966 (s, 3H, OCC*H*$_3$), 2.420 (s, 4H, NC*H*$_2$N), 0.713 (d, 12H, NCH(C*H*$_3$)$_2$). ^{13}C NMR (400 MHz, C_6D_6) δ 199.54 (1C, Cu*C*), 184.25 (1C, O*C*CH_3), 175.90 (1C, O*C*N), 142.50 (1C, OC*C*CH), 129.327 (2C, C*C*HCHCH), 128.68 (2C, CCH*C*HCH), 127.615 (1C, CCHCH*C*H), 51.041 (2C, N*C*H$(CH_3)_2$), 42.056 (2C, N*C*H$_2$), 25.824 (OC*C*H$_3$), 20.773 (4C, NCH(*C*H$_3$)$_2$) IR spectral analysis (KBr pellet): 1727.4 cm^{-1} (C=O), 1680.07 cm^{-1} (C=O (conjugated)).

1,3-diisopropyl-imidazolin-2-ylidene copper diacetamide (2) A 35mL pressure vessel equipped with a magnetic stir bar was charged with 1,3-diisopropyl-imidazolin-2-ylidene copper hexamethyl disilazide (1.053g, 2.78mmol). 1,3-diisopropyl-imidazolin-2-ylidene copper hexamethyl disilazide was dissolved in 20 mL of THF. Diacetamide (0.282g, 2.79mmol) was added portion-wise to the pressure vessel with rigorous stirring. The pressure vessel

was sealed and the reaction proceeded for 2 h. Volatiles were removed under reduced pressure to afford white solid (0.821g, 2.58mmol, 93%, m.p. 64-66ºC). ^{1}H NMR (400 MHz, C_6D_6): δ 4.341 (m, 2H, sept, NC*H*$(CH_3)_2$*)*, 2.629 (s, 6H,OCC*H*$_3$), 2.521 (s, 4H, NC*H*$_2$C*H*$_2$N), 0.828 (d, 12H, NCH(C*H*$_3$)$_2$). ^{13}C NMR (400 MHz, C_6D_6): δ 199.37 (1C, N*C*N), 180.54 (2C, N*C*O), 51.00 (2C, N*C*$(CH_3)_2$), 41.99 (2C, N*C*H$_2$*C*H$_2$N), 27.65 (2C, OC*C*H$_3$), 20.48 (4C, NC(*C*H$_3$)$_2$).

1,3-diisopropyl-imidazolin-2-ylidene copper acetylacetonate (3) A 35mL pressure vessel equipped with a magnetic stir bar was charged with 1,3-diisopropyl-imidazolin-2-ylidene copper hexamethyl disilazide (0.614g, 1.62mmol). 1,3-diisopropyl-imidazolin-2-ylidene copper hexamethyl disilazide was dissolved in 25mL of THF. Acetylacetone (0.713g, 7.12mmol) was added portion-wise to the pressure vessel with rigorous stirring. The pressure vessel was sealed and the reaction proceeded for 1 h. Volatiles were removed under reduced pressure to afford green solid (0.388g, 1.22mmol, 75%, m.p. 60 – 62ºC). ^{1}H NMR (400 MHz, C_6D_6): δ 5.544 (s, 1H, OCHC*H*CHO) 4.514 (sept, 2H,NC*H*), 2.594 (s, 4H, NC*H*$_2$C*H*$_2$N), 2.091 (s, 6H, OCHC*H*$_3$), 0.884 (d, 12H, NCH(C*H*$_3$)$_2$). ^{13}C NMR (400 MHz, C_6D_6): δ 189.04 (1C, N*C*N), 99.12 (1C, OC*C*CO), 50.80 (2C, N*C*H$(CH_3)_2$), 41.85 (2C, N*C*H$_2$*C*H$_2$N), 28.28 (2C, OC*C*H$_3$), 20.43 (4C, NC(*C*H$_3$)$_2$).

5.5 Conclusions

Three novel copper(I) compounds were synthesized from 1,3-diisopropyl-imidazolin-2-ylidene copper hexamethyl disilazide and characterized by thermogravimetric analysis to determine their suitability as volatile copper CVD precursors. The reactivity of 1,3-diisopropyl-imidazolin-2-ylidene copper hexamethyl disilazide was tested and since it is a strong base that will readily react with even weak acids, the displacement of the hexamethyldisilizide moiety occurred readily, under mild conditions. This reactivity can be exploited further, by employing other inexpensive, readily available reagents to form new and interesting copper compounds. Compounds **1**, **2** and **3** all exhibited volatility, although each had some level of decomposition as well. However, they still hold promise for future CVD experiments.

Chapter 6 – Preventing Thermolysis: Precursor Design for Volatile Copper Compounds

Please see preface, page 4, for more details and full article citation. Author contributions listed below are paraphrased from signed Letters of Permission to reprint this material.

Agnieszka Kurek is second author of this research paper. Her contributions to this published work included a thermolysis study of a copper compound, data interpretation, some writing, and editing.

Jason Coyle contributed synthesis of compounds, thermogravimetric analysis of compounds and interpretation of results.

Peter Pallister used solid-state and high-resolution NMR as well as elemental analysis to deduce a mechanism for chemisorption of one copper species on the surface of high surface area silicon. He also contributed writing and editing.

Eric Sirianni and Glenn Yap contributed crystal structure collection and data interpretation.

Sean Barry contributed data interpretation, writing and editing.

6.1 Abstract

A copper(I) iminopyrrolidinate was synthesized and evaluated by thermal gravimetric analysis (TGA), solution based ^{1}H NMR studies and surface chemistry to determine its thermal stability and decomposition mechanism. Copper(I) tert-butyl-imino-2,2-dimethylpyrrolidinate **(1)** demonstrated superior thermal stability and showed negligible decomposition in TGA experiments up to 300°C as well as no decomposition in solutions at 165°C over three weeks.

6.2 Introduction

Atomic layer deposition (ALD) is a deposition process that relies on successive self-limiting reactions between an entrained precursor gas and a solid substrate.[114,115] Progress in ALD has relied on novel precursor chemistry to allow processes for thin film deposition to be defined for a variety of target films and process conditions. In many cases, the “design” of the precursor entails selecting a new ligand and modifying it to provide volatility and thermal stability to a precursor. However, such ligands are often not tested and redesigned to improve on their original performance. More often, a new ligand is employed to overcome the failings of a previous ligand.

There have been several designs for precursors for the deposition of copper metal, a key element in the fabrication of microelectronic circuits.[116,117] One influential ligand used in copper ALD is the amidinate family, which includes both amidinates and guanidinates,[118] including copper(I) alkylamidinates[119] and copper(I) guanidinates[120] (Figure 6.2.1). These ligands suffer from two main thermal decomposition pathways: loss of carbodiimide (herein called

"deinsertion") and β-hydrogen abstraction.[10] These low temperature decompositions lead to the formation of copper metal, with the ligand acting as a reducing agent.

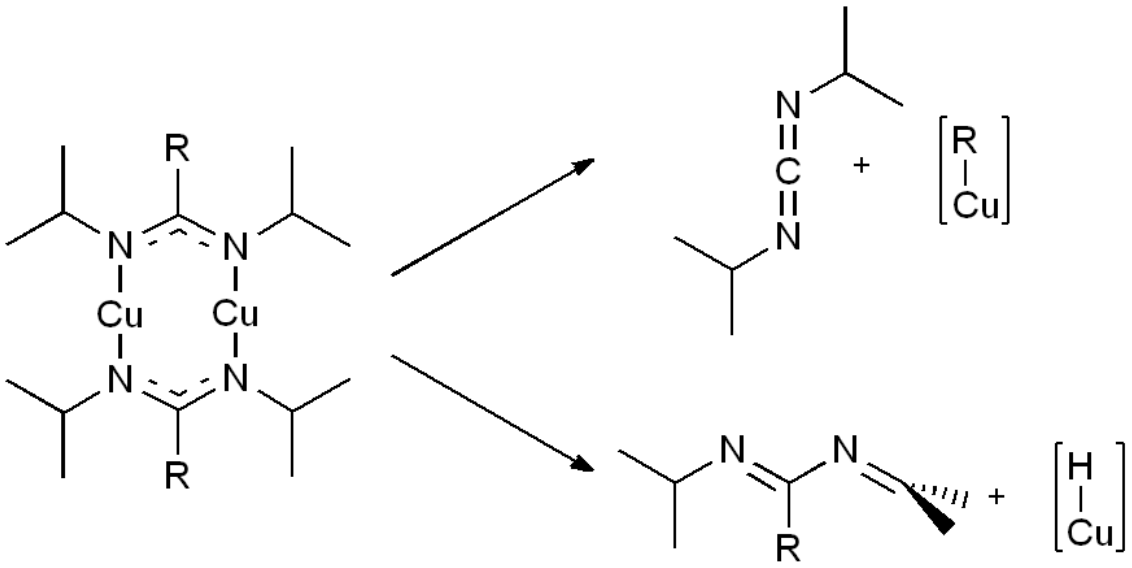

Figure 6.2.1: Thermal decomposition pathways for copper(I) amidinates, where R can be an alkyl or an amine.

6.3 Results and Discussion

The redesign of the amidinate ligand was undertaken to prevent these thermolyses. By using a judiciously chosen pyrrolidinate, both thermal pathways could be eliminated (Figure 6.3.1).

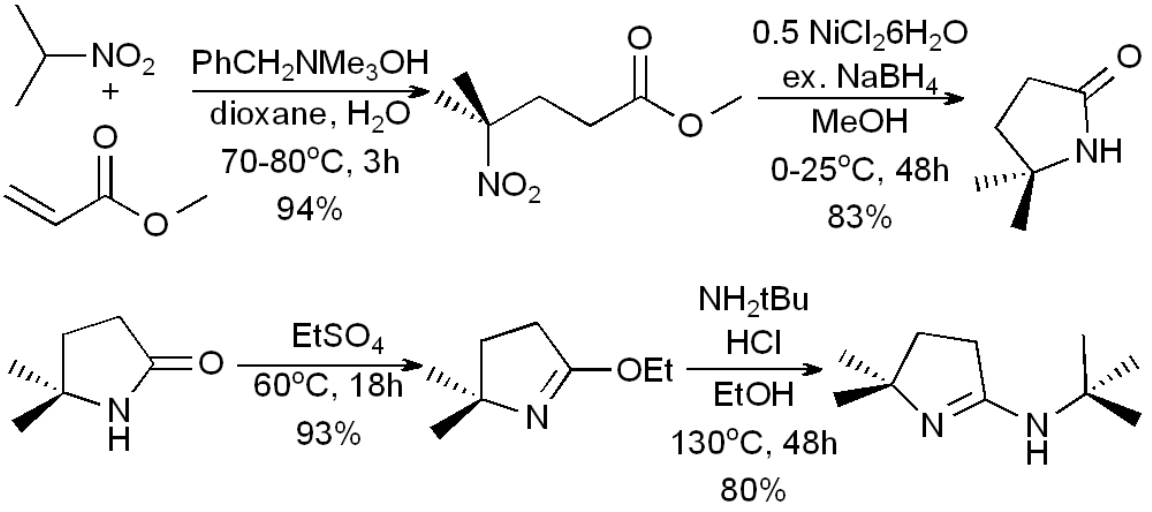

Figure 6.3.1: The synthetic procedure for producing the tert-butyl-imino-2,2-dimethylpyrrolidine ligand.

The deinsertion of carbodiimide (CDI) was prevented by tethering the alkyl group of the chelate position to the exocyclic group through use of a pyrrole ring. β-hydrogen abstraction was eliminated by using a tert-butyl group in the chelate position as well as replacing the β-hydrogens on the ring with methyl groups. The ligand was made in high yield, and the copper(I) pyrrolidinate **1** was formed through simple salt methathesis. Recently, trimeric heteroleptic copper(I) guanidinates were isolated from the attempted synthesis of $[Me_2NC(N^tBu)_2Cu]_2$.[121] Compared to this trimer, the ring of the iminopyrrolidinate reduced the steric bulk to permit the isolation of **1** as the more typical dimer, as

seen by single crystal X-ray diffraction. The structure of **1** is consistent with previously known amidinate[119] and guanidinate[120] systems (Figure 6.3.2, Table 6.3.1). The compound has a Cu-Cu distance of ~ 2.5Å, with an approximately linear coordination geometry around each copper atom. The metallocycle core is planar with equivalent N-C bonds (1.34Å) suggesting delocalization.

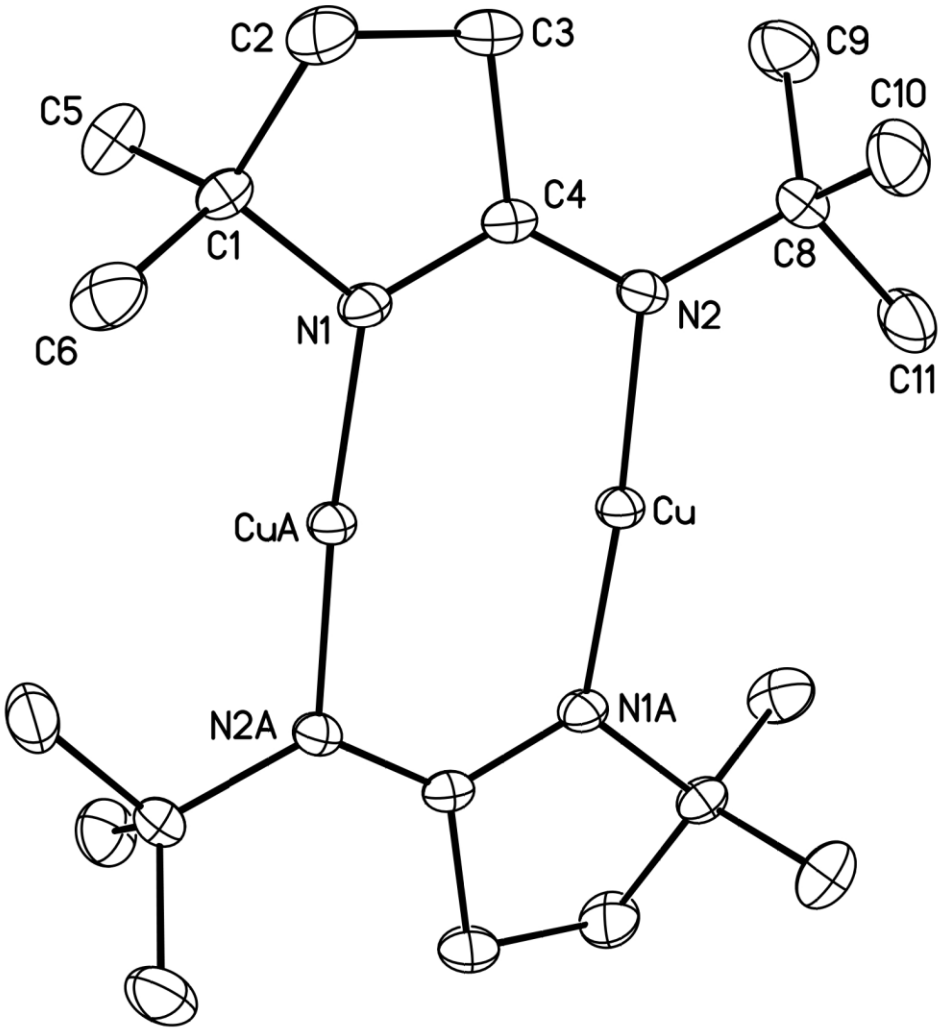

Figure 6.3.2: The structure of **1,** with hydrogens removed for clarity, and the thermal ellipsoids shown at 30%.

This compound showed excellent volatility: thermogravimetric analysis (TGA) showed it to be volatile as low as 165°C at atmospheric pressure, with a residual mass of <2% of the sample mass. Compound **1** could also be quantitatively sublimed at 130°C at a pressure of 20mTorr. This indicated that the compound cleanly volatilizes at these temperatures with no thermal decomposition.

Table 6.3.1: Selected Bond Lengths and Angles for 1

Selected Bond Lengths (Å)	
Cu-Cu	2.47
Cu-N1	1.87
Cu-N2	1.89
N1-C4	1.33
N2-C4	1.33
Selected Angles (°)	
N1-Cu-N2	175.6
N1-C4-N2	122.5

More importantly, a thermal stress test designed for this study showed **1** to be very resistant to thermal decomposition at higher temperatures. In this stress test, the compound is measured by TGA using the same temperature ramp rate (10°C/min) but with different sample masses (Figure 6.3.3). Due to the kinetics of volatilization, as sample mass is increased, more sample becomes exposed to higher temperatures. This valuable test can be used to gauge the behaviour of a compound with respect to thermal handling during a deposition process. As seen in Figure 6.3.3, varying the sample weights of **1** gave no deviation in residual mass, whereas performing the same stress test on the similar

diisopropylguanidinatocopper[120] compound **2** showed a marked increase of residual mass of <2.0 – 9.0% of the initial mass as the sample mass was increased from 10mg to 63mg. It has been previously demonstrated that **2** undergoes CDI deinsertion at lower temperatures, a process which has been prevented through this ligand design.[10]

This contrast in thermal behaviour was highlighted by the decomposition kinetics of these two compounds at 165°C. Compound **2** was found to decompose following first order decomposition kinetics with a calculated half-life of 33.8 hours while **1** showed no appreciable decomposition over 20 days at 165°C.

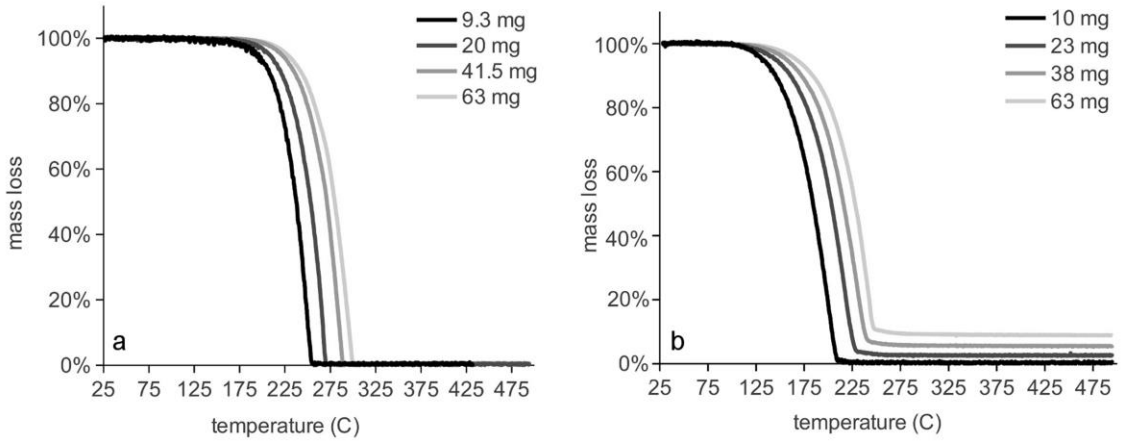

Figure 6.3.3: Thermal stress test of compounds a) 1 and b) 2, showing effect on residual mass as starting mass was increased.

To test compound **1** for vapour phase stability, it was heated in a bubbler at 160°C and the evolved vapour was entrained over high surface area silica for 17 h to saturate the silica with a chemisorbed monolayer. Characterization was undertaken using $^{1}H/^{13}C$ cross-polarized magic-angle spinning solid state NMR,

and there was only physisorbed species detected up to 200°C. At a deposition temperature of 275°C, solid-state ^{13}C NMR showed signals attributable to the copper precursor (6.3.4a, top trace). These signals were similar to the high resolution ^{13}C NMR of **1** in deuterated benzene (Figure 6.3.4a, bottom trace). There was excellent corroboration between the solution NMR and the solid-state NMR. Although this suggested that the precursor chemisorbed "whole" at the surface, literature suggests that the alkyl group at the chelate position might be lost at high temperatures.[121] The line width of the solid-state NMR did not permit unambiguous identification of the tert-butyl moiety, so another experiment was needed. The silica with the deposited monolayer was rinsed with D_2O to etch off the surface species, and a high resolution ^{1}H NMR was collected (Figure 6.3.4b, top trace), showing a singular surface species. Although the chemical shifts were different because of the necessity of using different solvents, the integration of the peaks for the surface species showed loss of the tert-butyl group: integrations of 2.1, 2.0, and 5.7 for the peaks at 2.94ppm, 2.07ppm, and 1.36ppm respectively. The ^{1}H NMR of the ligand in deuterated chloroform clearly showed a singlet for the tert-butyl group (6.3.4b, bottom trace) with integration ratios of 2.0, 2.0, 9.4, and 6.1 for the peaks at 2.42ppm, 1.57ppm, 1.32ppm, and 1.18ppm respectively. As well, ^{29}Si SS-NMR of the silica showed no additional signals for silicon beyond what was detected for pure silica, suggesting nucleation did not occur at a silicon atom. This is reasonable, considering that the most likely nucleation point for this precursor on silica surface is at the oxygen of a silanol group. Given these data, nucleation likely occurs through the copper atom to a

surface oxygen, and subsequently undergoes butene elimination (Figure 6.3.4c). This elimination occurs at 300°C higher in temperature than shown for the copper amidinate,[122] and highlights the excellent thermal stability designed into this ligand.

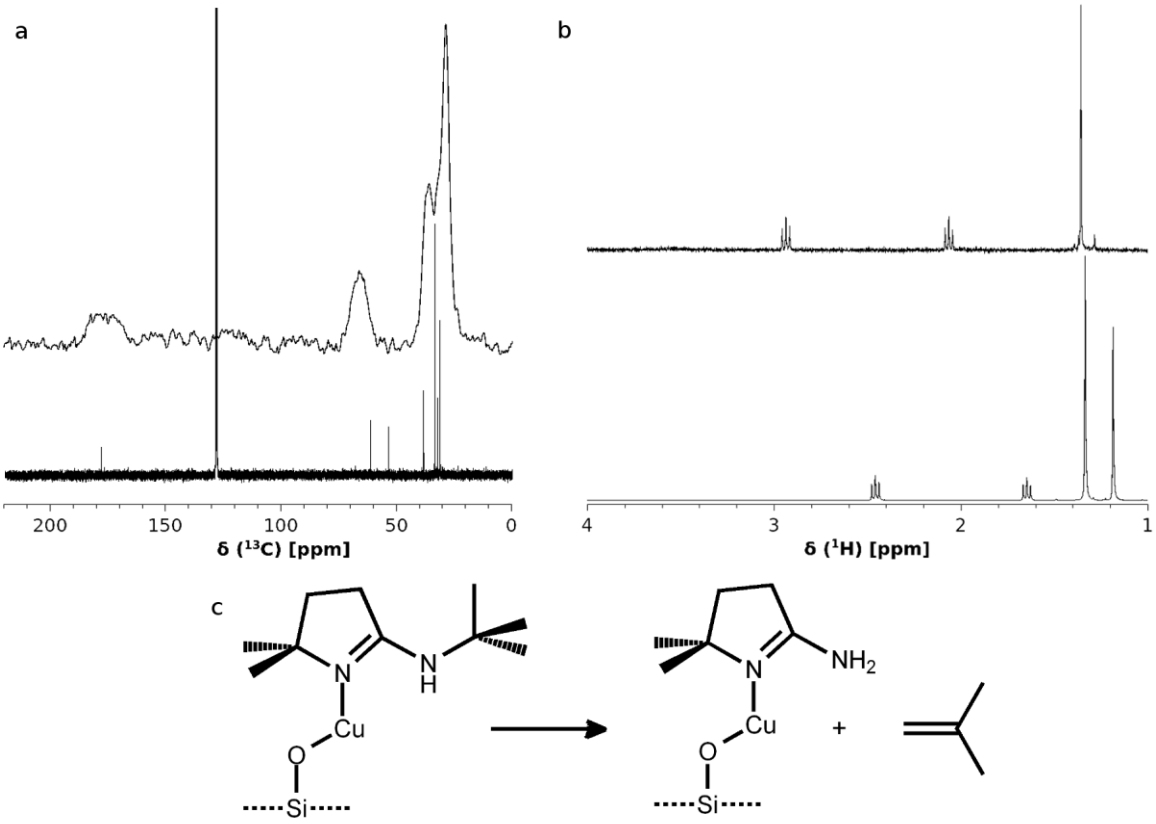

Figure 6.3.4: Reactivity of **1** with silica: a) shows the SS-^{13}C NMR of silica after deposition of **1** at 275°C (top trace) compared to the HR-^{13}C NMR of **1** in deuterated benzene (bottom trace). b) shows the HR-^{1}H NMR of the surface species etched from the silica with D_2O (in D_2O; top trace) compared to the HR-^{1}H NMR of **1** in $CDCl_3$ (bottom trace). c) shows the proposed nucleation and chemisorption of **1** at a silanol group on a silica surface.

6.4 Conclusions

In summary, a new volatile precursor for copper metal deposition was synthesized with its ligand designed to prevent two known, low temperature decomposition pathways. The precursor **1** showed excellent stability both in the solid state, in solution, and as a vapour species. Surface analysis suggested that the precursor undergoes an alkene elimination from the chelating nitrogen atom during chemisorption on silica at 275°C. This novel precursor suggests that a family of iminopyrrolidinates of copper might be synthesized with various β-hydrogen atoms, which would allow tuning of the precursors thermal reactivity.

Chapter 7 – Copper Iminopyrrolidinates: A Study of Thermal and Surface Chemistry

Please see preface, page 4, for more details and full article citation. Author contributions listed below are paraphrased from signed Letters of Permission to reprint this material.

Agnieszka Kurek is third author of this research paper. Her contributions to this published work included a thermolysis study of four copper compounds, data interpretation, some writing, editing and figure composition. Please see preface, page 4, for more details and full article citation.

Jason Coyle contributed synthesis of compounds, thermogravimetric analysis of compounds and interpretation of results.

Peter Pallister used solid-state and high-resolution NMR as well as elemental analysis to deduce a mechanism for chemisorption of one copper species on the surface of high surface area silicon. He also contributed writing and editing.

Eric Sirianni and Glenn Yap contributed crystal structure collection and data interpretation.

Sean Barry contributed data interpretation, writing and editing.

7.1 Abstract

Several copper(I) iminopyrrolidinates have been evaluated by thermogravimetric analysis (TGA) and solution based ^{1}H NMR studies to determine their thermal stability and decomposition mechanisms. Iminopyrrolidinates were used as a ligand for copper(I) to block previously identified decomposition routes of carbodiimide (CDI) deinsertion and β-hydrogen abstraction. The compounds copper(I) isopropyl-iminopyrrolidinate **(1)**, and copper(I) tert-butyl-iminopyrrolidinate **(2)**, were synthesized for this study, and compared to the previously reported copper(I) tert-butyl-imino-2,2-dimethylpyrrolidinate **(3)**, and the copper(I) guanidinate $[Me_2NC(^{i}PrN)_2Cu]_2$ **(4)**. Compounds **1** and **2** were found to be volatile yet susceptible to decomposition during TGA. At 165°C in C_6D_6, they had half-lives of 181.7 h and 23.7 h, respectively. The main thermolysis product of **1** and **2** was their respective protonated iminopyrrolidine ligand. β-hydrogen abstraction was proposed for the mechanism of thermal decomposition. Since compound **3** showed no thermolysis at 165°C, it was further studied by chemisorption on high surface area silica. It was found to eliminate isobutene upon chemisoption at 275°C. Annealing the sample at 350°C showed further evidence of the decomposition of the surface species, likely eliminating ethene, and producing a surface bound methylene diamine.

7.2 Introduction

Copper metal remains an interesting topic for chemical vapour deposition (CVD) and atomic layer deposition (ALD) due to its use in microelectronics,

primarily as an interconnect material.[55] One class of particularly well-studied precursors are amidinates, which originated from the Gordon group in the early 2000s.[119,123] Copper amidinates have utility in ALD[119] and CVD[124] processes between temperatures of 150 – 240°C when using hydrogen as a reducing agent. Copper(I)-N,N'-di-isopropylacetamidinate has been shown to undergo CVD deposition as low as 140°C,[122,125] and produces free amidine, acetonitrile, propene and iminopropane when allowed to thermally decompose in the absence of a reducing agent.[126] These findings have been corroborated in the surface study work of copper(I) acetamidinates on nickel where, above 130°C, the self-limiting nature of the monolayer is compromised and continuous uptake of the copper precursor is observed. Similar ligand fragments were identifed in the surface work as in the gas phase work.

We have previously investigated the thermal decomposition of copper (I) guanidinates, which are similar to amidinates except that the exocyclic group is an amide, rather than an alkyl.[10,120] Using a guanidinate with isopropyl groups on the chelating nitrogens, we found two distinct thermal decomposition mechanisms (Figure 7.2.1). In solution at lower temperatures, the guanidinate deinserted carbodiimide (CDI) and produced the parent amine of the exocyclic amide group.[120] In the gas phase at greater than 150°C, the methylene carbon of the isopropyl group on the chelating nitrogen loses a hydrogen and produces an oxidized guanidine. Hydrogen gas is also found as a thermolysis side product.[10]

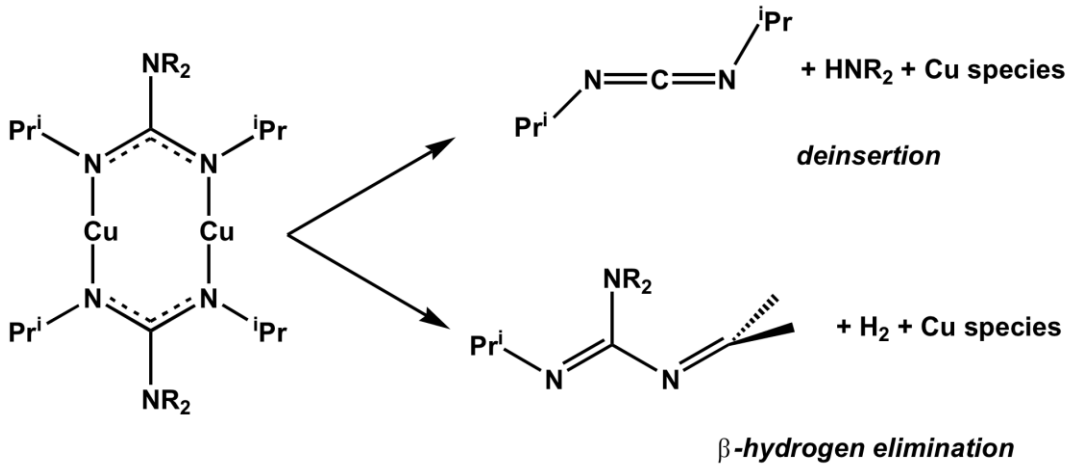

Figure 7.2.1: Two thermal decomposition pathways for a copper(I) guanidinate species.

Both of these thermal decomposition mechanisms are troubling from the point of view of developing a copper precursor for ALD. In the first case, the elimination of the oxidized guanidinate by β-hydrogen abstraction produces a copper hydride, which readily eliminates dihydrogen or parent guanidine to produce copper metal. This circumscribes an ALD process in favour of a CVD process. CDI deinsertion also greatly limits the use of this precursor in thermal processes. The formation of a transient copper-amide bond creates a species that will readily decompose,[127] thus also preventing ALD in favour of a CVD process.

A re-design of the basic amidinate framework is necessary to remove the known thermal decomposition pathways of this ligand family. Our group has developed and extensively characterized a novel iminopyrrolidinate ligand family that has evidenced good thermal stability. Recently, we have reported a family of

volatile, stable aluminum compounds.[128] This ligand has a five-membered ring linking one chelate nitrogen to the “bridgehead” (i.e., quaternary) carbon of the amidinate, thus preventing CDI deinsertion. Likewise, the ligand has been synthesized to allow control over the number of β-hydrogens, resulting in a series of four related copper(I) iminopyrrolidinates (Figure 7.2.2).

Herein we introduce two novel copper iminopyrrolidinates (copper(I) isopropyl-iminopyrrolidinate **(1)**, and copper(I) tert-butyl-iminopyrrolidinate **(2)**, to complement our previously reported[129] copper(I) tert-butyl-imino-2,2-dimethylpyrrolidinate **(3)** and copper (I) N',N”-diisopropyl-N,N-dimethyl guanidinate **(4)**. A thorough exploration of the thermal chemistry of these four compounds was made to demonstrate how the redesign of this ligand has influenced thermal behaviour. We have investigated the thermal stability of this series in the solid phase using a variety of thermogravimetric (TG) methods, as well as in solution phase using high resolution ^{1}H NMR of sealed tubes that have been treated at elevated temperatures to study decomposition kinetics. Finally, due to the superior thermal stability of **3**, we have undertaken an extensive study of the nature of the chemisorbed species produced on silica by **3** as deposited at 275°C and when annealed at 350°C.

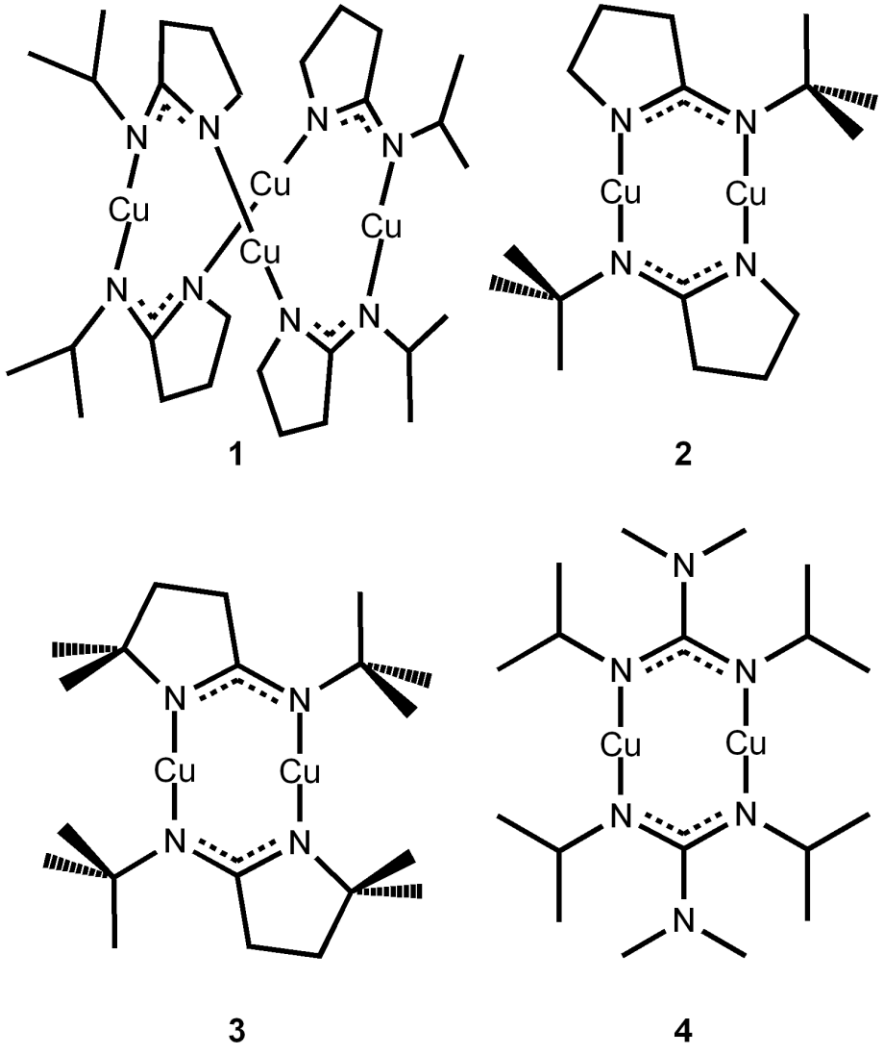

Figure 7.2.2: A series of amidinate-type ligands with differing numbers of ß-hydrogens, shown as their corresponding copper(I) compounds.

7.3 Results and Discussion

The copper compounds **1** and **2** were simply made by salt metathesis of copper(I) chloride with the *in-situ* generated lithium iminopyrrolidinates. These compounds were isolated as white crystalline materials in moderate to high yields. Similarly, a recent paper describes trimeric, heteroleptic copper(I) guanidinates isolated from the attempted synthesis of $[Me_2NC(N^tBu)_2Cu]_2$.[121] We believe the ring of the iminopyrrolidinates reported herein was necessary to slightly reduce the steric bulk and permit the isolation of **2** as a dimeric species (Figure 7.3.1b).

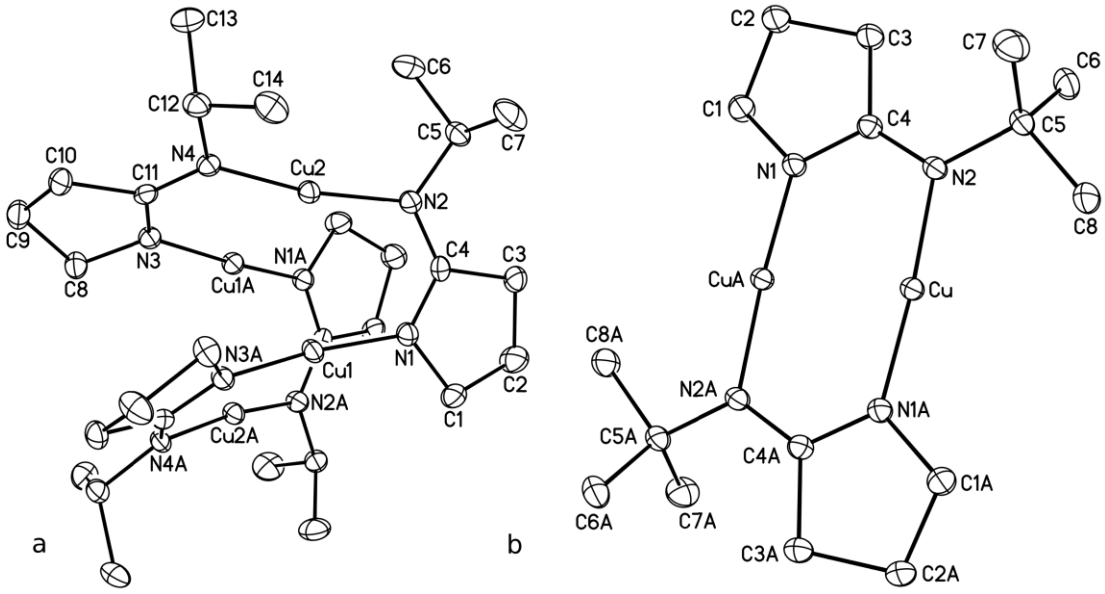

Figure 7.3.1: The structure of a) **1** and b) **2**, shown with the hydrogens removed for clarity. The thermal ellipsoids are at 30%.

The ^{1}H NMR of **2** was simple, suggesting a symmetrical oligomeric solution structure, similar to known copper guanidinate dimers.[120] However, compound **1** showed a more complex ^{1}H NMR. The doublets for the methyls of the isopropyl moiety in **1** suggested several environments. It is unclear if these multiple environments were due to an equilibrium of oligomers or from asymmetry in the molecule, but the relative integrations of these doublets were dependent on the concentration of **1**. Serial dilution of an NMR sample nor heating of the sample to 60°C did not yield a trivial set of peaks similar to the spectra of **2**. The data from the ^{1}H NMR suggest that the species might be in an oligomeric equilibrium where the exterior proton environments are disordered in the structure, while the interior ring protons are more ordered. Fortunately, **1** could be isolated as X-ray quality crystals (Figure 7.3.1a). The structure of **1** shows a tetrameric arrangement in the solid state with an orthorhombic C_{cca} space group (Figure 7.3.1a, Table 7.3.1). There are 16 tetramers in the unit cell, but only two that are crystallographically distinct. These molecules each have a core of four copper atoms that lay in a rhombohedral plane, with the rhombus of one molecule centred perpendicular to a C2 axis (with a minor torsion angle of 1.31°), and the other parallel to a different C2 axis (with a torsion angle of 0°). The closest Cu-Cu contact in the unit cell is 2.76Å, which suggest there are no significant Cu-Cu interactions.[130] This is supported by the fact that the N-Cu-N bonds only deviate from linearity by about 10°, which is likely caused by steric hindrance in the ligands (Table 7.3.1). Since the connectivity of the molecules in the unit cell is very similar, only one molecule will be discussed in depth.

Interestingly, the two ligands bonded to any specific copper are bonded through the same type of nitrogen. For example Cu1 is bonded to the ring nitrogens N1 and N3, where one might expect the ligands to alternate. Additionally, the isopropyl groups of the ligand are all oriented towards the copper plane. These observations suggest that there is a fine balance of steric interference across the copper plane allowing a tetramer to form. This structure type has been seen previously for group 11.[131–133] The Cu-N bonds in this molecule have an average length of 1.88Å, which is the same as in **3**.[129]

Table 7.3.1. Selected Bond Lengths and Angles for 1 and 2			
Compound **1**		Compound **2**	
Selected Bond Lengths (Å)			
Cu1-Cu2	2.76	Cu-Cu	2.48
Cu1-Cu1a	3.00	Cu-N1	1.86
Cu1-N1	1.87	Cu-N2	1.89
Cu1-N3	1.86	N1-C4	1.34
Cu2-N2	1.89	N2-C4	1.33
Cu2-N4	1.89		
N1-C4	1.31		
N2-C4	1.34		
N3-C11	1.31		
N4-C11	1.33		
N1-C1	1.44		
N2-C5	1.46		
N3-C8	1.46		
N4-C12	1.49		
Selected Angles (°)			
Cu2-Cu1-Cu2	114.2	N1-Cu-N2	175.3
Cu2-Cu1-Cu1	57.1	N1-C4-N2	122.1
N3-Cu1-N1	170.5		
N2-Cu2-N4	170.7		
N1-C4-N2	123.8		
N3-C11-N4	123.6		

Considering the ligands oriented parallel to each other and on the same side of the copper plane, it is obvious that more crowding exists here. The ligands bend out slightly from one another, on average 26.5° from parallel. As well, there is a slight twist of about 6° across each ligand with respect to the line defined by the coppers which bind them.

The metallocycle C-N bonds are all about equivalent in this molecule (1.31 – 1.34Å), suggesting complete delocalization of the double bond, similar to **3**. The bridging angle of the ligand (N-C-N) is about 123°, which is slightly larger than **3** and **4**.[120] This is quite understandable in the case of the tetramer, however, since the ligand is bridging a significantly large Cu-Cu distance.

The structure of **2** is more typical of the expected dimeric structures, considering **3** and **4** (Figure 7.3.1b, Table 7.3.1). It crystallized in the monoclinic $P2_{1/c}$ space group with two molecules in the unit cell centered on inversion centres, where both molecules in the unit cell are identical. The Cu-Cu distance is ~ 2.5Å, which is significantly closer than in **1**. The copper geometry is linear, contorting by only 4.7° to lengthen the Cu-Cu bond. The metallocycle core is planar with the core N-C bonds all essentially equivalent (1.33 – 1.34Å), suggesting that the inherent double bond character is delocalized between these two bonds.

The thermolyses of **1** and **2** are quite encouraging. Compound **1** showed low residual mass using thermogravimetric (TG) analysis, and a single feature in weight loss, suggesting that the species volatilized easily. This low residual mass

was surprising. Not only does this compound possess β-hydrogen atoms for abstraction, but also the tetrameric structure was expected to yield a lower vapour pressure from increased molecular mass. It is possible that there exists an oligomeric equilibrium that allows **1** to volatilize as a lower order oligomer (mass spectral analysis shows a dimer), thus providing a larger vapour pressure at lower temperature. This also explains why **1** has a similar onset of volatilization to the dimeric compounds **3** and **4**.

Compound **2** showed more complex behaviour. The residual mass was 28.1%, which was close to the percent mass of copper (31.3%) in this compound. The residual mass was confirmed to be metallic copper by powder X-ray diffraction, suggesting that **2** undergoes a low temperature reduction to produce Cu(0). This has previously been observed in the case of both **4** and the copper amidinates.[122,125] Due to the presence of the exocyclic pyrrolidine ring, the more favourable path for this thermal decomposition is β-hydrogen elimination rather than CDI deinsertion. This can be rationalized considering the crystal structure of **2**. The distortion of the dimer core and lack of steric protection exposes the copper and enables it to interact with the β-hydrogen atoms of neighbouring molecules.

These compounds were also investigated by a thermal stress test using TG analysis. Essentially, a compound is measured using the same temperature ramp rate (10°C/min) but using different sample masses. Thus, more quantity of sample would be exposed to higher temperatures due to the kinetics of

thermolysis or volatilization. This valuable test can be used to gauge the behaviour of the compound with respect to thermal handling during a deposition process, whether in the source bubbler or during the volatilization and entrainment to the deposition zone. A good example of this is the thermal stress test of **1 (**Figure 7.3.2). Compound **1** was shown to have a higher residual mass as the initial pan loading of the TG was increased. This indicated that it underwent decomposition as more compound was exposed to higher temperature. Compound **3** (Figure 7.3.2) was seen to undergo no decomposition as pan loading was increased, demonstrating a superior thermal stability.

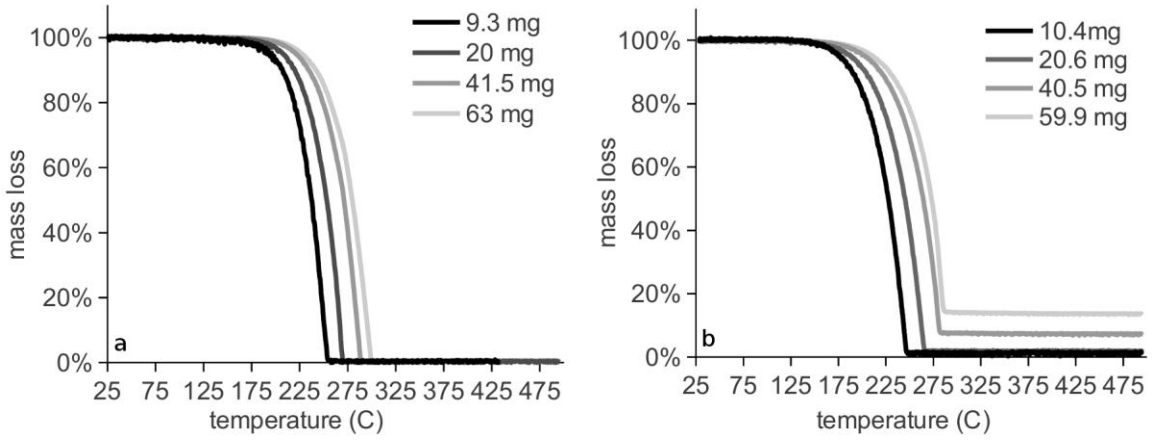

Figure 7.3.2: Thermal stress test of compounds **3** showing no change in residual mass with increasing sample mass (left), and **1** showing increasing residual mass with increasing initial sample mass (right).

The residual mass trends of each compound **1** – **4** can be seen in Figure 7.3.4. It should be noted that the top sample mass that could be accommodated was about 65mg; this filled the sample pan in all cases. With the exception of **1**, the stress trends are quite linear with an R^2 of 0.99. Compound **1** showed a higher deviation from linearity with an R^2 of 0.97. This might be due to a higher preponderance of a dimeric rather than tetrameric species at higher temperature, caused by a shift in oligomer equilibrium.

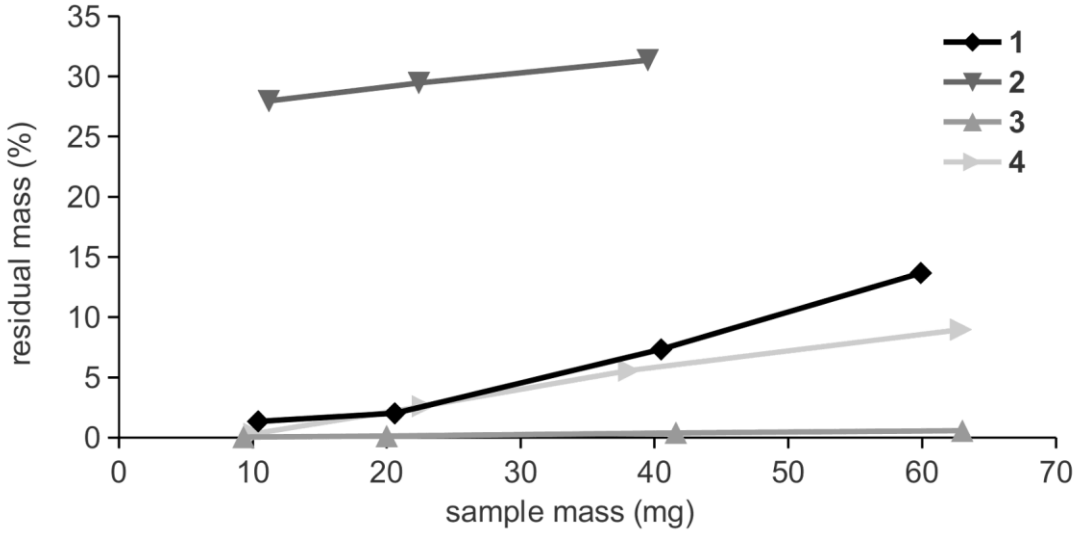

Figure 7.3.3: Thermal stress test trends for compounds **1** – **4**.

Compounds **1** and **4** show the most stress, deviating from a negligible residual mass at low loadings to quite high residual masses (13.7% for **1** and 9.0% for **4**) at high loadings. It is not surprising that these two compounds show similar thermal stress, since they both bear an isopropyl group for β-hydrogen elimination although CDI deinsertion cannot be ruled out in the case of **4**.

Compound **2** again showed poor thermal behaviour with very high residual masses. Indeed, the highest loading was not attempted for **2** since the 39.5mg of sample gave 31.35%, which is the mass percent of copper in that compound (31.32%). This was not surprising, given the high residual mass seen previously. This reactivity stands out due to the fact that **2** can be considered of intermediate reactivity with respect to number of β-hydrogens within this family. However, it has a dimeric structure (unlike **1**, which exists in the solid as a tetramer) and so is less sterically protected at the copper centres. This would lend it worse thermal stability.

Compound **3** showed very good thermal stress resistance, rising only to 0.56% residual mass at 63.0mg sample mass. This supports our hypothesis that **3** will be the most thermally stable of this series of compounds due to its lack of reactive hydrogens and the robust nature of the core of this ligand with respect to CDI deinsertion.

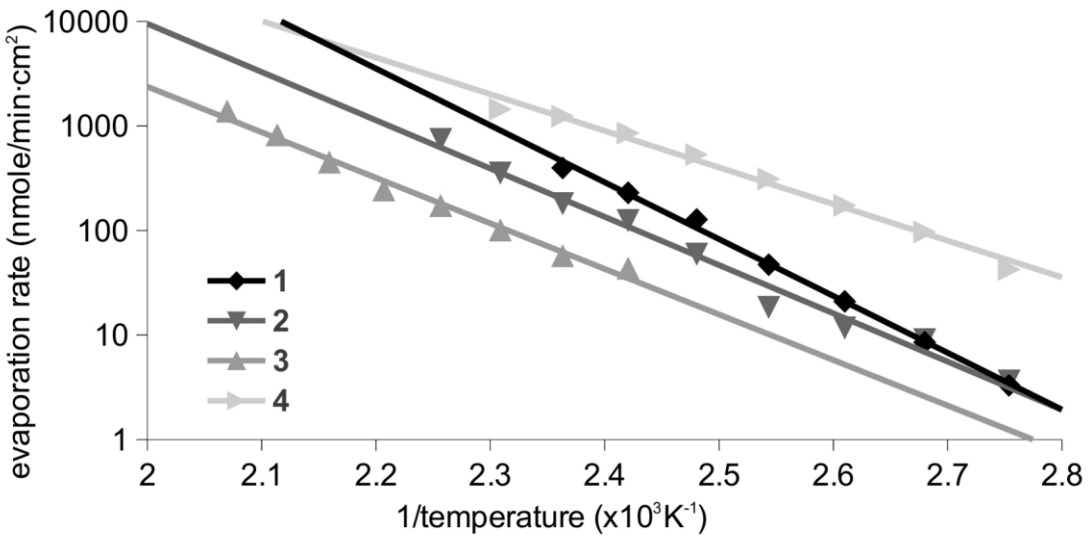

Figure 7.3.4: Evaporation kinetics of **1** – **4** by TG analysis.

The evaporation kinetics were evaluated by TG analysis for **1** – **4** (Figure 7.3.4). Compound **4** showed the highest evaporation rate at the lowest temperatures. Compounds **1** and **2** showed similar evaporation kinetics within the temperatures studied. This is unsurprising since **1** and **2** are expected to both volatilize as dimers and have similar molecular masses – a mass difference of only two methyl groups. Surprisingly, **3** showed the slowest evaporation kinetics even though it has a mass close to that of **4**. It is possible that the measured evaporation kinetics of the copper(I) iminopyrrolidinates are slower than **4** due to the more rigid framework of the iminopyrrolidinate ligand. The rigidity of the ligand would cause a compact, planar structure and allow for stronger intermolecular attraction within the solid. Additionally, the copper(I) iminopyrrolidinates would be expected to have less entropy gain during volatilization than **4**: the rigid ligand has fewer bonds that are free to rotate in the

gas phase than in the solid state, compared to the relatively less constrained guanidinate of **4**. From the isothermal TG analysis and using the Langmuir equation,[134] the temperatures at which 1Torr of vapour pressure was obtained were estimated to be 158°C, 161°C, 187°C, and 125°C for **1** – **4**, respectively.

To further illuminate the thermal chemistry of these compounds, they were each sealed in heavy-walled NMR tubes and heated in an oven at 165°C over a period of days. A ^{1}H NMR spectrum was collected each day to observe their thermal decomposition (Figure 7.3.5, Table 7.3.2). Compound **4** revealed decomposition to produce diisopropylcarbodiimide, as previously seen.[120] The decomposition of **4** followed first order decomposition kinetics and had a calculated half-life of 33.8 h. The parent guanidine was also observed as a product of thermolysis and its origin of production is discussed below.

Compound **1** showed much better thermal behaviour than **4**, as was expected from the TG data. The compound decomposed following first order kinetics with a half-life of 181.1 h, and there was very obvious plating of copper on the NMR tube walls. The main byproduct from the thermolysis was the parent ligand, isopropyliminopyrrolidine. There was no evidence of CDI or any evidence of oxidized ligand. There was an obvious flocculent in the NMR tube after the thermolysis; this might be the oxidized ligand wherein a proton was lost. Compound **2** showed similar decomposition to **1**, but much more quickly ($t_{1/2}$ = 23.7 h). The NMR tube was again obscured with plated Cu(0) and had a flocculent precipitate, and the ^{1}H NMR showed free, protonated ligand. It is

possible that since **1** forms a tetramer, this imparts thermal stability to the compound, perhaps because the tetramer has to dissociate to a smaller oligomer in order to thermalize. This would also account for the relatively poor linear fit to first order kinetics: if the tetramer forms at higher concentration, then there would be a slightly higher rate of decomposition as the overall concentration of **3** dropped and the dimer-tetramer equilibrium began to favour the dimer.

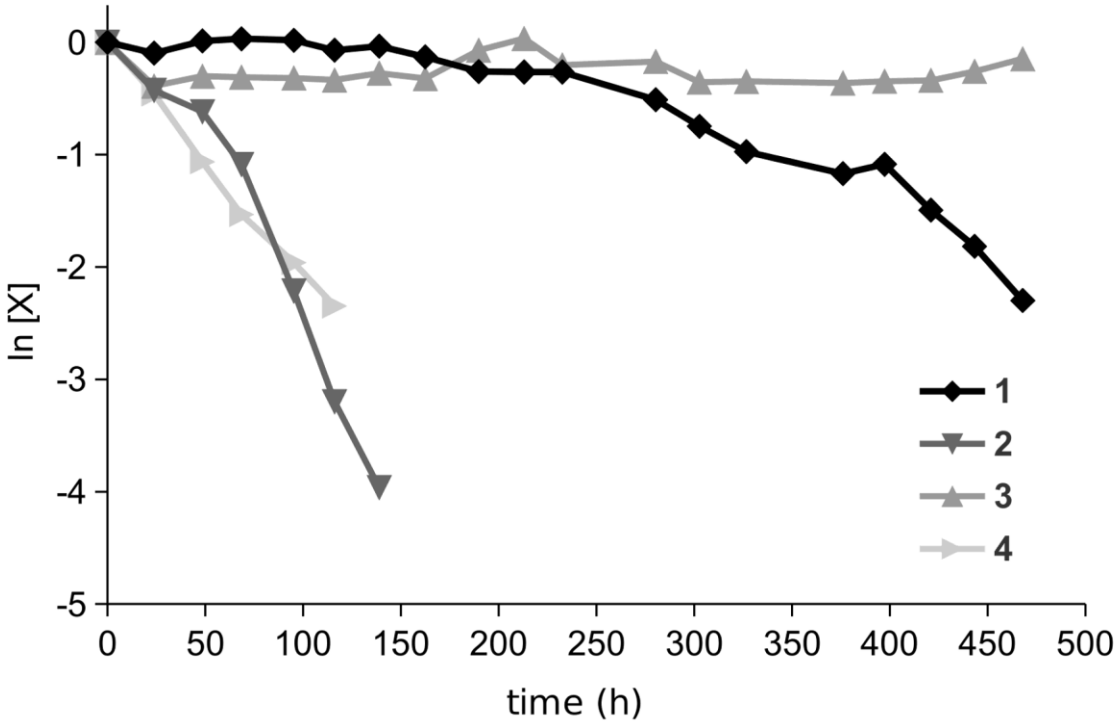

Figure 7.3.5: Thermal decomposition of **1** – **4** at 165°C over 21 days.

Table 7.3.2: Kinetic Data for the Thermal Decomposition of 1 – 4 at 165°C. The "Correlation Coefficient" Refers to the Linear Fit in Figure 7.3.5.

Compound	Rate Constant (s^{-})	Calculated Half- life (h)	Correlation Coefficient
1	1.06×10^{-6}	181.1	0.902
2	8.14×10^{-6}	23.7	0.944
3	No measurable decomposition		
4	5.69×10^{-6}	33.8	0.995

The full mechanism that produces the protonated ligand remains unclear. We propose β-hydrogens as the most likely source for protons for the origin of free ligand. Surface work by Gordon and Zaera[122,125] found that butene elimination occurs from copper(I)-N,N'-di-secbutylacetamidinate leaving an N-H

moiety, which might be another source for protons. However, no ^1H signals were observed in the NMR tube thermolysis experiment that suggest a similar mechanism occurring here. Evidence for disproportionation of Cu(I) acetamidinates has also been demonstrated in surface studies on SiO_2 substrates.[135] Since disproportionation of Cu(I) to Cu(II) and Cu(0) is a common thermolysis route for Cu(I) compounds, we offer the following insight. We observed a blue colour imparted to **2** during the solution based ^1H NMR thermolysis study (Figure 7.3.5), suggesting the formation of a Cu(II) species. Attempts to isolate a Cu(II) compound by crystallization failed and resulted only in the isolation of crystals of **2** with a blue impurity. Interestingly, we previously had prepared oxidized guanidine, i.e. the product of β-hydrogen elimination, from the reaction between guanidine and a Cu(II) compound.[10] Therefore, a Cu(II) intermediate might be involved in β-hydride abstraction thermolysis for this class of compound. We are continuing to study the thermolysis mechanisms of these compounds to gain a fuller understanding of this complicated thermal behavior.

Compound **3** showed no decomposition at 165°C over 21 days. It was expected that its ligand – with no β-hydrogens and without the CDI deinsertion pathway, would impart the best thermal stability, however; this marked difference was surprising. To further explore this, **3** was subjected to a rigorous surface study. This study used a combination of solid-state nuclear magnetic resonance (SS-NMR), elemental analysis, and high-resolution NMR (HR-NMR) to determine the initial monolayer and surface chemistry of **3** on high-surface area silica. SS-

NMR has been shown to be a useful tool in analysis of initial adsorption complexes on high-surface area substrates.[136,137]

Approximately 1g of high surface area silica was loaded into a reactor and annealed under vacuum at 350°C for about 16 h prior to exposure to precursor. This ensured a consistent hydroxyl density at the surface between each experiment. Under these conditions, silica is expected to have a hydroxyl density of 2 – 3.5OH/nm^2.[138] A bubbler temperature of 165°C has been show to produce a sufficient vapour pressure for **3** so this temperature was used for all experiments.[129] A deposition temperature of 200°C was attempted but it was determined that the precursor did not react with the silica. When the silica that was exposed to vaporous **3** was washed with D_2O, only unreacted, dimeric precursor was found at this temperature, suggesting that **3** was simply physisorbed. This was quite interesting, since it demonstrated the stability of **3**: it was stable in aqueous solution for several hours, which was not an anticipated characteristic of this precursor. As well, it existed in a physisorbed state on the silica surface for up to 17 h without decomposing or significantly desorbing.

It was found that a temperature of 275°C was needed to chemisorb **3**. There are three main experiments that will be discussed: Sample **a** is unmodified silica, Sample **b** has undergone chemisorption of **3**, and Sample **c** has undergone chemisorption of **3** with a subsequent anneal at 350°C for 4 h. Energy-dispersive X-ray spectroscopy (EDX) showed the presence of copper on samples **b** and **c**. No copper was detected on sample **a**, as expected.

Interestingly, when **b** was allowed to sit in air, it changed colour to turquoise-green within 15 minutes. This is likely a conversion of the as-deposited surface species to a hydrated copper oxide.

^{1}H/X Cross-polarization magic angle spinning solid-state NMR (CP/MAS SS-NMR) was used as the primary method of characterization for the samples **a** - **c**. The benefit of this technique is that the observed signals originate only from nuclei that are in close proximity to protons; in these samples, this means surface species only. The ^{29}Si CP/MAS SS-NMR spectra of samples **a** – **c** showed typical silica signals (Figure 7.3.6).[139] In **a**, there are signals at around -101.ppm, -110.5 ppm and a shoulder at -92ppm. The signal at -101.6ppm is attributed to silanol groups (‖-Si-OH) at the surface while the signal at -110.5ppm is attributed to fully dehydroxylated silicon near the surface of the bulk sample (‖-Si). The shoulder at -92ppm arises from silandiol species at the surface (‖-Si$(OH)_2$).

The middle trace in Figure 8.3.6 shows the ^{29}Si CP/MAS SS-NMR spectrum for **b**. It is apparent that the only signals present are similar to those of the unmodified silica. Indeed, the lack of other signals demonstrated that chemisorbed precursor interacts with the silica through an oxygen atom, rather than forming direct precursor-silicon bonds. That is, the precursor likely chemisorbs through a ‖-Si-O-Cu interaction, rather than a ‖-Si-Cu or ‖-Si-N. As well, the relative intensities of the various Si species present at the surface differs from that of **a**. The silandiol shoulder vanished in **b**, and the relative intensity of the silanol peak decreased in **b** compared to **a**. Thus, the active surface hydroxyl

groups are being consumed as precursor is taken up by the silica surface. However, the continued presence of a hydroxyl signal showed that saturation has not been reached under these experimental conditions.

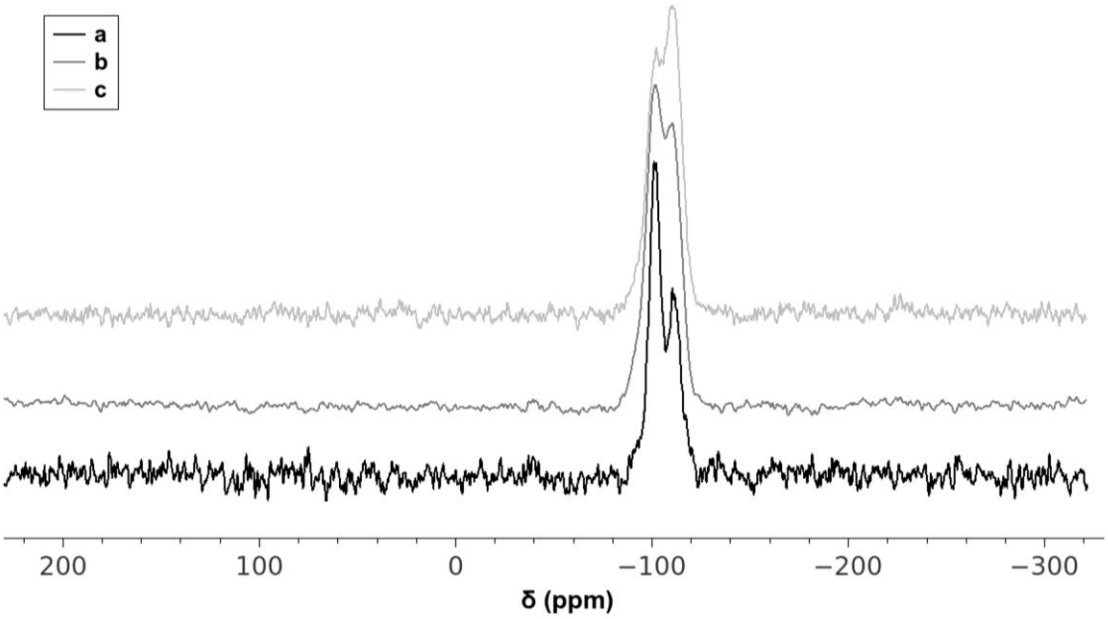

Figure 7.3.6: Solid-state ^{29}Si {^{1}H} CP/MAS NMR of samples **a** - **c**.

The ^{13}C CP/MAS SS-NMR spectra of samples **a** - **c** were diagnostic of the nature of the surface species (Figure 7.3.7). As expected, sample **a** did not show any carbon signals, and highlights the lack of carbon impurities at the silica surface before exposing the system to precursor. The trace for **b** gave four clear signals centered at 28.5, 35.8, 65.9, and 176.5ppm. The signal at 176.5ppm was attributed to the quaternary carbon between the two chelating nitrogens on the iminopyrrolidinate ligand. The broadening of this peak was likely due to the rigidity of the ligand in the chemisorbed surface species. This caused an incomplete averaging of the dipolar and scalar coupling at the 4.5kHz MAS

spinning speed used. The signal at 65.9ppm came from the quaternary carbon in the iminopyrrolidinate ring. The quaternary carbon from the tert-butyl substituent likely contributed to this peak as well. This peak has a similar broadening to the previous peak. The sharp signals 28.5ppm and 35.8ppm were due to the methyl substituents attached to the ring and the methylene carbons that are part of the ring in the iminopyrrolidinate ligand respectively. The methyl groups on the tert-butyl substituent would appear in the same range as these peaks and so was likely buried therein. The assignment of these peaks agreed with the ^{13}C HR-NMR reported for the pure compound **3**.[129]

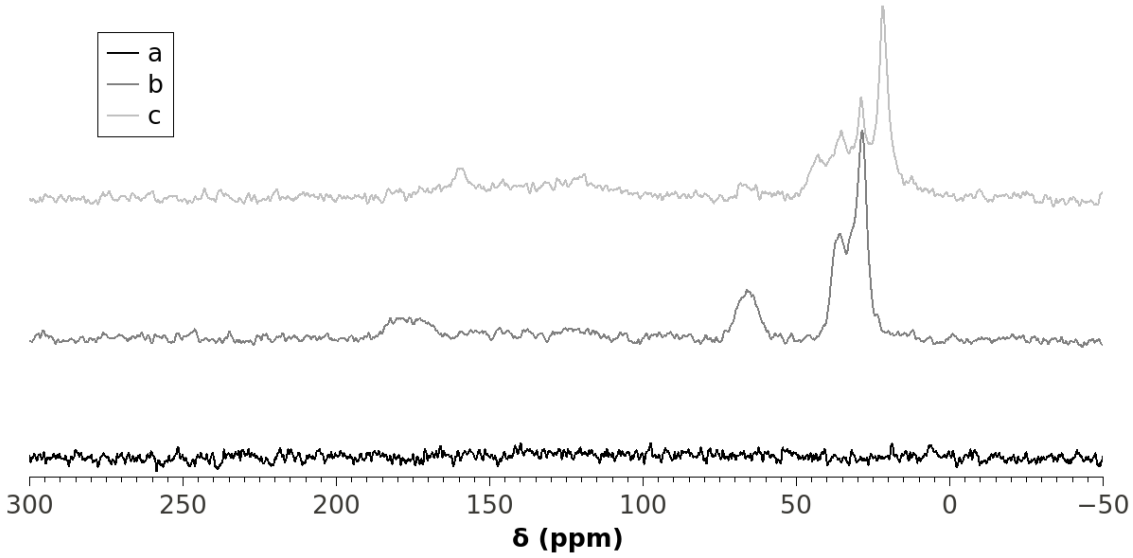

Figure 7.3.7: Solid-State ^{13}C {^{1}H} CP/MAS NMR of high surface area silica samples **a** – **c**.

Elemental analysis for carbon, hydrogen, and nitrogen was also performed on samples **a** - **c** (Table 7.3.3). Given the assumed hydroxyl density at the surface of 2 – 3.5hydroxyls/nm^2, the elemental analysis showed about 60% saturation of the surface, corroborating evidence from the ^{29}Si SS-NMR. To give

more insight into the nature of the surface species present, a molar ratio of each element was determined relative to nitrogen, which was fixed at 2 to represent the stoichiometry of nitrogen in the ligand. Given the molar ratios, the majority of the ligand appeared to be intact on the surface. However, the carbon ratio is lower than expected for a completely intact ligand, which can be explained by the loss of a fragment as large as C_4 from the ligand upon surface adsorption.

To further elucidate the adsorption mechanism a small amount of sample **b** was washed with D_2O to etch off the chemisorbed surface species for study using HR-NMR (Figure 7.3.8, bottom trace). This relatively clean spectrum shows that all the peaks from the surface species match what is known for the iminopyrrolidinate ligand, with an absence of the signal for the methyl groups from the tert-butyl substituent. This concretely demonstrates that the tert-butyl substituent was eliminated upon initial surface adsorption at 275°C. The somewhat higher hydrogen ratio likely had a contribution from the silica hydroxyl groups, which dehydrated during the combustion analysis.

Table 7.3.3: Elemental Analysis of Samples a – c. Data for Sample a was Below the Limit of Detection.

		sample **a**	sample **b**	sample **c**
C	wt%	< 0.3	2.71	4.16
	mole ratio	-	7	7
H	wt%	< 0.3	0.59	0.79
	mole ratio	-	17	16
N	wt%	< 0.3	0.95	1.40
	mole ratio	-	2	2

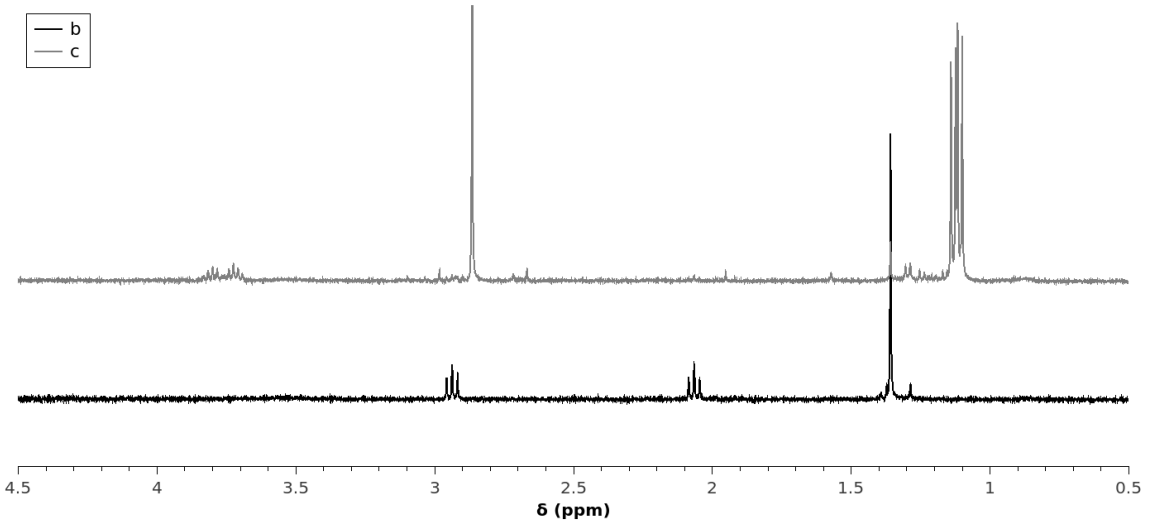

Figure 7.3.8: High-resolution ^{1}H NMR of D_2O after it was washed over samples **b** and **c**.

The thermal stability of the initial chemisorbed species was examined by annealing **b** at 350°C for 4 h under vacuum, producing sample **c**. The ^{13}C CP/MAS SS-NMR for **c** gave a spectrum that was somewhat similar to that of **b** (Figure 8.3.7). However, the quaternary carbon signal originally at 176.5ppm was not present and a new quaternary carbon signal appeared at 160ppm. The other quaternary carbon signal present in **b** also appeared for **c** with a considerably

weakened intensity from the annealing process. Two new carbon signals have appeared at 10 and 45ppm, confirming that a new surface species forms. The ^{29}Si CP/MAS SS-NMR spectrum for **c** was very similar to unmodified silica (Figure 7.3.6). Even at temperatures as high as 350°C, no alkylation of the silicon occurred at the surface and any thermolyzed chemisorbed species were still bonded through a ≡Si-O-R type interaction. Again, there was a change in the intensity of the peaks originating from each silica environment. Similar to the signal from **b**, the intensity of the silianol species at the surface decreased with respect to the signal for completely dehydroxylated silicon. This is likely due to the participation of silanol protons in the decomposition mechanism of the chemisorbed species from **b**.

Similar to the study done for **b**, a small of amount of **c** was washed with D_2O and examined via ^{1}H HR-NMR (Figure 7.3.8, top trace). Similar to the ^{1}H HR-NMR of **b**, the spectrum for **c** was very clean and exhibited only one species. There were two doublets and two septets, representing iso-propyl groups. There was an isolated singlet, which integrated to two protons relative to the isopropyl group. This singlet is too shielded to be an imine group (like ^{i}PrN=CH$_2$), and thus it could be that both nitrogen atoms remain in the surface species to form a methylene diimine. A mass spectal analysis of a non-deuterated aqueous solution found a peak at 89amu, which is the mass of this surface species with an additional proton. Using a hybrid quadropole time-of-flight mass spectrometer, the fragmentation of this parent ion supported the formulation ^{i}PrN(H)CH$_2$NH$_2$ (Figure 7.3.9). Thus, the ring methyls become the methyls of an isopropyl group,

and the quatenary carbon is protonated to produce a methylene. Interestingly, Chabal et al. also suggest a diamine as a stable surface species during ALD of Cu metal on SiO_2 substrates.[135] Combustion analysis of **c** did not clarify the formulation, giving very similar carbon, hydrogen and nitrogen molar ratios to that of **b** (Table 7.3.3). A more rigorous surface study is planned to clarify the 350°C thermolysis mechanism.

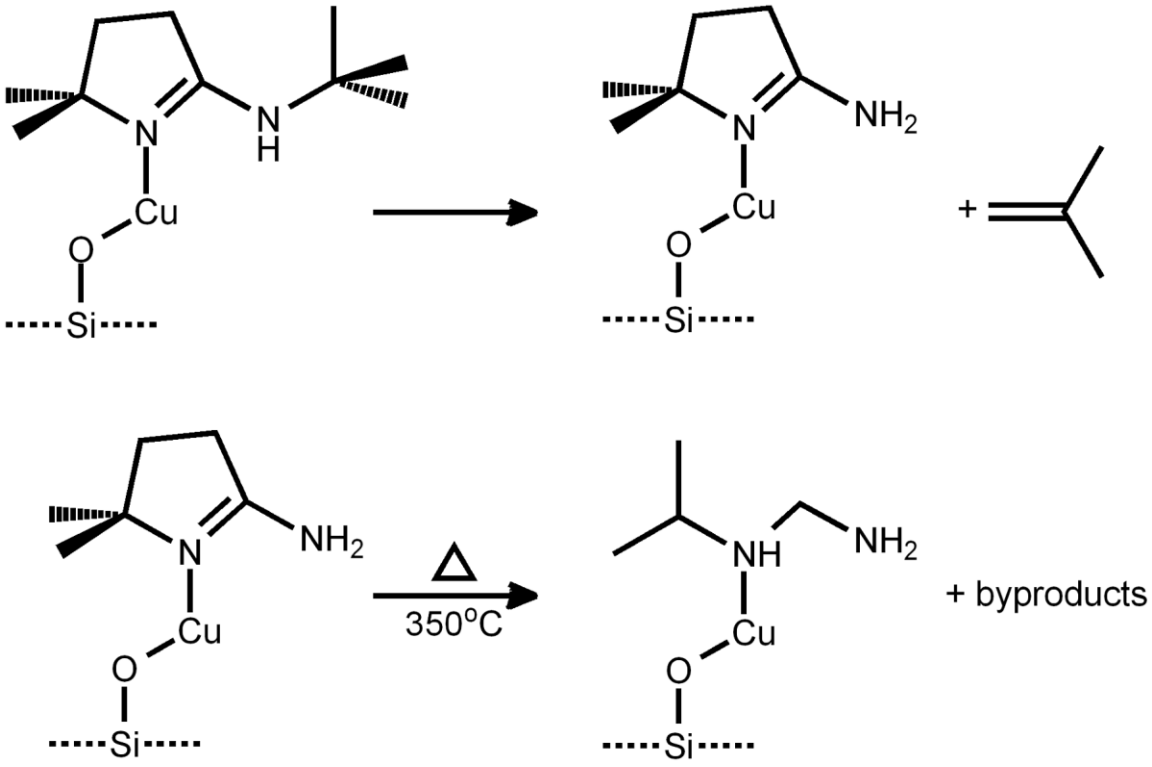

Figure 7.3.9: Possible thermolysis of the surface species formed by **3** on high-surface area silica.

7.4 Experimental

General Considerations: All manipulations involving the synthesis and handling of copper(I) compounds were performed in a nitrogen filled drybox. The chemicals CuCl and 2.5M BuLi in hexanes were purchased from Aldrich Chemical Company and used as received. All solvents used in manipulation of copper(I) compounds were ACS grade and purified from an MBraun Solvent Purifier System. All other solvents were ACS grade and used as received. Nuclear Magnetic Resonance experiments were performed on 300 MHz Avance 3 and 400 MHz Bruker AMX spectrometers. Canadian Microanalytical Service Ltd. performed combustion analyses. Thermogravimetric analysis was performed on a TA Instruments Q50 apparatus located in an MBraun Labmaster 130 drybox under a nitrogen atmosphere. Isopropyl-iminopyrrolidine and tert-butyl iminopyrrolidine were prepared by literature procedures.[128]

Copper(I) isopropyl-iminopyrrolidinate (1): Isopropyl-iminopyrrolidine (5.11g, 40.49mmol) was partially dissolved in 60mL of Et_2O and cooled to 0°C in an ice bath. N-butyl lithium (16.2mL) was added dropwise and a suspension formed after stirring for 2 h. In a separate flask, CuCl (4.2g, 42.42mmol) was suspended in 60mL of THF and cooled to 0°C in an ice bath. The suspension of lithium isopropyl-iminopyrrolidine was added via cannula to the cooled suspension of CuCl and was then allowed to warm to room temperature and stirred overnight. The volatiles were removed from the reaction flask by reduced pressure and the remaining solid was stirred in 100mL of toluene for 10 minutes. The cloudy

solution was filtered and the clear filtrate was concentrated under vacuum and kept at -35°C for 2 days. A mass of small, needle crystals was collected by filtration, washed with pentane and then dried under vacuum to afford 5.03g, 65.8%. mp 138°C. ^{1}H NMR (400 MHz, C_6D_6): δ 3.49, 3.24 (m, 1H, NC*H*$(CH_3)_2$); 3.34, 3.26 (t, 2H, NC*H*$_2CH_2CH_2C$); 2.04 (t, 2H, $NCH_2CH_2CH_2$C); 1.58 (quintet, 2H, $NCH_2CH_2CH_2C$); 1.487, 1.304, 1.208, 1.158 (d, 6H, NCH(C*H*$_3)_2$). ^{13}C NMR (300 MHz, C_6D_6): δ 179.84, 175.38, 54.19, 53.30, 53.15, 51.19, 50.48, 50.00, 29.02, 28.69, 28.65, 27.70, 27.55, 27.39, 27.36, 24.99, 24.72, 24.64. Combustion analysis, found (calculated): C, 44.63 (44.55); H, 7.11 (6.94); N, 14.84 14.84).

Copper(I) tert-butyl-iminopyrrolidinate (2): Tert-butyl iminopyrrolidine (1.72g, 12.26mmol) was dissolved in 60mL of THF. N-butyl lithium (4.9mL, 2.5M) was added and the solution was stirred for 2 h. CuCl (1.25g, 12.62mmol) was added in one portion and the suspension was stirred overnight. Volatiles were removed under reduced pressure and the remaining solid was taken up in THF and filtered. The filtrate was concentrated and then kept at -35°C for 1 day. Colourless, block crystals were collected by decanting the solution, washing with pentane, and then drying under vacuum; obtained 1.59g, 63.9%. mp 148°C. ^{1}H NMR (300 MHz, C_6D_6): δ 3.25 (t, 2H, NC*H*$_2CH_2CH_2C$), 2.19 (t, 2H, $NCH_2CH_2CH_2$C), 1.63 (quintet, 2H, $NCH_2CH_2CH_2C$), 1.32 (s, 9H, NC(C*H*$_3)_3$). ^{13}C NMR (300 MHz, C_6D_6): δ 180.01 ($NCH_2CH_2CH_2C$), 52.45 (N*C*$H_2CH_2CH_2C$), 33.72 (N*C*$(CH_3)_3$), 33.26 (NC(*C*$H_3)_3$), 31.64 ($NCH_2CH_2CH_2C$), 26.33 ($NCH_2CH_2CH_2C$). Combustion analysis, found (calculated): C, 47.08 (47.39); H, 7.49 (7.46); N, 13.69 (13.82).

Crystallography: X-ray structural analysis for **1** and **2**: Crystals were selected and mounted on plastic mesh using viscous oil flash-cooled to the data collection temperature. Data were collected on a Bruker-AXS APEX CCD diffractometer with graphite-monochromated Mo-Kα radiation (λ = 0.71073 Å). Unit cell parameters were obtained from 60 data frames, 0.3ºω, from three different sections of the Ewald sphere. The systematic absences in the data and the unit cell parameters were uniquely consistent to *Ccca* for **1** to $P2_{1/c}$ for **2** and. The data-sets were treated with SADABS absorption corrections based on redundant multiscan data.[i] The structures were solved using direct methods and refined with full-matrix, least-squares procedures on F^2. The compound molecules were each located on an inversion point in **2**. Two symmetry unique but chemically identical molecules of the compound in **1** are each located on a two-fold rotation axis: in one case the two-fold axis is parallel to the N-Cu-N axis and in the other case the two-fold axis is perpendicular to the N-Cu-N axis bisecting the Cu atoms on the opposite distal positions of the tetracopper rhombus. One THF solvent molecule of crystallization per two tetrameric complexes in **1** was located severely disordered and treated as diffused contribution.[51] One isopropyl group in **1** was located disordered with a 23/77 refined occupancy ratio. Chemically equivalent bond distances and angles in the disordered group were restrained to average values with equal atomic displacement atomic parameter contraints on equivalent atoms. All non-hydrogen atoms were refined with anisotropic displacement parameters. All hydrogen atoms were treated as idealized contributions. Atomic scattering factors are contained in the SHELXTL 6.12 program library.[140]

Surface Exposure Experiments: The exposure experiments were performed in a home-built reactor. The reaction chamber consisted of a stainless steel ring support covered in 200 stainless steel mesh with a plug of glass wool to prevent loss of silica powder. The system had one inlet from a heated bubbler and one inlet for He (purity of 99.999 %). All fittings used in this system were either CF or VCR to ensure a high-vacuum seal. The system was leak checked using a gas thermal conductivity/ leak detector (Gow-Mac Instrument Co.) and an overpressure of He. For the exposure experiments, typically about 1 g of high surface area SiO_2 powder (EP10X; PQ Corporation; $300m^2/g$ S.A.; $1.8cm^3/g$ P.V.; 24nm P.S.; 100μm P.D.) was used. The powder was pre-treated in the reactor at 350˚C for 16 h under vacuum before exposure to the precursor. The reactor and lines were heated to temperature and allowed to equilibrate for 1 – 2 h before introduction of the precursor. The precursor (typically 0.6 – 0.8g) was then vaporized and transported to the substrate with the system under 10^{-3}Torr vacuum. The substrate was exposed to volatilized precursor for 17 h before the system was cooled to room temperature for handling. Both precursor and substrate were handled in inert atmosphere. Annealing experiments were performed in a tube furnace while under vacuum. Samples were loaded into the furnace under a blanket of nitrogen gas. Samples were annealed for 2 h.

Characterization of Surface Species: Solid-state NMR experiments were performed at 4.7T on a Bruker Avance III console. All spectra were obtained using a Bruker 7mm $^1H/X/Y$ probe. ^{13}C (ν_0 = 50.3MHz) cross-polarization magic angle spinning (CP/MAS) experiments were collected at a spinning rate of

4.5kHz using a 3.4μs 90° proton pulse with a contact time of 2ms where the contact pulse was ramped on the ^{1}H channel. A relaxation delay of 2s was sufficient to prevent saturation and typically total acquisition times were 16 – 30 h. Glycine was used as an external secondary reference for the ^{13}C chemical shift scale. Spectra were treated with 40Hz line broadening during processing. ^{29}Si (v_0 = 39.7MHz) CP/MAS experiments were collected at a spinning rate of 4.5kHz using a 3.85μs 90° proton pulse with a contact time of 10ms where the ^{1}H channel contact pulse was ramped. The relaxation delay was 2s and typically required 2 – 8 h acquisition times. TMSS was used as an external reference for the ^{29}Si chemical shift scale. Spectra were treated with 30Hz line broadening during processing. All spectra were obtained with high power proton decoupling during acquisition.

Samples were prepared for High Resolution NMR (HR-NMR) by adding a small amount, typically 40 – 50mg, of modified silica powder to 2mL of D_2O (Sigma), agitating, and allowed to sit for 15 minutes. The D_2O solution was then decanted and studied via HR-NMR. d_4-TSP was used as an internal reference.

Electron dispersive X-ray spectroscopy (EDX) was performed on the modified silica samples as qualitative proof for the presence of copper. Samples were mounted on an aluminum support using carbon tape and loaded into a Tescan Vega II SEM equipped with an Oxford Inca 200 EDX for analysis.

7.5 Conclusions

A series of copper(I) iminopyrrolidinates were synthesized and evaluated by thermogravimetric analysis and in C_6D_6 solutions by ^1H NMR to determine their thermal stability and suitability as precursors in CVD processes. The employed unsymmeterical, cyclic amidinate ligand proved to impart excellent thermal stability when no β-hydrogens were present. A direct comparison of the number of β-hydrogens to thermal stability was complicated by the tetrameric structure of **1**, which was thought to influence thermal stability.

A valuable thermal stress test by TGA was devised and provided complementary thermal stability trends to solution-based thermolysis studies. Advantages of the thermal stress test by TGA was faster data collection, and use of conditions more pertinent to CVD processes. The solution-based thermolysis studies identified the parent amidine and copper metal as thermolysis products of **1** and **2**. The amidines were produced through an intramolecular hydrogen abstraction and a β-hydride abstraction mechanism was proposed. Compound **3** showed negligible decomposition in both the TGA and solution experiments, and is an excellent candidate for copper deposition experiments.

An extensive surface reactivity study of **3** was undertaken, revealing some interesting thermal behaviour. Compound **3** lost an alkyl group on chemisorption at 275°C, but was stable to thermolysis up to 350°C, demonstrating that the design of the ligand system did indeed protect the monolayer from thermolysis. At 350°C, the surface species underwent further thermolysis by an unknown

mechanism to produce a surface species suspected to be the methylenediamine $^{i}PrN(H)CH_2NH_2$.

Chapter 8 – Metal Assisted Chemical Etching Using Sputtered Gold: A Simple Route to Black Silicon

Please see preface, page 4, for more details and full article citation. Author contributions listed below are paraphrased from signed Letters of Permission to reprint this material.

Agnieszka Kurek is first author of this research paper. Her contributions to this published work included all experimental expect for radiance study, data interpretation, writing, editing and figure composition. Please see preface, page 4, for more details and full article citation.

Sean Barry contributed data interpretation, writing and editing.

8.1 Abstract

We report an accessible and simple method of producing “black silicon” with aspect ratios as high as 8 using common laboratory equipment. Gold was sputtered to a thickness of 8nm using a low-vacuum sputter coater. The structures were etched into silicon substrates using an aqueous H_2O_2/HF solution, and the gold was then removed using *aqua regia*. Ultrasonication was necessary to produce columnar structures, and an etch time of 24 min gave a velvety, non-reflective surface. The surface features after 24 min etching were uniformly microstructured over an area of square centimetres.

8.2 Introduction

Silicon porosification has been studied intensely since the early nineties.[141,142] The fabrication of silicon wafers with hollow pores ranging from <2nm to >50nm in diameter, while preserving the crystalline integrity of the surrounding silicon, has been explored for semiconductor applications.[143] Although the majority of this work has been undertaken using electrochemical methods, Metal-assisted Chemical Etching (MaCE) has also been well-studied.[144] Many types of noble metals have been used in MaCE, most commonly Ag, Au, Pt, and Pd, and each provide different porous silicon morphologies.[145] On the other hand, gold-assisted etching tends to produce isolated, straight pores, only in regions covered by the metal.[146] Therefore, using gold metal can allow more control over the pore distribution.

In general, the metal acts as a catalytic site to promote the activity of the oxidant. Typically, a solution of HF/H_2O_2 is used, and the peroxo oxygen undergoes reduction to produce water. An electron-depleted region is formed in the vicinity of the metal, and the silicon is oxidized and dissolved away as SiF_6^{2-}.

Black silicon is closely related to porous silicon but consists of high-density vertical pillars or nanowire assemblies. Black silicon characteristically has low reflectivity, as apparent in its matte, black colour and has great potential in photovoltaic applications or antireflective coatings.[147] It has also been investigated as a superhydrophobic surface, assisted by electrowetting.[148] Traditionally reactive ion etching is used, but MaCE has also shown promise for production of black silicon.[149,150] Ion sputtering is a relatively inexpensive, simple method that yields nanometer thick layers with good coverage, independent of substrate size.[151]

Some contributing factors to surface morphology include etchant composition, oxidizing agent, time of etch, agitation, and others. In recent literature, agitation by ultrasonication has been shown to detach H_2 bubbles that accumulate on the substrate surface during normal etching procedures and inhibit uniform etch.[152] Depending on how the metal was deposited, ultrasonication has had very contradictory effects. Reasons for this have not been adequately explained. It has been shown that the time of etch is proportional to the etching rate.[150] The aim of this study is to determine the effect of ultrasonication on the etching of silicon.

8.3 Results and Discussion

Our approach was to develop a simple, easily accessible, and scalable synthesis of black silicon using metal-assisted chemical etching with gold. To this end, we sputtered gold using a low-vacuum sputter coater common to SEM facilities, and etched using an ultrasonication bath common to chemical synthesis laboratories. In a typical experiment, an 18 x 6mm^2 silicon (100) wafer was sputtered with a layer of gold using a simple sputtering apparatus. AFM showed this layer to be 4 – 5nm thick, with a root mean square (RMS) roughness of 4.7Å, similar to that of the silicon substrate.

Of the many factors that contribute to the control of uniformity of roughness over the surface area of the etched wafer, ultrasonication has been the least explored in the literature. Recent work suggests that bubbles of H_2 created during etch stick to the substrate and shield the silicon surface from the etchant.[152] Therefore, bubble coalescence is a key event in the production of a rough surface. When two bubbles coalesce on the Si surface in an explosive event, a larger daughter bubble is formed and tiny micron-scale droplets of etching solution, formed by the impact, are scattered near the merging site and across the surface of the substrate. These droplets continue etching underneath the daughter bubble and once the bubble grows large enough, it is liberated from the surface. Thus, ultrasonication plays an important role in the formation of deep trenches, and we initially undertook a study of ultrasonication.

The duration of etch was held constant at 6 min, with one sample agitated and the other not (Figure 8.3.1). The non-agitated sample had a distinct “peaked” pattern with relatively smooth edges and features, while the ultrasonicated sample showed similar topography with features on the order of 500nm that dimpled the overall pattern (best depicted in Figure 8.3.1d). The round, concave dimples were found consistently across the entire substrate. It appears that ultrasonication caused these finer features. We suspect that H_2 bubbles, formed from the etching reaction, were subsequently imploded by ultrasonication and quickly exposed the surface to HF. The pressure and heat generated at the site of an ultrasonication-generated bubble implosion likely accelerates the HF etch.

The samples looked different when the etch time was extended up to 24 min. With sonication, they took on a velvety, black appearance, reflecting little light compared to the parent silicon. Without sonication, there was an obvious “rainbow” hue of interference colour, and the samples exhibited a strong iridescence. Attempts to measure the reflectance of the non-sonicated samples were hampered by this, and the data were not reportable. However, reflectance experiments could be carried out on the sonicated samples.

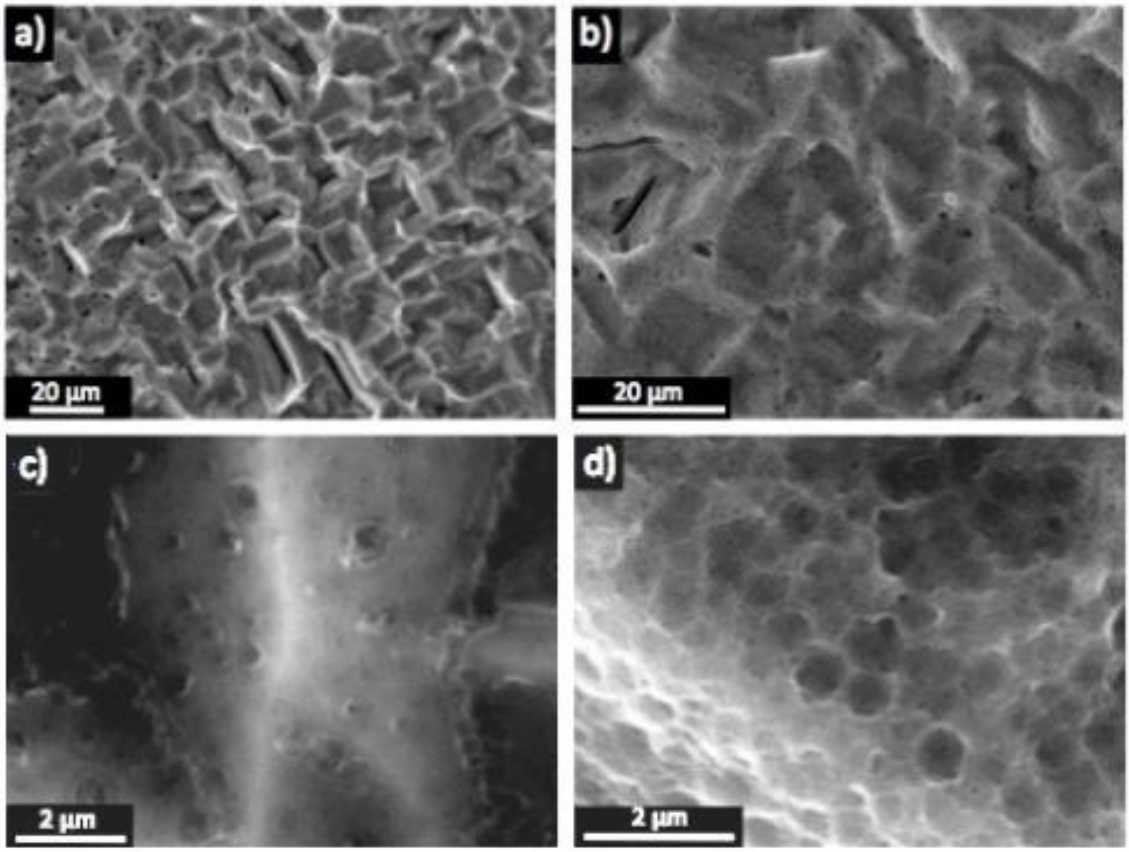

Figure 8.3.1: SEM images demonstrating a 6 min etch of silicon by peroxide/HF with an 8 nm sputtered gold film. Panels a) and c) show different magnifications of a sample etched without ultrasonication. Panels b) and d) show the effect of ultrasonication. Both samples are shown with gold remnants on the surface.

When the etching time was increased with ultrasonication, these dimples deepened and became meso- and macro-pores (Figure 8.3.2). The pore diameters were polydisperse, and the structure was made more complicated as the overall peak pattern of the silicon surface became more extreme. Indeed, the structures seen after a 24 min etch appeared to be more uniform. The SEM images showed that the microstructure adopted an ever-increasing columnar appearance (Figure 8.3.2). The structure has a random distribution of features, but the aspect ratio and columnar nature are most apparent when viewed at 45°

to the plane view. When the substrates were cleaved and SEM images taken of the cross sections, the depth of the pores became apparent.

It was notable that etching up to 6 min produced a significantly different structure than etching up to 12 min or longer. We suspect the initial period of sonication etches slowly because there is a uniform film of gold. As the etching continues, the gold coalesces into assemblies of nanoparticles and then the etching can proceed faster, and can form deeper structures.

The aspect ratios of the features developed were relatively disperse, and there appeared to be a levelling off of this aspect ratio as the etch time was increased (Figure 8.3.3). As the etch time increased, the porous features also became relatively more uniform in depth. This was an advantageous outcome because the goal was to produce deeply etched, thin, pillar-like structures by etching a high density of pores.

The roughened silicon surface was quite uniform, but extended inspection by SEM showed the occasional occurrence of a plateau with a different, dimpled texture (Figure 8.3.5). This “upper layer” of etched silicon appeared to become so significantly etched as time was increased that it lifted off from the lower layer. Indeed, black fragments were observed visually in the solution at 18 and 24 min of etching. This phenomenon was repeatable, and the upper layer could be seen by SEM to have a thickness on the order of 10 to 25μm, depending on the duration of the etch.

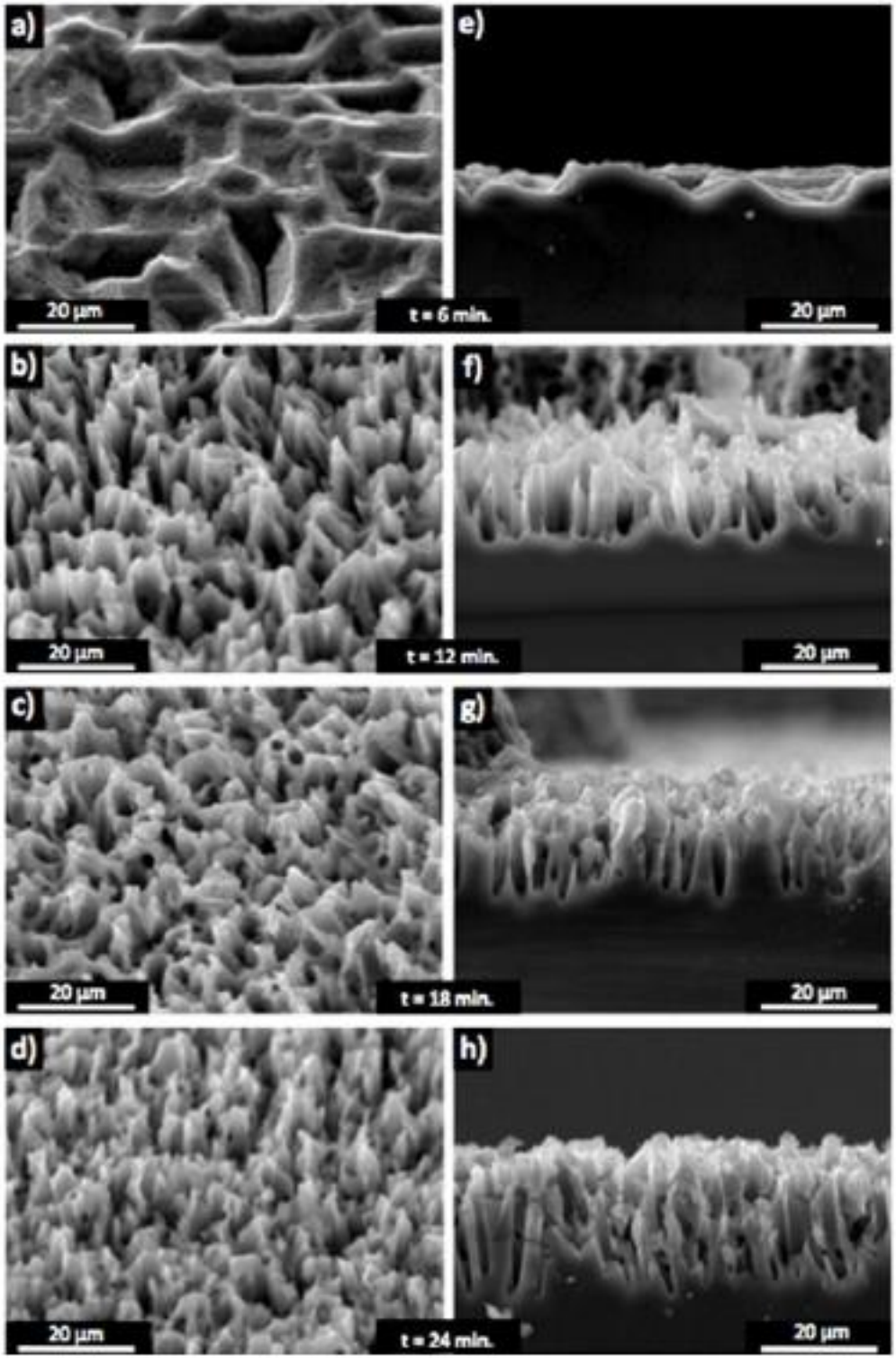

Figure 8.3.2: The aspect ratio of surface features as a function of etch time. Panels a) – d) show a 45°-inclined view and panels e) – h) show a cross-sectional view.

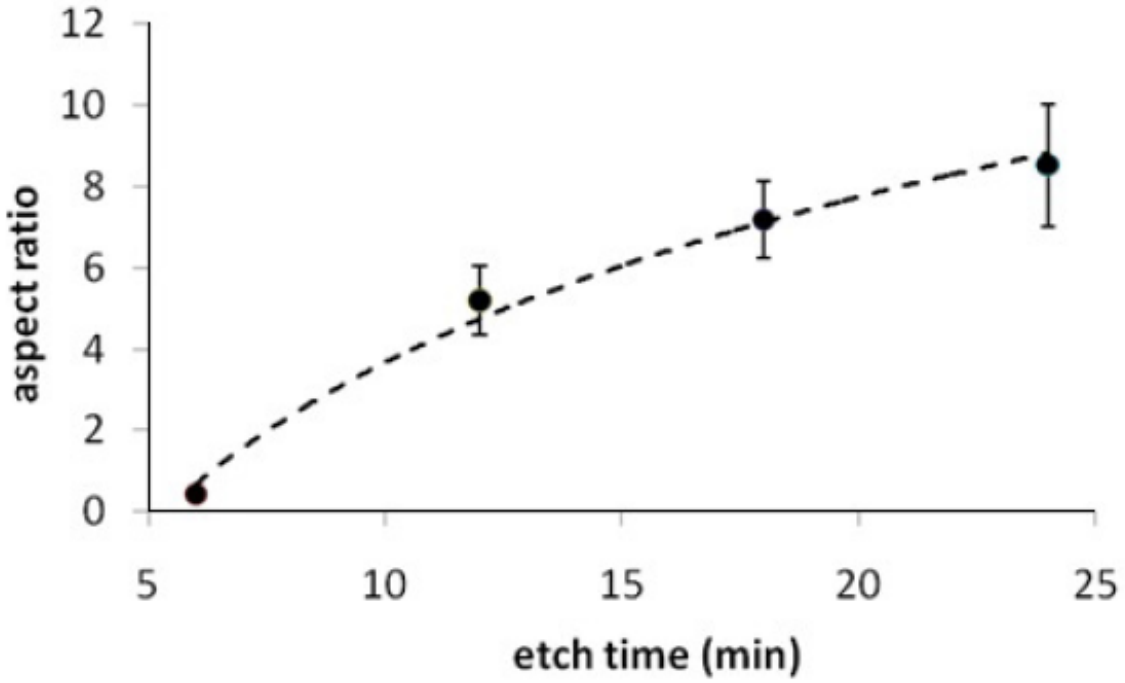

Figure 8.3.3: The aspect ratio of surface features as a function of etch time. The etch rate fits a logarithmic trend (shown as a dashed line) with a coefficient of determination (R^2) of 0.9909.

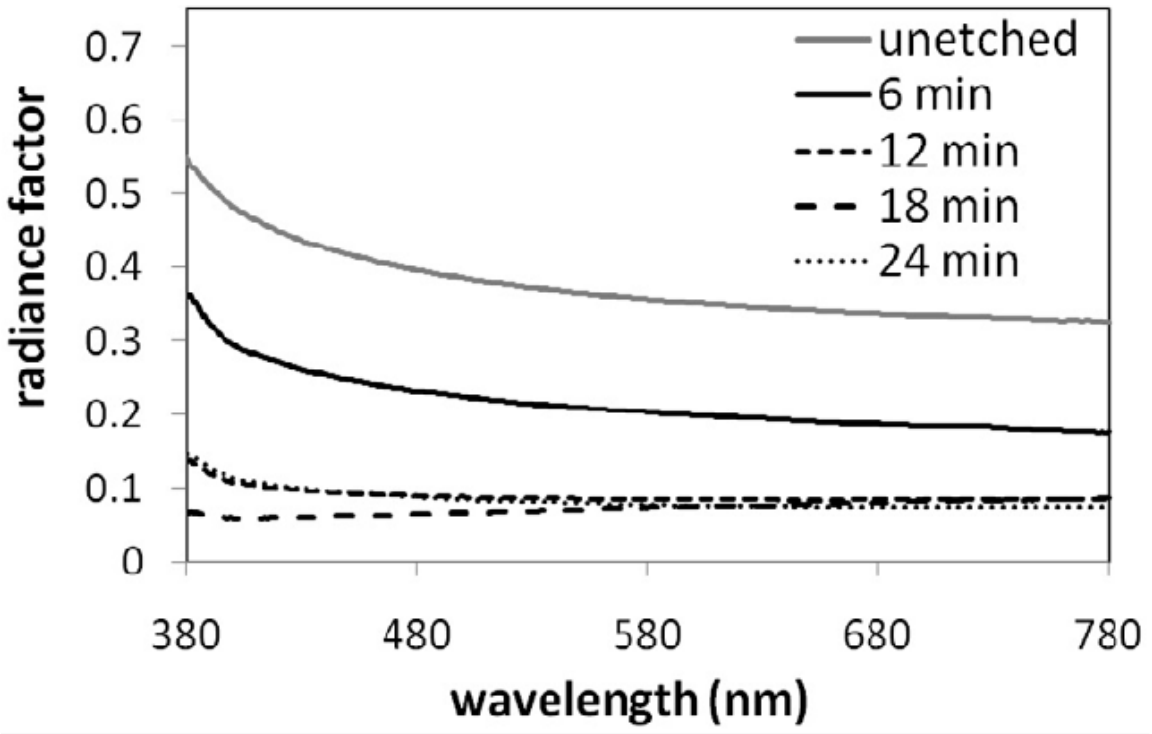

Figure 8.3.4: The radiance factor over the visible spectrum of the samples etched for 0 – 24 min with sonication.

The reflectivity was measured for the samples etched for different lengths of time with sonication, where the radiance factor is the normalised radiance at that angle, compared to the illuminant (Figure 8.3.4). The samples were illuminated normal to the surface, and the reflectivity was measured at 45° to normal. Because the samples were very matte, this non-specular reflection was similar at all angles of observation. It should be noted that the silicon was measured with an illumination angle at -45° to normal, in plane with the observation angle. This is necessary since the reflectance is highly specular for unetched silicon.

While the sample etched and sonicated for 6 min showed intermediate radiance, the radiance of the samples etched for 12 min and longer was very low, around 10% across the visible spectrum. This corroborates our observation by SEM that the 6 min sample had a different surface structure likely due to the slow etch through the initial gold film, while the subsequent samples adopted a more uniform and deeply etched nanostucture. It is also striking that these samples differ very little (only at low wavelength for the 18 min etch), and so the larger aspect ratios at longer etch times seem to have little effect.

By comparing SEM images of samples etched for different lengths of time, it was observed that longer etch time produced thinner top layers that covered a decreasing fraction of the substrate. Figures 8.3.5a and 8.3.5b show a relatively complete top layer, with only a small amount of delamination to reveal the lower layer. As the etch time is increased, the upper layer is reduced to isolated plateaus (Figures 8.3.5c and 8.3.5d). The etching continued through these plateaus and into the lower layer (Figures 8.3.5e and 8.3.5f) as the etching

continued. It was interesting to see that some pores etched in a “bent” manner (Figure 8.3.5f), a phenomenon that has been previously described.[153]

In several panels in Figure 8.3.5 there appear to be wider pores located around the outline of the upper layer. Cross-sectional SEM images showed that these were significantly deeper etched features (Figure 8.3.6). It can be seen that one such pore was on the order of 45 μm in depth when the pore was serendipitously located on a cleaved edge (Figures 8.3.6a and 8.3.6b). The pore is nestled in the top layer with roots throughout the lower layer. It seems likely that these pores in the top layer etched deeper than those formed elsewhere where a large gold particle was formed during sputtering. Given the simplicity of the coating technique, these deeper features were surprisingly rare.

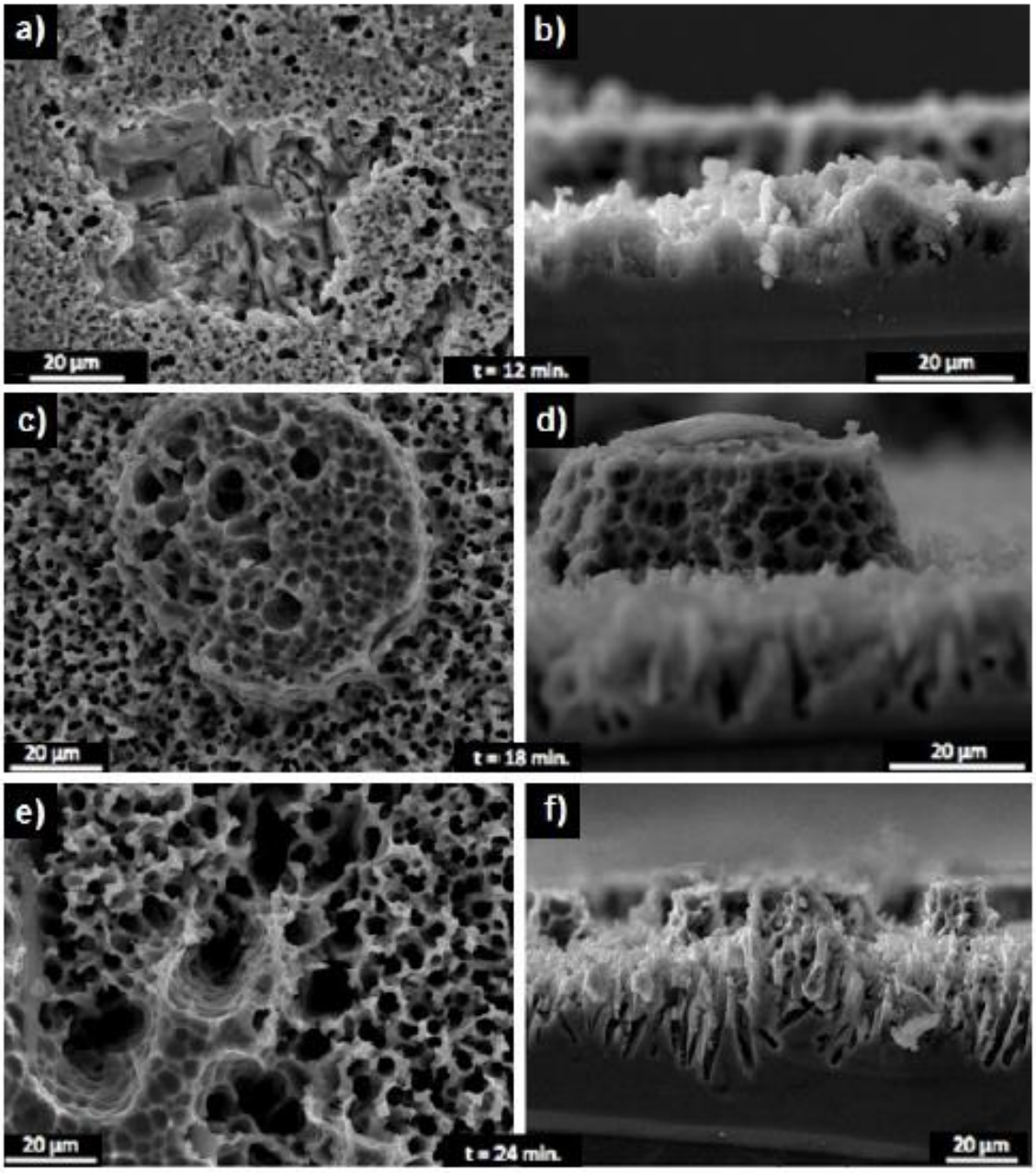

Figure 8.3.5: SEM images showing the top layer that is formed and liberated from the substrate during a peroxide/HF etch for various etch times. Panels a), c) and e) show plane view and panels b), d) and f) show a side view. Panels a) and b) show a typical top layer after 12 min etching. Panels c) and d) show an isolated "plateau" feature after 18 min etching. Panels e) and f) show the pores etched through the top layer "plateau" features and into the underlying layer after 24 min etching. All samples are shown with gold remnants present on the surface.

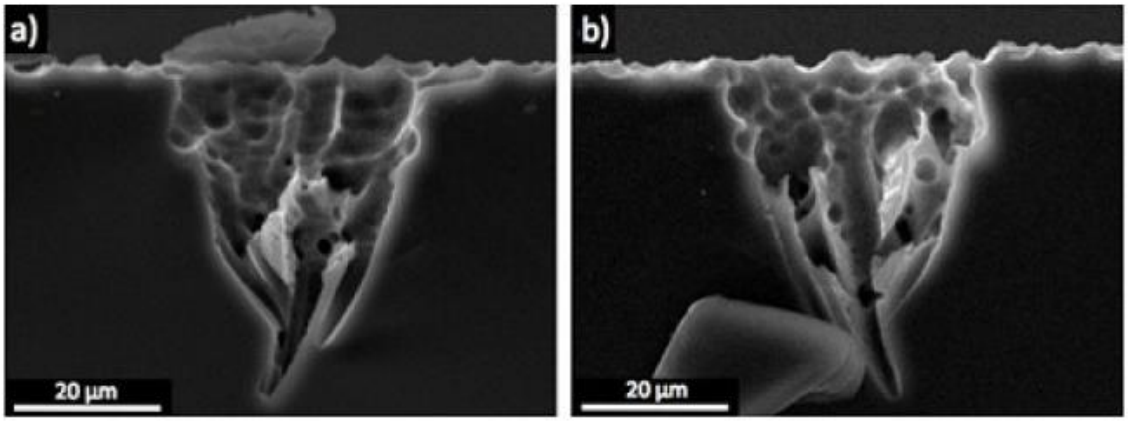

Figure 8.3.6: SEM images of the same pore on two complementary edges of a cleaved substrate. The sample shown was etched for 24 min and gold catalyst has been removed by aqua regia.

8.4 Experimental

Si (100) wafers were cleaned using a standard piranha surface treatment. The 18 x 6mm^2 substrates were coated with sputtered gold using an Anatech Ltd. HUMMER VII Sputtering System set to deposit 8nm. Each sample was submerged in a beaker containing 24mL of aqueous etchant solution, comprised of H_2O_2 (4.3M, 15mL) and HF (2M, 3mL), and ultrasonicated in a VWRTM Model 250D sonicator for a duration of 6 – 24 min. Scanning electron microscopy (SEM) images were acquired with a Tescan Vega-II XMU VPSEM scanning electron microscope and atomic force microscopy (AFM) data were collected with an NTEGRA NT-MDT ST0505 system.

8.5 Conclusions

The reported very simple sputter-etch method produced black silicon of very good quality that covered square centimetres. It can be easily carried out in common laboratory equipment and thus enables small-scale production of low-reflectivity, black silicon.

Chapter 9 – Conclusions

Centralized around a theme of thin films, this work investigated CVD precursor design – primarily thermolysis studies of ligands and metal complexes. Work involving MACE of gold films using a physical deposition method showed that the process could be more facile than solution-based MACE.

A literature review of guanidinate ligands highlighted the versatility of this ligand system and the effect of small modifications to the structure on the electronics of resultant metal compounds. With many substitutions possible at the nitrogen heteroatoms, the tunability of these ligands can be exploited on many different metal centres for maximal volatility and thermal robustness.

Logical design of iminopyrrolidine ligands addressed a thermal decomposition pathway commonly seen in guanidinate compounds involving CDI deinsertion. The ligands were tested on aluminum centres employng TMA and TEA in ligand exchange. A similar melting point trend was observed for both neutral ligands and Al compounds. ^{1}H NMR studies suggested that these compounds were more thermally stable in solution than the analogous amidinate and guanidinate Al compounds. A dimer was discovered after several days in solution at elevated temperatures.

Thermal ALD of copper films has been described in the literature in many processes using many types of precursors and temperatures. In general, most CVD of copper begins around 200 – 230°C. This is a very important factor in the design of ALD processes and second precursors can be used to activate the

copper metal deposition at low temperatures. There is still room for precursor development, although copper(I) betadiketonates are well-established.

Three novel copper(I) compounds were synthesized in good yield from 1,3-diisopropyl-imidazolin-2-ylidene copper hexamethyl disilazide. Thermogravimetric analysis showed excellent neutral ligand volatility, that was, for the most part imparted onto the respective copper(I) compounds as well. Some decomposition was noticed, as residual masses were non-zero, however all were below the molecular mass of copper in each compound. The reactivity of hexamethyldisilazide can be used to expand this family of precursors, taking advantage of the stabilizing n-heterocyclic carbene. Future deposition experiments using **3** from this study would be relatively straightforward. Since the on set of volatilization was around 165°C, but since the precursor bubbler would be under vacuum, a lower temperature of 110°C is about the temperature that it should be set to. This temperature could be cautiously increased if the rate of mass transport of the precursor is too slow. In a simple hot-walled CVD reactor, forming gas could be used as a carrier gas to deliver **3** to a substrate that would be heated independently to 150 - 200°C. This temperature should always be at least hotter than the bubbler to prevent condensation. The substrate could be silicon to begin, but glass and alumina would be interesting to try as well. Several variables, including bubbler temperature, substrate temperature, precursor mass, carrier gas flow rate should be systematically tuned to optimize the deposition of copper metal.

Further enhancement was designed into the iminopyrrolidinate ligand to address a second decomposition pathway: beta hydrogen elimination. Precursor **1** proved to be very stable in solid, solution and vapour phases. At 275°C this precursor undergoes alkene elimination from the chelating nitrogen while chemisorbed to a silica surface.

A new series of copper(I) iminopyrrolidinates was synthesized and evaluated for thermal properties. The ligand with no beta hydrogens yielded the most stable copper compound, as shown in the TGA stress test. This finding was supported by the lack of decomposition in a solution-based ^{1}H NMR study of all of the compounds. In this study, compounds **1** and **2** showed amidine formation and reduction to copper metal through a proposed intramolecular beta hydrogen elimination pathway. This was not seen in compound **3**.

The physical vapour deposition method of sputtering was used to deposit thin gold films on silicon and roughen the surface with nanostructures using metal-assisted chemical etching. This process is typically done with solution-based metal nanoparticles and this study showed that having the metal already in contact with the surface, allows for an effective, controllable etching rate. The aspect ratio of the resultant structures can be controlled using etching time. Removing the substrate from the etchant and rinsing with distilled water easily quenched the reactions.

In future work, the ligands developed here should be applied to other metal centres, such as titanium, nickel, silver and gold as thin films of these are also desirable in many industries. CVD or ALD experiments should also be

carried out with the copper compounds developed in Chapter 5, to achieve a true sense of whether they are copper metal precursors.

This work showcases the evolution and versatility of volatile ligands. Logical changes such as tethering two ends together or removing beta hydrogens can have the anticipated effects. For a summary of the ligand modifications that were presented in this thesis, see Tables 9.0.1 and 9.0.2, below. It is worth studying and improving ligands because a great precursor may be uncovered without starting from scratch. If a ligand does not work well on a certain metal centre, it may find a use on a different one. The recyclable and reusable nature of ligands like guanidines makes them interesting to work on. This thesis also showed that PVD methods like sputtering and perhaps CVD and ALD can lead to metal films with new and creative applications. Perhaps these methods can add some degree of control over MACE and improve the efficiency of black silicon solar cells in future work.

Table 9.0.1: Summary of Ligand Improvements to $[Cu(iPr\text{-}guan)]_2$

Metal compounds	Structure of Ligand	Problem/Modification	Impact
$Al(iPr\text{-}amd)_2R_2$ (Chapter 3) **$Al(guan)_3$** (Chapter 2) **$[Cu(iPr\text{-}guan)]_2$** (Chapter 7)	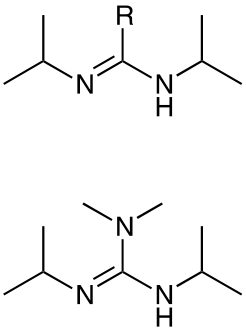	Undergoes β-hydrogen elimination and CDI deinsertion at elevated T	Impurities in deposited films
$ipAlMe_2$ (Chapter 3) **$ipAlEt_2$** (Chapter 3) **$(Cuip)_2$** (Chapter 7)	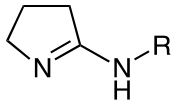	Pyrrole ring	Eliminated CDI deinsertion pathway
$tbipAlMe_2$ (Chapter 3) **$(Cutbip)_2$** (Chapter 7)	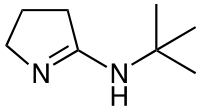	Tert-butyl R-group; removed of some β-hydrogens	Increased thermal stability and volatility
$[Cu(dtip)]_2$ (Chapters 6 and 7)	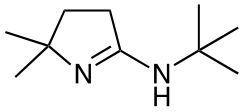	Added two methyl moieties onto pyrrole ring	Eliminated β-hydrogen abstraction; increased thermal stability and volatility

Table 9.0.2: Summary of Ligand Improvements to (NHC)Cu(HMDS)			
Cu compounds (Chapter 5)	**Structure of Ligand**	**Problem/Modification**	**Impact**
(NHC)Cu(HMDS)	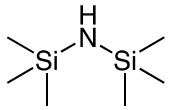	Relatively high MW (160.38 g/mol)	May promote Si impurities into deposited film or hinder volatilization
(NHC)Cu(N-acetylbezamide)	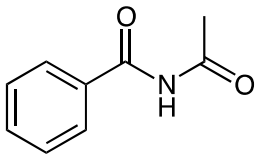	No Si, but similar MW (162.17 g/mol)	Ligand onset of volatility is147.6°C; Cu compound residual mass of 10.1%
(NHC)Cu(diacetamide)	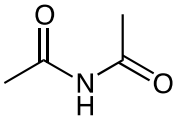	Removed phenyl ring; lowered MW (100.10 g/mol)	Lowered ligand onset of volatility to 82.6°C; Cu compound residual mass of 18.0%
(NHC)Cu(acac)	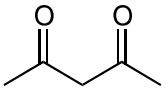	Removed amide; lowered MW (99.11 g/mol)	Lowest Cu compound residual mass of 5.8%

References

[1] V. Craciun, M. Guilloux-Viry, M. Alexe, G. Catalán Bernabé, M. Fanciulli, A. Devi, S. Cwik, K. Xu, A. P. Milanov, H. Noei, et al., *Thin Solid Films* **2012**, *520*, 4512–4517.

[2] F. T. Edelmann, *Chem. Soc. Rev.* **2012**, *41*, 7657–72.

[3] K. Xu, A. P. Milanov, H. Parala, C. Wenger, C. Baristiran-Kaynak, K. Lakribssi, T. Toader, C. Bock, D. Rogalla, H.-W. Becker, et al., *Chem. Vap. Depos.* **2012**, *18*, 27–35.

[4] S. T. Barry, P. G. Gordon, M. J. Ward, M. J. Heikkila, W. H. Monillas, G. P. a Yap, M. Ritala, M. Leskelä, *Dalt. Trans.* **2011**, *40*, 9425–30.

[5] T. Prieur, V. Brizé, T. Cornier, B. Doisneau, A. Farcy, R. Boichot, A. Mantoux, S. Daniele, E. Blanquet, *J. Nanosci. Nanotechnol.* **2011**, *11*, 8383–8386.

[6] A. P. Milanov, K. Xu, A. Laha, E. Bugiel, R. Ranjith, D. Schwendt, H. J. Osten, H. Parala, R. A. Fischer, A. Devi, *J. Am. Chem. Soc.* **2010**, *132*, 36–7.

[7] V. Miikkulainen, M. Leskela¨ M. Ritala, R. L. Puurunen, *J. Appl. Phys.* **2013**, *113*, 021301.

[8] C. J. Carmalt, A. C. Newport, S. a O'Neill, I. P. Parkin, A. J. P. White, D. J. Williams, *Inorg. Chem.* **2005**, *44*, 615–9.

[9] A. P. Kenney, G. P. A. Yap, D. S. Richeson, S. T. Barry, *Inorg. Chem.* **2005**, *44*, 2926–33.

[10] J. P. Coyle, P. A. Johnson, G. A. DiLabio, S. T. Barry, J. Müller, *Inorg. Chem.* **2010**, *49*, 2844–50.

[11] T. B. Thiede, M. Krasnopolski, A. P. Milanov, T. de los Arcos, A. Ney, H.-W. Becker, D. Rogalla, J. Winter, A. Devi, R. A. Fischer, *Chem. Mater.* **2011**, *23*, 1430–1440.

[12] T. A. Mih, S. Paul, A. P. Milanov, R. Bhakta, A. Devi, *ECS Trans.* **2009**, *25*, 901–907.

[13] S. J. Kim, K. Xu, H. Parala, R. Beranek, M. Bledowski, K. Sliozberg, H.-W. Becker, D. Rogalla, D. Barreca, C. Maccato, et al., *Chem. Vap. Depos.* **2013**, *19*, 45–52.

[14] K. Xu, A. P. Milanov, M. Winter, D. Barreca, A. Gasparotto, H.-W. Becker, A. Devi, *Eur. J. Inorg. Chem.* **2010**, *2010*, 1679–01688.

[15] M. Eleter, S. Daniele, V. Brize, C. Dubourdieu, C. Lachaud, N. Blasco, A. Pinchart, *ECS Trans.* **2009**, *25*, 151–158.

[16] A. P. Milanov, T. B. Thiede, A. Devi, R. a Fischer, *J. Am. Chem. Soc.* **2009**, *131*, 17062–3.

[17] A. P. Milanov, K. Xu, S. Cwik, H. Parala, T. de los Arcos, H.-W. Becker, D. Rogalla, R. Cross, S. Paul, A. Devi, *Dalton Trans.* **2012**, *41*, 13936–47.

[18] J. P. Coyle, W. H. Monillas, G. P. A. Yap, S. T. Barry, *Inorg. Chem.* **2008**, *47*, 683–9.

[19] L.-Y. Shao, J. P. Coyle, S. T. Barry, J. Albert, *Opt. Mater. Express* **2011**, *1*, 128.

[20] T. Kim, Y. Yao, J. P. Coyle, T. Barry, F. Zaera, *Chem. Mater.* **2013**, *25*, 3630–3639.

[21] M. Gebhard, M. Hellwig, H. Parala, K. Xu, M. Winter, a Devi, *Dalton Trans.* **2014**, *43*, 937–40.

[22] A. P. Milanov, T. Toader, H. Parala, D. Barreca, A. Gasparotto, C. Bock, H.-W. Becker, D. K. Ngwashi, R. Cross, S. Paul, et al., *Chem. Mater.* **2009**, *21*, 5443–5455.

[23] A. P. Milanov, T. Thiede, M. Hellwig, H. Parala, C. Bock, H.-W. Becker, D. Ngwashi, R. Cross, S. Paul, U. Kunze, et al., *ECS Trans.* **2009**, *25*, 143–150.

[24] R. Ranjith, A. Laha, E. Bugiel, H. J. Osten, K. Xu, A. P. Milanov, A. Devi, *Semicond. Sci. Technol.* **2010**, *25*, 105001.

[25] K. Xu, R. Ranjith, A. Laha, H. Parala, A. P. Milanov, R. A. Fischer, E. Bugiel, J. Feydt, S. Irsen, T. Toader, et al., *Chem. Mater.* **2012**, *24*, 651–658.

[26] T. Chen, W. Hunks, P. S. Chen, G. T. Stauf, T. M. Cameron, C. Xu, A. G. DiPasquale, A. L. Rheingold, *Eur. J. Inorg. Chem.* **2009**, *2009*, 2047–2049.

[27] T. Chen, W. Hunks, P. S. Chen, C. Xu, A. G. DiPasquale, A. L. Rheingold, *Organometallics* **2010**, *29*, 501–504.

[28] M. Eleter, L. G. Hubert-Pfalzgraf, S. Daniele, G. Pilet, B. Tinant, *Polyhedron* **2010**, *29*, 2522–2526.

[29] T. Chen, C. Xu, T. H. Baum, G. T. Stauf, J. F. Roeder, A. G. DiPasquale, A. L. Rheingold, *Chem. Mater.* **2010**, *22*, 27–35.

[30] T. Thiede, V. Gwildies, L. Alsamann, D. Rische, R. Fischer, *ECS Trans.* **2009**, *25*, 593–600.

[31] Y.-S. Won, S.-S. Park, *Bull. Korean Chem. Soc.* **2010**, *31*, 2416–2418.

[32] C. Blackman, C. Carmalt, S. Moniz, S. E. Potts, H. Davies, D. Pugh, *ECS Trans.* **2009**, *25*, 561–565.

[33] M. Reiners, K. Xu, N. Aslam, A. Devi, R. Waser, **2013**, 2–5.

[34] K. Xu, A. R. Chaudhuri, H. Parala, D. Schwendt, T. de los Arcos, H. J. Osten, A. Devi, *J. Mater. Chem. C* **2013**, *1*, 3939–3946.

[35] Y. A. Wasslen, E. Tois, S. Haukka, K. A. Kreisel, G. P. A. Yap, M. D. Halls, S. T. Barry, *Inorg. Chem.* **2010**, *49*, 1976–82.

[36] T. J. J. Whitehorne, J. P. Coyle, A. Mahmood, W. H. Monillas, G. P. A. Yap, S. T. Barry, *Eur. J. Inorg. Chem.* **2011**, *2011*, 3240–3247.

[37] S.-D. Bai, J.-P. Guo, D.-S. Liu, *Dalton Trans.* **2006**, 2244–50.

[38] J. Barker, M. Kilner, *Coord. Chem. Rev.* **1994**, *133*, 219–300.

[39] F. T. Edelmann, *Coord. Chem. Rev.* **1994**, *137*, 403–481.

[40] F. T. Edelmann, *Chem. Soc. Rev.* **2009**, *38*, 2253–68.

[41] T.-G. Ong, G. P. A. Yap, D. S. Richeson, *J. Am. Chem. Soc.* **2003**, *125*, 8100–1.

[42] B. S. Lim, A. Rahtu, J.-S. Park, R. G. Gordon, *Inorg. Chem.* **2003**, *42*, 7951–8.

[43] B. S. Lim, A. Rahtu, R. G. Gordon, *Nat. Mater.* **2003**, *2*, 749–54.

[44] F. T. Edelmann, in *Adv. Organomet. Chem.*, **2008**, pp. 183–352.

[45] G. R. Desiraju, *Nature* **2001**, *412*, 397–400.

[46] Z. Li, S. T. Barry, R. G. Gordon, *Inorg. Chem.* **2005**, *44*, 1728–35.

[47] A. L. Brazeau, Z. Wang, C. N. Rowley, S. T. Barry, *Inorg. Chem.* **2006**, *45*, 2276–81.

[48] C. N. Rowley, G. A. DiLabio, S. T. Barry, *Inorg. Chem.* **2005**, *44*, 1983–91.

[49] B. W. Hansen, E. B. Pederson, *Acta Chem. Scand. B* **1980**, *34*, 369–373.

[50] B. D. Ward, H. Risler, K. Weitershaus, S. Bellemin-Laponnaz, H. Wadepohl, L. H. Gade, *Inorg. Chem.* **2006**, *45*, 7777–87.

[51] G. M. Sheldrick, *Acta Crystallogr. A.* **2008**, *64*, 112–22.

[52] C. Andricacos, C. Uzoh, J. O. Dukovic, J. Horkans, H. Deligianni, *Electrochem. Fabr.* **1998**, *42*, 567–574.

[53] Y. Liu, L. Yin, S. Bliznakov, P. Kondos, P. Borgesen, D. W. Henderson, C. Parks, J. Wang, E. J. Cotts, N. Dimitrov, *Components Packag. Technol.* **2008**, *33*, 2105–2110.

[54] R. C. Weast, Ed. , *CRC Handbook of Chemistry and Physics*, The Chemical Rubber Co., **1968**.

[55] "2011 Edition of the International Technology Roadmap for Semiconductors," can be found under http://www.itrs.net/, **n.d.**

[56] M. K. Dobkin, D. , Zuraw, *Principles of Chemical Vapor Deposition*, Springer, **2003**.

[57] S. M. George, *Chem. Rev.* **2010**, *110*, 111–131.

[58] T. J. Knisley, L. C. Kalutarage, C. H. Winter, *Coord. Chem. Rev.* **2013**, *257*, 3222–3231.

[59] D. J. Hagen, I. Povey, S. Rushworth, J. S. Wrench, L. Keeney, M. Schmidt, N. Petkov, S. T. Barry, J. P. Coyle, M. E. Pemble, *J. Mater. Chem. C* **2014**, *2*, 9205–9214.

[60] C. Lampe-onnerud, U. Jansson, A. Hårsta, J. Carlsson, *J. Cryst. Growth* **1992**, *121*, 223–234.

[61] P. Mårtensson, J. Carlsson, *Chem. Vap. Depos.* **1997**, *3*, 45–50.

[62] T. Törndahl, M. Ottosson, J.-O. Carlsson, *Thin Solid Films* **2004**, *458*, 129–136.

[63] M. Juppo, M. Ritala, M. Leskela, *J. Vac. Sci. Technol. A Vacuum, Surfaces, Film.* **1997**, *15*, 2330.

[64] V. L. Young, D. F. Cox, M. E. Davis, *Chem. Mater.* **1993**, *5*, 1701–1709.

[65] P.-F. Hsu, Y. Chi, T.-W. Lin, C.-S. Liu, A. J. Carty, S.-M. Peng, *Chem. Vap. Depos.* **2001**, *7*, 28–31.

[66] R. Becker, a. Devi, J. Weiß, U. Weckenmann, M. Winter, C. Kiener, H.-W. Becker, R. a. Fischer, *Chem. Vap. Depos.* **2003**, *9*, 149–156.

[67] D.-Y. Moon, D.-S. Han, S.-Y. Shin, J.-W. Park, B. M. Kim, J. H. Kim, *Thin Solid Films* **2011**, *519*, 3636–3640.

[68] T. J. Knisley, T. C. Ariyasena, T. Sajavaara, M. J. Saly, C. H. Winter, *Chem. Mater.* **2011**, *23*, 4417–4419.

[69] L. C. Kalutarage, S. B. Clendenning, C. H. Winter, *Chem. Mater.* **2014**, *26*, 3731–3738.

[70] Z. Li, A. Rahtu, R. G. Gordon, *J. Electrochem. Soc.* **2006**, *153*, C787.

[71] V. Krisyuk, L. Aloui, N. Prud'homme, B. Sarapata, F. Senocq, D. Samelor, C. Vahlas, *ECS Trans.* **2009**, *25*, 581–586.

[72] L. Shao, J. P. Coyle, S. T. Barry, J. Albert, *Opt. Mater. Express* **2011**, *1*, 128–137.

[73] P. Doppelt, *Coord. Chem. Rev.* **1998**, *180*, 1785–1809.

[74] J. Rickerby, J. H. G. Steinke, *Chem. Rev.* **2002**, *102*, 1525–50.

[75] M. E. Gross, *J. Electrochem. Soc.* **1991**, *138*, 2422–2426.

[76] J. A. T. Norman, B. A. Muratore, P. N. Dyer, D. A. Roberts, A. K. Hochberg, *Le J. Phys. IV* **1991**, *02*, C2–271–C2–278.

[77] M. Utriainen, M. Kroger-Laukkanen, L.-S. Johansson, L. Niinisto, *Appl. Surf. Sci.* **2000**, *157*, 151–158.

[78] A. Niskanen, A. Rahtu, T. Sajavaara, K. Arstila, M. Ritala, M. Leskelä, *J. Electrochem. Soc.* **2005**, *152*, G25.

[79] L. Wua, E. Eisenbraun, *J. Vac. Sci. Technol. B Microelectron. Nanom. Struct.* **2007**, *25*, 2581.

[80] P. Mårtenson, Jan-Oto Carlsson, *J. Electrochem. Soc.* **1998**, *145*, 5–10.

[81] A. U. Mane, S. A. Shivashankar, *Mater. Sci. Semicond. Process.* **2004**, *7*, 343–347.

[82] R. Gupta, B. G. Willis, *Appl. Phys. Lett.* **2007**, *90*, 253102.

[83] I. J. Hsu, B. E. McCandless, C. Weiland, B. G. Willis, *J. Vac. Sci. Technol. A Vacuum, Surfaces, Film.* **2009**, *27*, 660.

[84] C. Jezewski, W. A. Lanford, C. J. Wiegand, J. P. Singh, P.-I. Wang, J. J. Senkevich, T.-M. Lu, *J. Electrochem. Soc.* **2005**, *152*, C60.

[85] R. Solanki, B. Pathangey, *Electrochem. Solid-State Lett.* **2000**, *3*, 479–480.

[86] S.-W. Kang, J.-Y. Yun, Y. H. Chang, *Chem. Mater.* **2010**, *22*, 1607–1609.

[87] D. Moon, W. Kim, T. Kim, B. Kang, J. Park, S. J. Yeom, J. H. Kim, *J. Korean Phys. Soc.* **2009**, *54*, 1330–1333.

[88] B. H. Lee, J. K. Hwang, J. W. Nam, S. U. Lee, J. T. Kim, S.-M. Koo, a. Baunemann, R. A. Fischer, M. M. Sung, *Angew. Chemie* **2009**, *121*, 4606–4609.

[89] B. Vidjayacoumar, D. J. H. Emslie, S. B. Clendenning, J. M. Blackwell, J. F. Britten, A. Rheingold, *Chem. Mater.* **2010**, *22*, 4844–4853.

[90] K.-H. Park, A. Z. Bradley, J. S. Thompson, W. J. Marshall, *Inorg. Chem.* **2006**, *45*, 8480–2.

[91] J. P. Coyle, G. Dey, E. R. Sirianni, M. L. Kemell, G. P. A. Yap, M. Ritala, M. Leskelä, S. D. Elliott, S. T. Barry, *Chem. Mater.* **2013**, *25*, 1132–1138.

[92] A. M. James, R. K. Laxman, F. R. Fronczek, A. W. Maverick, *Inorg. Chem.* **1998**, *37*, 3785–3791.

[93] G. Dey, S. D. Elliott, *J. Phys. Chem. A* **2012**, *116*, 8893–901.

[94] E. S. Hwang, J. Lee, *Chem. Mater.* **2000**, *12*, 2076–2081.

[95] Y. K. Ko, B. S. Seo, D. S. Park, H. J. Yang, W. H. Lee, P. J. Reucroft, J. G. Lee, *Semicond. Sci. Technol.* **2002**, *17*, 978 – 982.

[96] Y. Au, Y. Lin, R. G. Gordon, *J. Electrochem. Soc.* **2011**, *158*, D248.

[97] O.-K. Kwon, H.-B. Lee, S.-W. Kang, H.-S. Park, *J. Vac. Sci. Technol. A Vacuum, Surfaces, Film.* **2002**, *20*, 408.

[98] D.-S. Lee, W.-J. Lee, *Jpn. J. Appl. Phys.* **2009**, *48*, 076004.

[99] H. Park, A. Kim, C. Lee, J.-S. Lee, J. Lee, *Appl. Phys. Lett.* **2009**, *94*, 213508.

[100] O.-K. Kwon, J.-H. Kim, H.-S. Park, S.-W. Kang, *Electrochem. Solid-State Lett.* **2003**, *6*, C109.

[101] K.-C. Shim, H.-B. Lee, O.-K. Kwon, H.-S. Park, W. Koh, S.-W. Kang, *J. Electrochem. Soc.* **2002**, *149*, G109.

[102] D. Josell, D. Wheeler, T. P. Moffat, *Electrochem. Solid-State Lett.* **2002**, *5*, C44.

[103] G. Dey, S. D. Elliott, *RSC Adv.* **2014**, *4*, 34448.

[104] B. S. Lim, A. Rahtu, R. G. Gordon, *Nat. Mater.* **2003**, *2*, 749–54.

[105] A. Turgambaeva, N. Prud'homme, V. Krisyuk, C. Vahlas, *J. Nanosci. Nanotechnol.* **2011**, *11*, 8198–8201.

[106] Q. Ma, H. Guo, R. G. Gordon, F. Zaera, *Chem. Mater.* **2010**, *22*, 352–359.

[107] J. P. Coyle, W. H. Monillas, G. P. A. Yap, S. T. Barry, *Inorg. Chem.* **2008**, *47*, 683–9.

[108] J. P. Coyle, P. J. Pallister, A. Kurek, E. R. Sirianni, G. P. A. Yap, S. T. Barry, *Inorg. Chem.* **2013**, *52*, 910–7.

[109] G. S. Girolami, P. M. Jeffries, L. H. Dubois, *J. Am. Chem. Soc.* **1993**, *115*, 1015–1024.

[110] P. G. Gordon, A. Kurek, S. T. Barry, *ECS J. Solid State Sci. Technol.* **2014**, *4*, N3188–N3197.

[111] D. J. Hagen, I. M. Povey, S. Rushworth, J. S. Wrench, L. Keeney, M. Schmidt, N. Petkov, S. T. Barry, J. P. Coyle, M. E. Pemble, *J. Mater. Chem. C* **2014**, *2*, 9205–9214.

[112] X. Tao, K.-C. Shen, Q.-Y. Tang, M. Feng, J.-T. Fang, Y.-L. Wang, Y.-Z. Shen, *Appl. Organomet. Chem.* **2012**, *26*, 323–329.

[113] C. D. Hurd, A. G. Prapas, *J. Org. Chem.* **1958**, *24*, 388–392.

[114] M. Ritala, M. Leskelä, *Handbook of Thin Films*, Elsevier, **2002**.

[115] M. Leskelä, M. Ritala, *Thin Solid Films* **2002**, *409*, 138–146.

[116] H. Kim, *J. Vac. Sci. Technol. B Microelectron. Nanom. Struct.* **2003**, *21*, 2231.

[117] P. Doppelt, *Coord. Chem. Rev.* **1998**, *178-180*, 1785–1809.

[118] F. T. Edelmann, *Chem. Soc. Rev.* **2012**, *41*, 7657–72.

[119] Z. Li, A. Rahtu, R. G. Gordon, *J. Electrochem. Soc.* **2006**, *153*, C787.

[120] J. P. Coyle, W. H. Monillas, G. P. A. Yap, S. T. Barry, *Inorg. Chem.* **2008**, *47*, 683–9.

[121] A. M. Willcocks, T. P. Robinson, C. Roche, T. Pugh, S. P. Richards, A. J. Kingsley, J. P. Lowe, A. L. Johnson, *Inorg. Chem.* **2012**, *51*, 246–57.

[122] Q. Ma, H. Guo, R. G. Gordon, F. Zaera, *Chem. Mater.* **2011**, *23*, 3325–3334.

[123] Z. Li, S. T. Barry, R. G. Gordon, *Inorg. Chem.* **2005**, *44*, 1728–35.

[124] V. Krisyuk, L. Aloui, N. Prud'homme, S. Sysoev, F. Senocq, D. Samelor, C. Vahlas, *Electrochem. Solid-State Lett.* **2011**, *14*, D26–D29.

[125] Q. Ma, H. Guo, R. G. Gordon, F. Zaera, *Chem. Mater.* **2010**, *22*, 352–359.

[126] A. Turgambaeva, N. Prud'homme, V. Krisyuk, C. Vahlas, *J. Nanosci. Nanotechnol.* **2011**, *11*, 8198–8201.

[127] T. Tsuda, K. Watanabe, K. Miyata, H. Yamamoto, T. Saegusa, *Inorg. Chem.* **1981**, *20*, 2728–2730.

[128] Y. A. Wasslen, A. Kurek, P. A. Johnson, T. C. Pigeon, W. H. Monillas, G. P. A. Yap, S. T. Barry, *Dalton Trans.* **2010**, *39*, 9046–54.

[129] J. P. Coyle, A. Kurek, P. J. Pallister, E. R. Sirianni, G. P. A. Yap, S. T. Barry, *Chem. Commun. (Camb).* **2012**, *48*, 10440–2.

[130] F. A. Cotton, L. M. Daniels, X. Feng, D. J. Maloney, J. H. Matonic, C. A. Murilio, *Inorganica Chim. Acta* **1997**, *256*, 291–301.

[131] H. E. Abdou, A. A. Mohamed, J. P. Fackler, *J. Clust. Sci.* **2007**, *18*, 630–641.

[132] X. Jiang, J. C. Bollinger, M.-H. Baik, D. Lee, *Chem. Commun. (Camb).* **2005**, 1043–5.

[133] J. Beck, J. Strahle, *Angew. Chemie Int. Ed. English* **1986**, *25*, 95–96.

[134] G. V Kunte, S. A. Shivashankar, A. M. Umarji, *Meas. Sci. Technol.* **2008**, *19*, 025704.

[135] M. Dai, J. Kwon, M. D. Halls, R. G. Gordon, Y. J. Chabal, *Langmuir* **2010**, *26*, 3911–7.

[136] S. Haukka, E. L. Lakomaa, A. Root, *J. Phys. Chem.* **1993**, *97*, 5085–5094.

[137] Y. A. Wasslen, E. Tois, S. Haukka, K. A. Kreisel, G. P. A. Yap, M. D. Halls, S. T. Barry, *Inorg. Chem.* **2010**, *49*, 1976–82.

[138] Horacio E. Bergna, *The Colloid Chemistry of Silica*, American Chemical Society, Washington DC, **1994**.

[139] G. E. Maciel, D. W. Sindorf, *J. Am. Chem. Soc.* **1980**, *102*, 7606–7607.

[140] A. L. Spek, *J. Appl. Crystallogr.* **2003**, *36*, 7–13.

[141] V. Lehmann, *J. Electrochem. Soc.* **1990**, *137*, 653.

[142] V. Lehmann, U. Gösele, *Appl. Phys. Lett.* **1991**, *58*, 856.

[143] K. Barla, G. Bomchil, R. Herino, J. C. Pfister, J. Baruchel, *J. Cryst. Growth* **1984**, *68*, 721–726.

[144] G. Korotcenkov, B. K. Cho, *Crit. Rev. Solid State Mater. Sci.* **2010**, *35*, 153–260.

[145] X. Li, P. W. Bohn, *Appl. Phys. Lett.* **2000**, *77*, 2572.

[146] C.-L. Lee, K. Tsujino, Y. Kanda, S. Ikeda, M. Matsumura, *J. Mater. Chem.* **2008**, *18*, 1015.

[147] C. C. Striemer, P. M. Fauchet, *Phys. status solidi* **2003**, *197*, 502–506.

[148] M. Barberoglou, V. Zorba, A. Pagozidis, C. Fotakis, E. Stratakis, *Langmuir* **2010**, *26*, 13007–14.

[149] W. K. Choi, T. H. Liew, M. K. Dawood, H. I. Smith, C. V Thompson, M. H. Hong, *Nano Lett.* **2008**, *8*, 3799–802.

[150] C. Chartier, S. Bastide, C. Lévy-Clément, *Electrochim. Acta* **2008**, *53*, 5509–5516.

[151] H. Asoh, F. Arai, S. Ono, *Electrochim. Acta* **2009**, *54*, 5142–5148.

[152] B. S. Aldinger, A. Gupta, I. T. Clark, M. A. Hines, *J. Appl. Phys.* **2010**, *107*, 103520.

[153] K. Tsujino, M. Matsumura, *Electrochim. Acta* **2007**, *53*, 28–34.